Challenge Journal of
CONCRETE RESEARCH LETTERS

Vol.17 No.1 (2026)

acoustic emission aerated concrete artificial neural network compressive strength corrosion cracking ductility durability energy absorption ferrocement flexural strength fly ash fracture mechanics mechanical properties mortar optimization nanoparticle palm oil fuel ash polymer concrete reinforced concrete self-compacting concrete steam curing strengthening superplasticizer tensile strength workability waste disposal water absorption

ISSN 2548-0928

TULPAR ACADEMIC PUBLISHING

Challenge Journal of
CONCRETE RESEARCH LETTERS

E-mail: *cjcrl@challengejournal.com*

Web page: *cjcrl.challengejournal.com*

Tulpar Academic Publishing
www.tulparpublishing.com

Challenge Journal of
CONCRETE RESEARCH LETTERS

CONTENTS

Research Articles

TULPAR
ACADEMIC PUBLISHING

Challenge Journal of CONCRETE RESEARCH LETTERS

Research Article

Effect of polyethylene terephthalate granules on nano-$CaCO_3$-blended concrete

Awinash Kumar [a], Sachin Kumar Singh [a], Abhishek Mishra [a], Awadhesh Srivastava [a,*]

[a] *Department of Civil Engineering, Institute of Engineering and Technology, Lucknow, 226021 Uttar Pradesh, India*

ABSTRACT

This study explores the effects of partially replacing fine aggregate with 10% polyethylene terephthalate granules (PET) and cement with varying amounts (0–5%) of nano calcium carbonate ($CaCO_3$) in M40 grade concrete. Concrete mixes were tested for workability, density, compressive strength, tensile strength, and flexural strength. Microstructural characteristics were examined using Scanning Electron Microscopy (SEM) and X-Ray Diffraction (XRD), while ANSYS simulations were used to validate compressive strength results. The results indicated that the optimal performance was achieved at 2% nano-$CaCO_3$ replacement along with 10% PET. Although workability and density slightly declined with increasing $CaCO_3$ content, compressive and tensile strengths showed only minor reductions, reflecting the limited reactivity of $CaCO_3$. On the other hand, the addition of PET improved flexural strength and toughness, though these benefits reduced gradually at higher $CaCO_3$ levels. SEM and XRD analyses confirmed uniform dispersion and the presence of crystalline phases, while ANSYS simulations closely matched experimental results, reinforcing the validity of the findings. The study is limited to M40 grade concrete and specific replacement levels. However, the findings suggest that combining PET waste and nano-$CaCO_3$ can enhance mechanical performance while contributing to environmental benefits by reducing plastic waste and CO_2 emissions. Further research is needed for broader application and lifecycle assessment.

ARTICLE INFO

Article history:
Received – June 25, 2025
Revision requested – September 1, 2025
Revision received – September 4, 2025
Accepted – September 15, 2025

Keywords:
Polyethylene terephthalate
Nano-$CaCO_3$
Waste management
Environmental pollution
Compressive strength
Flexural strength

Citation: Kumar A, Singh SK, Mishra A, Srivastava A (2026). Effect of polyethylene terephthalate granules on nano-$CaCO_3$-blended concrete. *Challenge Journal of Concrete Research Letters*, 17(1), 1–12.

1. Introduction

The cement industry is responsible for approximately 8–10% of all human-generated CO_2 emissions worldwide. With production projected to increase from around 4 billion metric tons today to more than 6 billion by 2050, this will further contribute to atmospheric CO_2 levels (Andrew 2018; Srivastava et al. 2025). In response, global initiatives are focusing on reducing the sector's environmental impact while still meeting rising demand. The cement technology roadmap presents key strategies for enhancing sustainability, including adopting energy-efficient processes, utilizing alternative fuels, reducing clinker content, and fostering technological innovation (Camiletti et al. 2013).

Among these approaches, clinker substitution stands out as a widely used and economical option. This technique involves partially replacing cement with supplementary cementitious materials such as fly ash, ground granulated blast furnace slag, silica fume, and limestone powder. Recently, nanotechnology has become increasingly popular, with nanomaterials being used as partial replacements for cement clinker. These nanoparticles modify the hydrated paste at the nanoscale, leading to notable improvements in compressive and flexural strength, as well as overall performance and durability (Srivastava et al. 2025; Cao et al. 2019). Research has demonstrated that adding nanoparticles including nano-SiO_2, nano-TiO_2, nano-$CaCO_3$, nano-Fe_2O_3, nano-ZrO_2, nano-Al_2O_3, and nano-graphene (as well as carbon nano-

* *Corresponding author*. E-mail address: kumarawadhesh0011@gmail.com (A. Srivastava)
ISSN: 2548-0928 / DOI: https://doi.org/10.20528/cjcrl.2026.01.001

tubes and carbon nanofibers to cementitious composites can significantly enhance their performance and longevity (d'Amora et al. 2020; Supit et al. 2014).

However, the high cost of many of these nanomaterials limits their widespread use in the cement industry. In comparison, nano-$CaCO_3$ is relatively more affordable and has been shown to potentially be produced at cement plants using waste CO_2 from cement production (Daniyal et al. 2019; Hashim et al. 2018).

In recent years, plastic production has steadily risen due to its widespread use in daily life. However, plastic waste is non-biodegradable and chemically hazardous, causing significant environmental harm. The United Nations Environment Program reports that global annual plastic production exceeds 400 million tonnes, with around 87% (or 350 million tonnes) becoming waste. As of 2015, the plastic packaging industry was generating approximately 141 million tonnes of single-use plastics annually, accounting for 47% of all plastic waste (Saikia et al. 2014). China emerged as the largest global producer of plastic packaging waste, contributing 40 million tonnes. Meanwhile, the United States had the highest per capita production of plastic packaging waste, totaling 45 million tonnes (Bamigboye et al. 2021).

Plastics come in two main types: thermoplastics and thermosetting plastics. Thermoplastics can be melted and recycled multiple times within the industry. Some common examples of thermoplastics include high-density polyethylene, low-density polyethylene, polyethylene terephthalate (PET), polyethylene, polystyrene, polypropylene, polyamide, polyoxymethylene, and polytetrafluoroethylene. In contrast, thermosetting plastics cannot be melted due to their strong molecular bonds and crosslinked structure, which makes them resistant to melting. Examples of thermosetting plastics are melamine, silicone, epoxy resin, phenolic, unsaturated polyester, and polyurethane. Currently, these plastic wastes are either incinerated or buried, both of which are expensive and environmentally damaging. Reusing thermosetting plastic waste could help reduce both pollution and waste management costs.

Among thermoplastics, PET is the most commonly used polyester. Frigione (2010) conducted research to evaluate the impact of replacing 5% of fine aggregates in concrete with unwashed PET particles by weight. The study assessed how this substitution influenced workability, compressive strength, and splitting tensile strength. Both the sand and PET particles used had sizes ranging from 300 μm to 2.36 mm. The results showed a slight decrease in compressive strength (less than 2%) and splitting tensile strength (between 1.6% and 2.4%) for the concrete with PET, but no significant change in workability. Almeshal et al. (2020) examined the effects of substituting sand with shredded PET waste (ranging from 0.075 to 4 mm) on concrete's workability, unit weight, and compressive strength, using replacement rates from 10% to 50% by volume. Their findings indicated that increasing the PET content significantly reduced workability, with slump values dropping from 90 mm for the control specimens to just 10 mm for those with 50% PET. This reduction in workability was attributed to PET's lower density compared to sand, which also adversely affected compressive strength. Concrete mixtures with 40% and 50% PET saw compressive strength reductions of 31% and 60%, respectively, compared to the control. Dawood et al. (2021) investigated concrete properties with shredded PET waste as a partial volumetric replacement of fine aggregates, ranging from 5% to 20%. Although both the fine aggregates and PET fibers were less than 4.75 mm in size, PET fibers predominantly ranged from 2.36 mm to 1.18 mm, with significant variation in gradation (0–4.47 mm). Their study found that workability decreased as PET content increased, with a notable 62.5% reduction for the 20% PET replacement compared to the control. This decrease was due to the larger surface area of PET particles. However, compressive strength improved with up to 15% PET replacement, peaking at a 7.5% increase for 12% PET, before declining with higher replacement levels (Choi et al. 2005).

Research on using PET waste as a partial replacement for concrete components (fine and coarse aggregates) has been conducted before, but results have varied based on the shape and size of the PET waste. While PET fibers have been commonly used, PET granules have not been extensively studied (Ismail and Al-Hashmi 2008). A recent study demonstrated that substituting 2% of cement with nano-$CaCO_3$ can lead to a 69% reduction in CO_2 emissions from cement production (Batuecas et al. 2021). Specifically, the CO_2 emissions decreased from 0.96 kg CO_2 eq./kg of cement to 0.3 kg CO_2 eq./kg. This reduction illustrates that nano-$CaCO_3$, even at lower replacement levels compared to fly ash, offers significant economic and environmental advantages (Aslani et al. 2021; Limami et al. 2020; Moghadam et al. 2009).

This research study investigates the impact of partial substitution of Polyethylene terephthalate (PET) with fine aggregate and nano calcium carbonate ($CaCO_3$) particles with cement in M40 grade concrete respectively. Important physical properties, were assessed alongside the microstructural observations. The cement is replaced by $CaCO_3$ with 0%, 2%, 3%, 4%, and 5%, while the fine aggregate is replaced by 10 % PET in all possible variations. This paper also examines the technical feasibility of incorporating nano-$CaCO_3$ in cement.

2. Materials and Method

2.1. Materials

In this study, the binder materials included only Ordinary Portland Cement (OPC) 43-grade in the control mixture, while the experimental mixtures used was OPC combined with nano-$CaCO_3$ particles. The nano-$CaCO_3$ particles employed had sizes ranging from 15 to 40 nm and contained 98% $CaCO_3$ shown in Fig. 1(a) (Siddique et al. 2008). The property of PET granules was shown in Table 1 and Fig. 1(b). A superplasticizer, commercially known as Fosroc (Complast SP40 G8 QCDA820), was used to enhance workability. Coarse aggregates with a maximum particle size of 20 mm and a specific gravity of 2.55 were utilized. Natural sand, with a specific gravity of 2.71, served as the fine aggregate. Tap water was used for mixing. The experimental test results of cement shown in Table 2.

Table 1. Characteristics of PET used in the experimental work.

Grade	Density	Manufacturer	Granule size	Source	Pre-treatment
B52A003	0.954 g/cm^3	Gail India G-Lex	≤ 4.75 mm	Post-consumer water bottles	Washed to remove impurities; air-dried; no chemical pre-treatment.

Table 2. Test results of OPC (43-grade) cement.

S. no	Properties	Test result
1	Specific gravity	3.04
2	Standard consistency	27%
3	Initial setting time	42 minutes
4	Final setting time	349 minutes

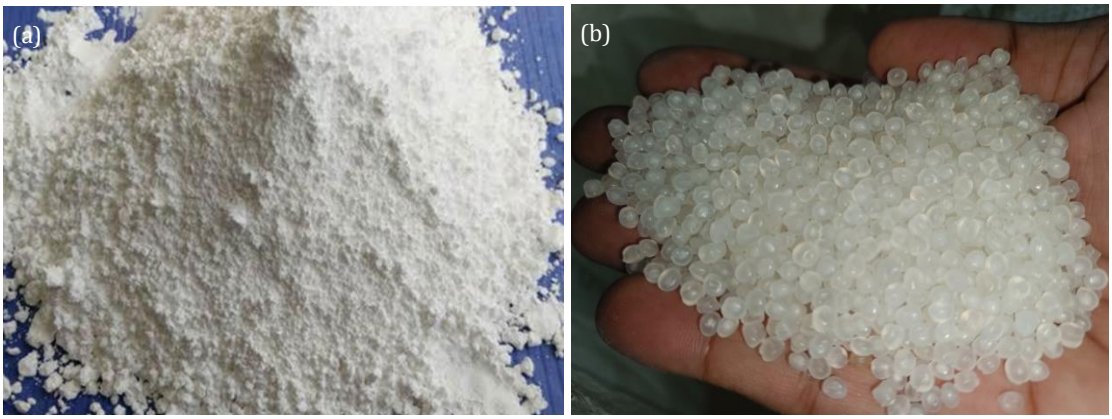

Fig. 1. (a) Nano-CaCO3; (b) PET granules.

2.2. Concrete mixes

Table 3 provides details on the mixing ratios for concrete mixes with varying amounts of nano-$CaCO_3$ as a replacement for cement. In the mix notation, "0NC10PP" indicates 0% nano-$CaCO_3$ replacement and 10% PET(PP) replacement. Concrete mixtures were prepared using different percentages of nano-$CaCO_3$ (0%, 2%, 3%, 4%, and 5%) relative to the dry cement weight, simultaneously PET was added at 10% of the fine aggregate weight for all different ratios. Small quantities of superplasticizer were incorporated into the mixtures to enhance the performance of the nano-particles (Limami et al. 2020).

Table 3. Mix design for the different concrete mix considered.

Sr. no	Concrete mix	Cement, kg/m^3	Fine aggregate, kg/m^3	Coarse aggregate, kg/m^3	Water cement ratio	Water, kg/m^3	Nano-$CaCO_3$, kg/m^3	PP granules, kg/m^3	Super plasticizer, l/m^3
1	0NC0PP	411.22	681.66	1191.75	0.36	143	0	0	1.85
2	0NC10PP	411.22	613.49	1191.75	0.36	143	0	68.17	1.85
3	2NC10PP	403.00	613.49	1191.75	0.36	143	8.22	68.17	1.85
4	3NC10PP	398.89	613.49	1191.75	0.36	143	12.33	68.17	1.85
5	4NC10PP	394.78	613.49	1191.75	0.36	143	16.44	68.17	1.85
6	5NC10PP	390.66	613.49	1191.75	0.36	143	20.56	68.17	1.85

2.3. Specimen casting and curing

To make the concrete mixes cement, coarse and fine aggregates with PET were combined in a rotary mixer. The aggregates used were in a saturated surface dry (SSD) condition. After mixing these ingredients, cement, nano-$CaCO_3$, water, and superplasticizer were added and mixed thoroughly. A portion of the fresh mixture was

then tested for slump. After the slump test, the remaining mixture was kept in the mixer and poured into oiled molds. The molds were left to set for 24 hours as shown in Fig. 2. After this, the samples were removed from the molds and cured traditionally by immersing them in water for 7, 14, and 28 days (Siddique et al. 2008).

Fig. 2. Fresh concrete cube samples.

2.4. Specimen testing

First of all, compressive strength tests were performed on cubic samples with dimensions of 150×150×150 mm, while splitting tensile strength was tested using cylindrical samples of 100×200 mm. Flexural strength was assessed with beams measuring 150×150×700 mm. After conducting these tests on concrete samples that had cured for 28 days, some fragments were collected from the fractured surfaces. These fragments were then subjected to SEM and XRD analyses for detailed microstructural examination.

3. Results and Discussion

3.1. Workability

The control concrete mix recorded a slump value of 110mm as in Fig. 3. The rounded and relatively smooth PET granules facilitated the dispersion of fine aggregates in the mixture, despite the low water-to-cement ratio. Nano-CaCO3, being a natural material with finer particles than cement, enhances particle packing in concrete and acts as a spacer. Consequently, concrete mixtures with nano-$CaCO_3$ replacement exhibited a higher slump, improving workability. Concrete mixes with PET replacements showed a slump comparable to that of the control mix (Rahmani et al. 2013; Azhdarpour et al. 2016).

3.2. Density

The concrete density decreased with the addition of PET. For concrete with a 10% PET replacement, the density was 2405 kg/m^3, which is fairly close to the control sample's density of 2465 kg/m^3. Nano-$CaCO_3$ had minimal impact on the density, yielding similar results to those with PET. These results align with findings from other studies (Rahmani et al. 2013).

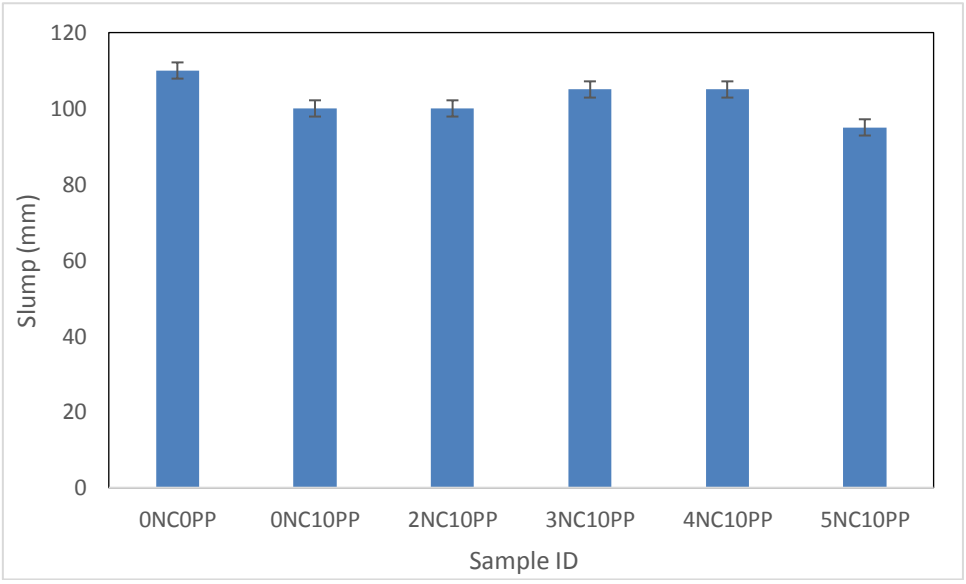

Fig. 3. Workability of the fresh concrete.

3.3. Compressive strength

The compressive strength of concrete increased by 4% with 10% PET granules, compared to the standard mix. However, adding 2% $CaCO_3$ and 10% PET granules achieved the target strength. The compressive strength of concrete dropped noticeably with higher $CaCO_3$ replacement ratios (Pezzi et al. 2006; Asha et al. 2015; Marangu et al. 2019). Differences in previous research results can be attributed to variations in the grading, shape, and size of PET particles, as well as the water-to-cement ratio used. The way PET granules affect the failure modes of concrete is related to their shape and flexibility.

When the concrete reaches its maximum load, the internal stresses shift from shear to tensile stress. Concrete with PET granules tends to maintain its shape after peak load, reducing the likelihood of collapse, whereas the standard concrete tends to be more brittle and fails through shear. This difference is likely due to the flexibility of PET granules compared to sand (Rahmani et al. 2013; Choi et al. 2005; Abu-Saleem et al. 2021). $CaCO_3$ interacts with the C_3A phase of cement to form carboalumination, which partially replaces ettringite. As a result, OPC concrete typically shows higher compressive strength than concrete with $CaCO_3$ at 28 days shown in Fig. 4, when the concrete has fully matured. Because nano-$CaCO_3$ is less reactive than cement, replacing cement with nano-$CaCO_3$ can lead to a decrease in compressive strength, especially over the long term, as there is minimal reaction between nano-$CaCO_3$ and cement hydrates (Rahmani et al. 2013; Choi et al. 2005).

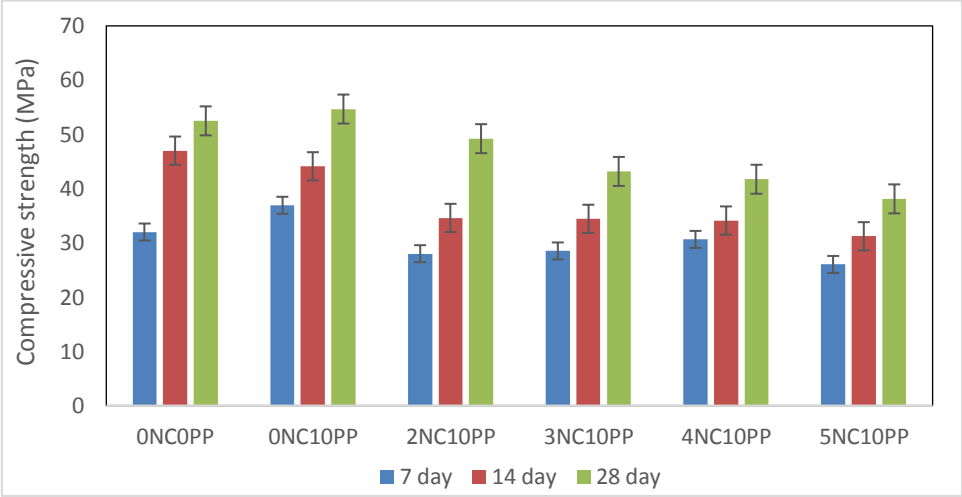

Fig. 4. Compressive strength test results of different mixes at 7, 14 and 28 days.

3.4. Tensile strength

The tensile strength dropped by 8% for the sample with 10% of PET and 0% of $CaCO_3$ compared to regular concrete as shown in Fig. 5. When more $CaCO_3$ was added, the performance worsened further. For instance, the sample with a 5% replacement rate saw a 14.15% decrease in tensile strength compared to the standard concrete. This happens because PET granules, when used in small amounts, helps in bonding the aggregates and cement better due to their flexibility and in even distribution (Fig. 6). However, once the concrete reaches its maximum strength, the PET granules tend to pull away from the cement, leading to reduced tensile strength (Pezzi et al. 2006, Asha et al. 2015).

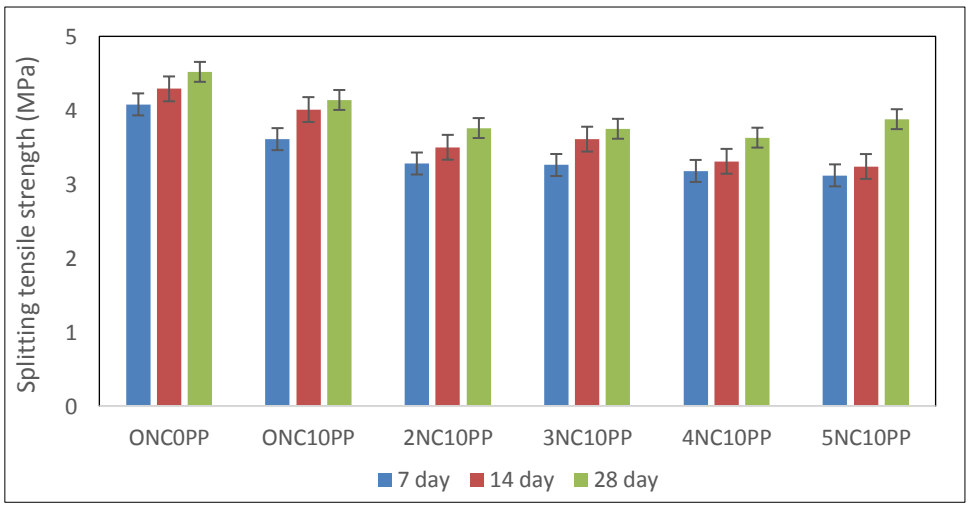

Fig. 5. Splitting tensile strength test results of different mixes at 7, 14 and 28 days.

Fig. 6. Splitting tensile strength test of cylindrical specimens.

3.5. Flexural strength

Test results in Fig. 7 show that the specimen containing 2% $CaCO_3$ and 10% PET reached the highest flexural strength of 3.23 MPa, which was a reduction of 2.71% compared to the reference concrete. Although the addition of $CaCO_3$ led to a decrease in flexural performance as its quantity increased, flexural strength remained relatively effective (Aslani et al. 2021). Fig. 8 denoted the fractured beam specimen during flexural test as per Indian standard.

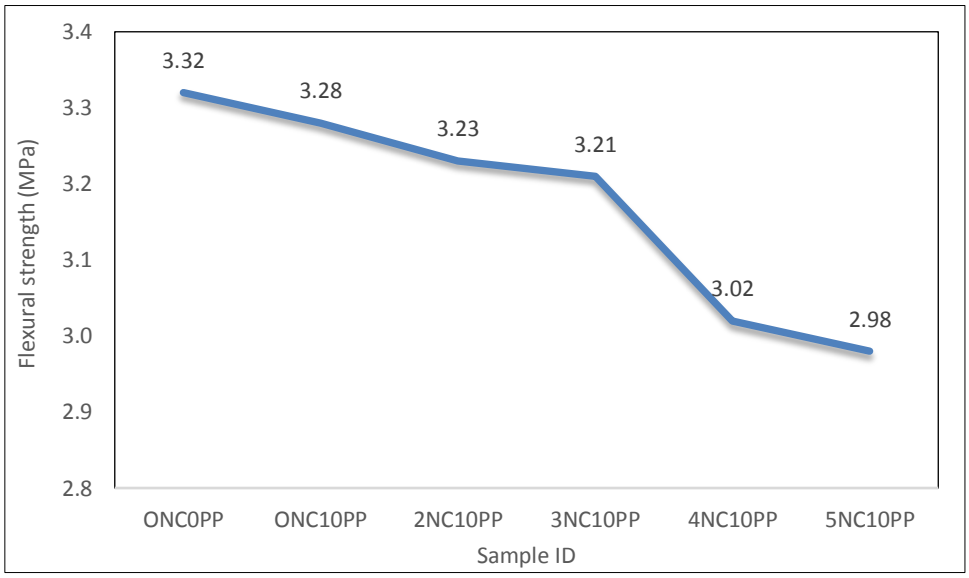

Fig. 7. Flexural strength test results at 28 days.

Fig. 8. Beam specimen after the flexural strength test.

3.6. Scanning electron microscopic (SEM) analysis

Fig. 9 shows the SEM micrographs of the 02NC10PP specimen, while Fig. 10 presents the corresponding EDS analysis used to identify its elemental composition.

Elemental composition:

- Oxygen (O): The high percentage of oxygen is expected in concrete due to the presence of various oxides and hydrated compounds such as calcium silicate hydrate (C-S-H), which is a major component of the cement matrix shown in Fig. 10.
- Aluminum (Al): Aluminum is present likely due to the aluminosilicate compounds found in the cementitious materials. Al might be a part of phases like calcium aluminate hydrates or fly ash additives if used.
- Silicon (Si): Silicon is a major component in concrete due to the presence of silicon dioxide (SiO_2) in sand and other aggregates. It is also a primary component of the C-S-H gel formed during the hydration of cement.
- Potassium (K): Potassium could be from the raw materials used in cement. It can also be from K-feldspar in the aggregates.
- Calcium (Ca): Calcium is a key element in concrete, primarily from the calcium carbonate ($CaCO_3$) nanoparticles added, as well as from calcium silicates and calcium hydroxide formed during hydration of cement.
- Platinum (Pt): Platinum is not a common component of concrete and its presence here is most likely from a coating applied to the sample for SEM analysis to make it conductive. This coating improves the quality of the SEM images.

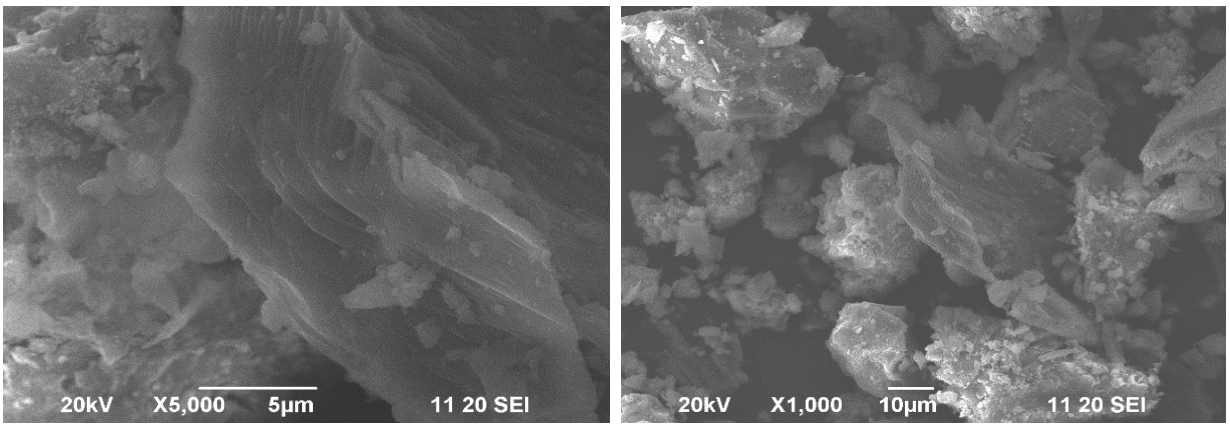

Fig. 9. SEM images of 02NC10PP.

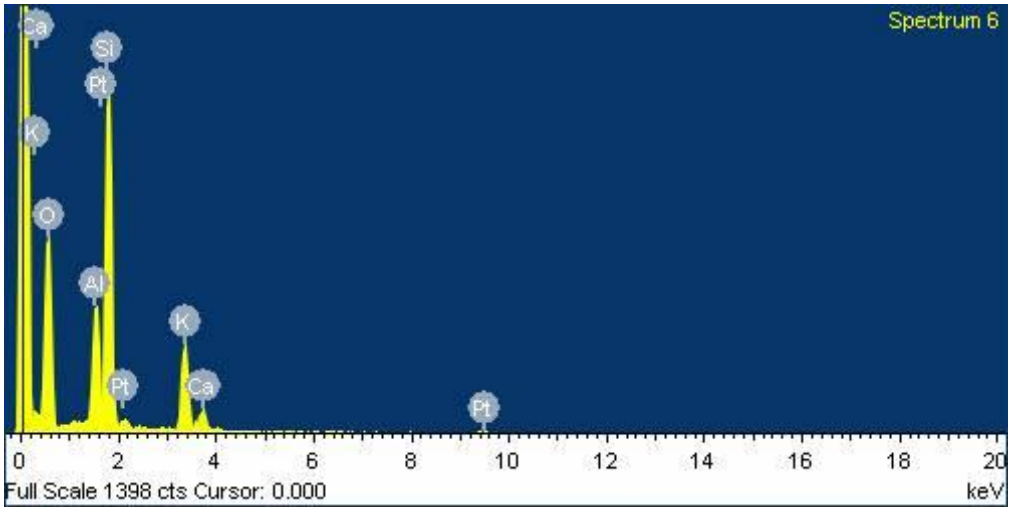

Fig. 10. EDS image of 02NC10PP.

Implications and observations:

- Nano-$CaCO_3$ and Concrete Composition: The presence of calcium (Ca) at 1.56% by weight suggests that the nano-$CaCO_3$ is dispersed throughout the sample. Although it is a small percentage, nano-$CaCO_3$ can significantly influence the microstructure and mechanical properties of concrete by acting as a filler and nucleation site for hydration products.
- Polyethylene terephthalate (PET) Granules: The analysis does not directly detect PET because it is a car-bon-based polymer and typically does not produce characteristic X-rays detectable by EDS. The influence of PET granules would be more evident in mechanical property tests and microstructural analysis rather than in elemental composition data from EDS.
- Concrete Matrix: The high content of oxygen, silicon, and aluminum suggests the formation of typical cementitious compounds such as C-S-H, ettringite, and other hydration products shown in Fig. 9. The pres-

ence of potassium and other elements aligns with typical raw materials and potential additives.
- Platinum Coating: The presence of 2% platinum is due to the conductive coating applied to the sample. This is a standard preparation step for SEM analysis to prevent charging and to improve image resolution.

The SEM-EDS analysis of the concrete sample containing 2% nano-$CaCO_3$ and 10% PET granules shows a typical composition with major elements expected in a cementitious matrix. The nano-$CaCO_3$ is present as indicated by the calcium content, while the PET granules, being non-metallic and non-oxide, are not directly detectable by EDS but contribute to the mechanical and durability properties of the concrete. The analysis confirms the expected distribution of elements in a concrete matrix modified with nano-$CaCO_3$ and PET granules represents in Table 4 (Aslani et al. 2021; Azhdarpour et al. 2016).

Table 4. EDS elemental composition of 02NC10PP.

Element	Weight, %	Atomic, %
O	58.67	73.45
Al	7.33	5.44
Si	22.54	16.08
K	7.90	4.05
Ca	1.56	0.78
Pt	2.00	0.21
Totals	100.00	–

Fig. 11 shows the SEM micrographs of the 05NC10PP specimen, while Fig. 12 presents the corresponding EDS analysis used to identify its elemental composition.

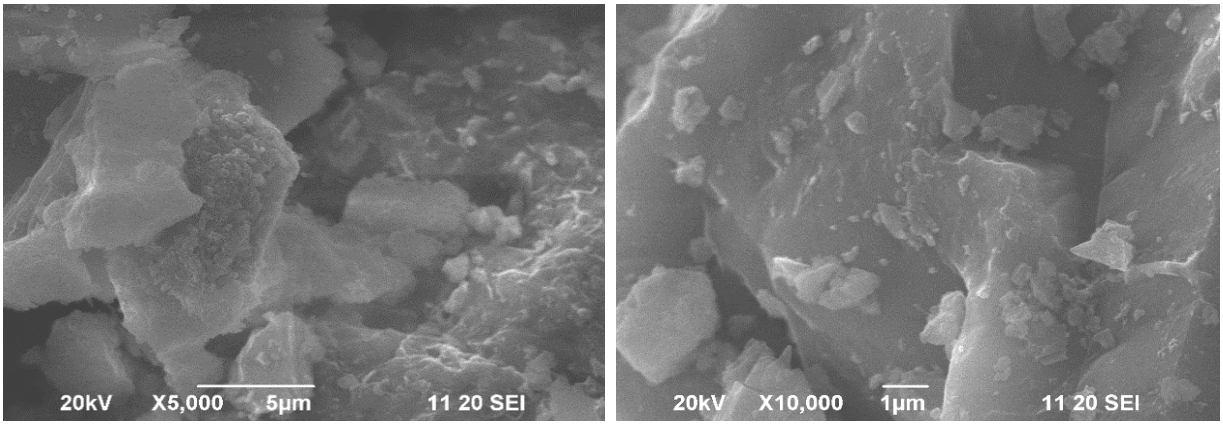

Fig. 11. SEM images of 05NC10PP.

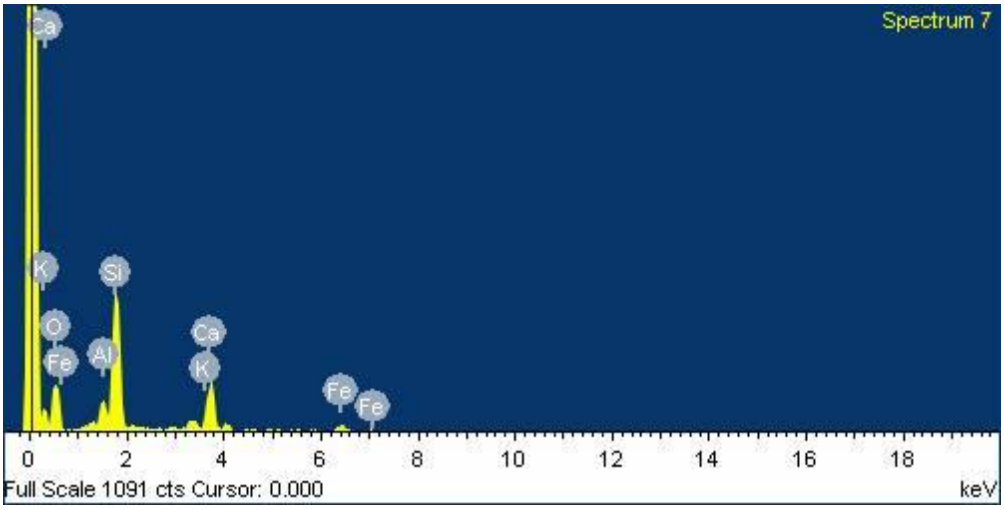

Fig. 12. EDS image 05NC10PP.

Elemental composition:
- Oxygen (O): The high percentage of oxygen is typical in concrete, reflecting the presence of various oxides and hydrated compounds. This includes calcium silicate hydrate (C-S-H), calcium hydroxide, and other hydration products.
- Aluminum (Al): Aluminum is present due to the aluminosilicate compounds in the cementitious materials. It may come from the raw materials or additives like fly ash.
- Silicon (Si): Silicon is a significant component in concrete, originating from silicon dioxide (SiO_2) in sand, aggregates, and the C-S-H gel formed during the hydration of cement.
- Potassium (K): Potassium can come from raw materials used in cement, pozzolans, or fly ash additives. It

might also be present in K-feldspar from aggregates Fig. 12.

- Calcium (Ca): The relatively high percentage of calcium indicates the presence of calcium compounds, including the 3% nano-$CaCO_3$ added. Calcium is essential in forming calcium silicate hydrates and other cement hydration products.
- Iron (Fe): Iron might be present in small amounts from raw materials used in cement production, or it could be a trace element from aggregates or additives. Iron oxides can also contribute to the color and durability of concrete.

Implications and observations:

- Nano-$CaCO_3$ and Concrete Composition: The presence of calcium at 12.59% by weight suggests a significant influence of nano-$CaCO_3$ on the overall composition. The increased calcium content compared to the previous sample with 1% nano-$CaCO_3$ indicates the higher incorporation of these nanoparticles, enhancing the concrete's microstructure and potentially improving its mechanical properties.
- PET Granules: Similar to the previous analysis, the PET granules, being carbon-based, are not directly detectable by EDS. Their impact on the concrete would be more evident in its mechanical properties and microstructure, providing improved toughness and crack resistance.
- Concrete Matrix: The high content of oxygen, silicon, and aluminum suggests the formation of typical cementitious compounds, such as C-S-H, ettringite, and other hydration products. The presence of potassium and iron aligns with typical raw materials and potential additives Fig. 12.
- Oxygen and Silicon: Both samples have high oxygen and silicon contents, typical of cementitious materials.
- Aluminum: The aluminum content is slightly lower in the 5% nano-$CaCO_3$ sample.
- Calcium: The calcium content is significantly higher in the 5% nano-$CaCO_3$ sample, reflecting the increased addition of nano-$CaCO_3$.
- Iron: The new sample has a measurable amount of iron, which was not present in the previous analysis, indicating possible variations in the raw materials or additives used.

The SEM-EDS analysis of the concrete sample with 5% nano-$CaCO_3$ and 10% PET granules shows a typical composition with significant calcium content due to the increased nano-$CaCO_3$ addition shown in Fig. 11. The elemental composition suggests the formation of standard cementitious phases, with the added nano-$CaCO_3$ likely improving the microstructure and mechanical properties of the concrete as shown in Table 5. The PET granules, while not detectable by EDS, contribute to enhanced toughness and crack resistance. The presence of iron in this sample indicates some variation in raw materials or additives compared to the previous sample (Marangu et al. 2019; Rahmani et al. 2013; Abu-Saleem et al. 2021).

Table 5. EDS elemental composition of 05NC10PP.

Element	Weight, %	Atomic, %
O	52.73	69.14
Al	4.10	3.19
Si	24.85	18.56
K	2.31	1.24
Ca	12.59	6.59
Fe	3.42	1.28
Totals	100.00	–

3.7. X-ray diffraction (XRD) analysis

As shown in Fig. 13, the XRD pattern of the 2NC10PP specimen indicates the presence of distinct crystalline phases within the concrete matrix. The intensity peaks represent the constructive interference of diffracted X-rays, while the 2θ values correspond to specific lattice planes of the crystalline constituents. The most prominent peaks can be associated with calcium carbonate, particularly those observed around 24° to 25° and 29° to 30°. In particular, the peak near 29.4° is characteristic of the (104) plane of calcite, confirming the presence of $CaCO_3$ in the specimen. In addition, the peaks detected at higher diffraction angles may be attributed to other crystalline phases present in the cementitious matrix, including hydration products and mineral constituents. The incorporation of nano-$CaCO_3$ may also act as a nucleation site, contributing to microstructural refinement and supporting the mechanical performance of the concrete.

Similarly, Fig. 14 shows the XRD pattern of the 5NC10PP specimen, which also exhibits several sharp peaks indicating well-defined crystalline phases. The most prominent peaks appear around 24.77°, 30.61°, and 50.07° 2θ, suggesting the presence of calcite and other crystalline compounds in the matrix. Moreover, several smaller peaks are distributed across the diffraction range, indicating minor phases that may be associated with cement hydration products such as calcium silicate hydrates and ettringite. The higher $CaCO_3$ content in this mixture may explain the stronger calcite-related reflections. Although PET-related phases are difficult to identify directly because of peak overlap and the polymeric nature of PET, the XRD pattern still confirms that the concrete contains the expected crystalline components of a modified cementitious composite.

4. Numerical Verification Through Software

The compressive strength data for concrete specimens 0NC0PP, 0NC10PP, 2NC10PP, 3NC10PP, 4NC10PP, and 5NC10PP were verified using ANSYS Workbench 2024 R2. The comparison between the experimental and numerical results is shown in Fig. 15. A standard-sized concrete cube with dimensions of 150 mm × 150 mm × 150 mm was modeled in ANSYS Workbench 2024 R2. To analyze the stress distribution of the concrete cube, the following procedure was adopted:

- First, a new static structural analysis system was created in the Workbench project. After that, the geometry was defined, and a cube with the specified dimensions was created.
- Material properties were assigned by selecting concrete and inputting the experimental density value.
- Other relevant material properties such as Young's modulus and Poisson's ratio were also assigned.
- The analysis then proceeded to the meshing stage by generating a suitable mesh for the cube. In this setup, boundary conditions were applied by fixing one face of the cube to simulate a fixed support.
- A load was then applied on the opposite face in the negative y-axis direction.
- After setting up the boundary conditions and loading, the model was solved.
- Once the solution was complete, the results were reviewed by plotting the equivalent (von Mises) stress distribution to understand the stress behavior within the concrete cube under the given loading conditions. Table 6 presents the comparison between the experimental and analytical data.

Table 6. Compressive strength at 28th day (MPa).

Concrete mix	Experiment	Numerical
0NC0PP	52.49	53.23
0NC10PP	54.675	55.12
2NC10PP	47.21	47.59
3NC10PP	43.17	43.75
4NC10PP	41.73	42.57
5NC10PP	38.11	39.14

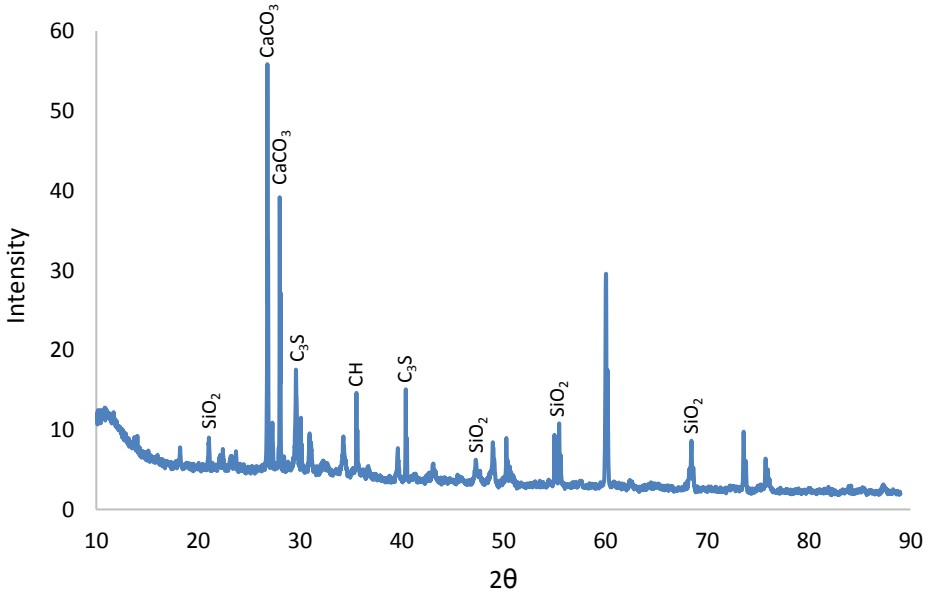

Fig. 13. XRD data of 2NC10PP.

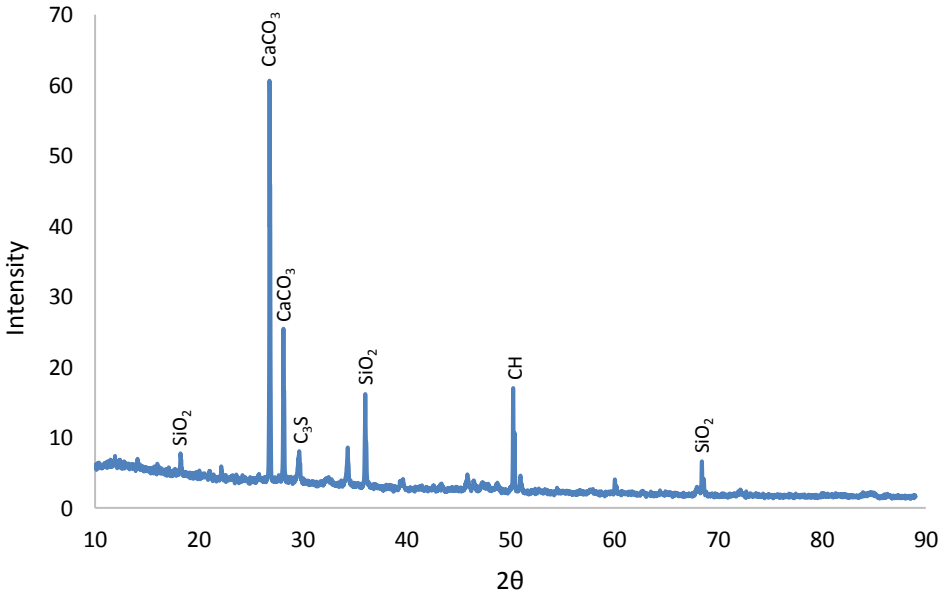

Fig. 14. XRD data of 5NC10PP.

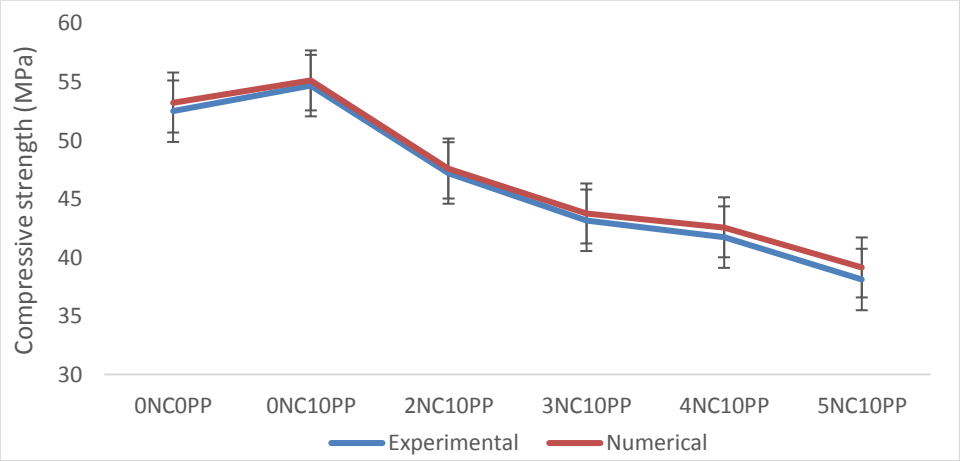

Fig. 15. Comparison of stresses for experimental and numerical approach.

5. Conclusions

This study examines how PET granules and nano-$CaCO_3$ affect the fresh, hardened, and microstructural properties of M40 concrete. PET granules were used to replace 10% of the fine aggregates, and nano-$CaCO_3$ was mixed with the cement on a volumetric basis. The PET granules were sized to closely match the river sand they replaced to reduce any effects from size differences. Based on the results, the following conclusions can be drawn:

- Adding up to 2% nano-$CaCO_3$ with PET granules did not affect the workability of the concrete mix. However, beyond this amount, the workability decreased with increasing nano-$CaCO_3$ content, although the reduction was minimal. Similarly, the density of the concrete decreased as more nano-$CaCO_3$ and PET granules were added, because PET is lighter than sand.
- Concrete with 10% PET granule content exceeded the target compressive strength for M40 concrete. The compressive strength of concrete increased by 4% with 10% PET granules compared to the standard mix. In contrast, concrete with 2% nano-$CaCO_3$ and 10% PET granule content achieved the target strength.
- The compressive strength of $CaCO_3$ concrete is slightly lower than that of standard concrete. This is due to $CaCO_3$ reacting with the C_3A phase of the cement to form carboaluminate, which partially replaces ettringite. Consequently, OPC concrete has a higher compressive strength at 28 days, when the concrete is fully cured. Since $CaCO_3$ is less reactive than cement, its replacement leads to a reduction in compressive strength, partly because $CaCO_3$ has minimal interaction with cement hydrates and does not provide the same long-term pozzolanic activity.
- The tensile strength declined with increasing nano-$CaCO_3$ content, although the change was relatively minor.
- The inclusion of PET granules up to a 10% replacement ratio positively impacted both flexural strength and toughness, with the greatest improvements observed in specimens containing 10% PET granules. However, when nano-$CaCO_3$ was added alongside PET, both flexural strength and toughness decreased.
- SEM images revealed a uniform distribution of $CaCO_3$ in the concrete mix, while the PET granules, being non-metallic and non-oxide, are not directly detectable by EDS but contribute to the mechanical and durability properties of the concrete.
- The XRD pattern provides a fingerprint of the crystalline components present in the concrete sample. By analyzing the peaks and their positions, one can deduce the presence and concentration of specific phases, such as calcium carbonate from the nano-$CaCO_3$ and other crystalline constituents of the concrete. The incorporation of nano-$CaCO_3$ and PET granules is aimed at improving the mechanical and durability properties of the concrete, which is reflected in the XRD pattern through the identified phases and their intensities.
- The results of this study, in terms of compressive strength, tensile strength, and flexural strength, were notably higher compared to findings reported in the literature, especially for concrete mixtures containing 10% PET granules.
- The compressive strength of concrete containing nano-$CaCO_3$ with PET granules was found to be nearly similar to the results predicted by ANSYS.

Acknowledgements

The authors would like to thank Institute of Engineering and Technology, Lucknow, India for the support regarding the experimental research.

Funding

The authors received no financial support for the research, authorship, and/or publication of this manuscript.

Conflict of Interest

The authors declare no potential conflicts of interest with respect to the research, authorship, and/or publication of this manuscript.

Data Availability

The datasets generated and/or analyzed during the current study are not publicly available but are available from the corresponding author upon reasonable request.

AI Assistance

No AI-based tools were used in the preparation of this manuscript.

Author Contributions

All authors made substantial contributions to the conception and design of the study, acquisition of data, analysis and interpretation of data; drafted or critically revised the manuscript for important intellectual content; and approved the final version to be published.

REFERENCES

Abu-Saleem M, Zhuge Y, Hassanli R, Ellis M, Rahman MM, Levett P (2021). Microwave radiation treatment to improve the strength of recycled plastic aggregate concrete. *Case Studies in Construction Materials*, 15, e00728.

Almeshal I, Tayeh B A, Alyousef R, Alabduljabbar H, Mohamed AM (2020). Eco-friendly concrete containing recycled plastic as partial replacement for sand. *Journal of Materials Research and Technology*, 9(3), 4631-4643.

Andrew RM (2018). Global CO_2 emissions from cement production. *Earth System Science Data*, 10, 195–217.

Asha S, Resmi PR (2015). Experimental research on concrete with straight and crimped waste plastic fibres. *International Journal of Engineering Sciences & Emerging Technologies*, 8(2), 55-71.

Aslani H, Pashmtab P, Shaghaghi A, Mohammadpoorasl A, Taghipour H, Zarei M (2021). Tendencies towards bottled drinking water consumption: Challenges ahead of polyethylene terephthalate (PET) *waste management*. *Health Promotion Perspectives*, 11(1), 60-68.

Azhdarpour AM, Nikoudel, MR, Taheri M (2016). The effect of using polyethylene terephthalate particles on physical and strength-related properties of concrete; a laboratory evaluation. *Construction and Building Materials*, 109, 55-62.

Bamigboye GO, Tarverdi K, Umoren A, Bassey DE, Okorie U, Adediran J (2021). Evaluation of eco-friendly concrete having waste PET as fine aggregates. *Cleaner Materials*, 2, 100026.

Batuecas E, Liendo F, Tommasi T, Bensaid S, Deorsola FA, Fino D (2021). Recycling CO_2 from flue gas for $CaCO_3$ nanoparticles production as cement filler: A life cycle assessment. *Journal of CO_2 Utilization*, 45, 101446.

Camiletti J, Soliman, AM, Nehdi ML (2013). Effects of nano- and micro-limestone addition on early-age properties of ultra-high-performance concrete. *Materials and Structures/Materiaux et Constructions*, 46, 881–898.

Cao M, Ming X, He K, Li L, Shen S (2019). Effect of macro-, micro-and nano-calcium carbonate on properties of cementitious composites—A review. *Materials*, 12(5), 781.

Choi YW, Moon DJ, Chung JS, Cho SK (2005). Effects of waste PET bottles aggregate on the properties of concrete. *Cement and Concrete Research*, 35(4), 776-781.

d'Amora M, Liendo F, Deorsola FA, Bensaid S, Giordani S (2020). Toxicological profile of calcium carbonate nanoparticles for industrial applications. *Colloids and Surfaces B: Biointerfaces*, 190, 110947.

Daniyal M, Akhtar S, Azam A (2019). Effect of nano-TiO2 on the properties of cementitious composites under different exposure environments. *Journal of Materials Research and Technology*, 8, 6158–6172.

Dawood AO, Hayder AK, Falih RS (2021). Physical and mechanical properties of concrete containing PET wastes as a partial replacement for fine aggregates. *Case Studies in Construction Materials*, 14, e00482.

Frigione M (2010). Recycling of PET bottles as fine aggregate in concrete. *Waste Management*, 30(6), 1101-1106.

Hashim AM, Nhabah HT (2018). Influence of $CACO_3$ with nanoparticles on the mechanical characteristics and concrete microstructure. *International Journal of Civil Engineering and Technology*, 9, 799–808.

Ismail ZZ, Al-Hashmi EA (2008). Use of waste plastic in concrete mixture as aggregate replacement. *Waste Management*, 28(11), 2041-2047.

Limami H, Manssouri I, Cherkaoui K, Saadaoui M, Khaldoun A (2020). Thermal performance of unfired lightweight clay bricks with HDPE & PET waste plastics additives. *Journal of Building Engineering,* 30, 101251.

Marangu JM, Thiong'o JK, Wachira JM (2019). Review of carbonation resistance in hydrated cement based materials. *Journal of Chemistry*, 2019(1), 8489671.

Moghadam MA, Mokhtarani N, Mokhtarani B (2009). Municipal solid waste management in Rasht City, Iran. *Waste Management*, 29(1), 485-489.

Pezzi L, De Luca PA, Vuono D, Chiappetta F, Nastro A (2006). Concrete products with waste's plastic material (bottle, glass, plate). In: *Materials Science Forum*, 514-516, 1753-0.

Rahmani E, Dehestani M, Beygi MHA, Allahyari H, Nikbin IM (2013). On the mechanical properties of concrete containing waste PET particles. *Construction and Building Materials*, 47, 1302-1308.

Saikia N, De Brito, J (2014). Mechanical properties and abrasion behaviour of concrete containing shredded PET bottle waste as a partial substitution of natural aggregate. *Construction and Building Materials*, 52, 236-244.

Siddique R, Khatib J, Kaur I (2008). Use of recycled plastic in concrete: A review. *Waste Management*, 28(10), 1835-1852.

Srivastava A, Mishra A, Singh S (2025). Mechanical and durability study of nano-SiO_2 and nano-TiO_2 on fiber reinforced concrete. *Challenge Journal of Concrete Research Letters*, 16(1), 33-39.

Srivastava A, Mishra A, Singh, SK (2025). Effect of nano TiO_2 and reinforcement of polypropylene fiber in standard concrete: an experimental and numerical approach. *Canadian Journal of Civil Engineering*, 52(5), 929-945.

Supit SWM, Shaikh FUA (2014). Effect of Nano-$CaCO_3$ on compressive strength development of high volume fly ash mortars and concretes. *Journal of Advanced Concrete Technology*, 12, 178–186.

Challenge Journal of CONCRETE RESEARCH LETTERS

Research Article

Effect of bacteria and fibers on the mechanical and structural behavior of self-healing fibrous concrete

Mina Medhat Youssef [a,*], Alaa Ali Bashandy [a], Rateb Nabil Abbas [b], Amal Abdel Hady Nasser [a]

[a] *Department of Civil Engineering, Menoufia University, 32511 Shebin ElKoum, Menofia, Egypt*
[b] *Department of Microbial Biotechnology, Genetic Engineering and Biotechnology Research Institute, University of Sadat City, 32897 Sadat City, Egypt*

ABSTRACT

The incorporation of bacteria into concrete has emerged as a promising strategy to enhance mechanical performance. This study presents a comprehensive experimental and numerical investigation into the behavior of fibrous concrete incorporating two bacterial strains—Bacillus megaterium (BM) and W1 at a dosage of 0.25% of cement weight, combined with either steel or polypropylene fibers. A multiscale experimental program was carried out, including compressive, tensile, and flexural tests, along with structural slab evaluation and analytical validation. Results revealed significant strength enhancements due to the steel fiber–BM combination, with compressive strength improvements of 42%, 52%, and 31% at 7, 28, and 90 days, respectively, compared to the control. Using polypropylene fiber–W1 mixes, recorded tensile strength gains reached nearly 19%. Flexural strength increased by up to 30% in 90 days, confirming the synergistic effect of fiber crack-bridging and bacterial precipitation. Structural performance was further assessed through four-point bending tests on reinforced slabs (1.0 m × 0.5 m × 0.05 m), where bacterial–fibrous concretes exhibited superior ductility and load capacity compared to the control. Reinforcing with steel plates proved more effective than glass fiber laminates, achieving 15–17% higher ultimate loads. A finite element model developed in Abaqus/CAE using the Concrete Damaged Plasticity model accurately replicated the experimental load–deflection responses, validating the proposed approach. Overall, the results demonstrate that integrating bacteria with fibers and external reinforcement can substantially enhance both material- and structural-scale performance, highlighting its potential for durable, high-performance concrete applications. These findings underline the potential of fibrous concrete as a sustainable, durable, and cost-effective solution for future structural applications.

ARTICLE INFO

Article history:
Received – October 6, 2025
Revision requested – November 10, 2025
Revision received – December 5, 2025
Accepted – December 11, 2025

Keywords:
Bacteria
Polypropylene fiber
Steel fiber
Glass fiber
Fibrous concrete
Self-healing concrete
Steel plates

Citation: Youssef MM, Bashandy AA, Abbas RN, Nasser AAH (2026). Effect of bacteria and fibers on the mechanical and structural behavior of self-healing fibrous concrete. *Challenge Journal of Concrete Research Letters*, 17(1), 13–29.

1. Introduction

For decades, engineers and scientists have strived to extend the service life of structures and components through research and innovation. One promising strategy is the development of bio-enhanced composite materials (Igbokwe et al. 2022). Concrete remains the most widely used material in the global construction industry due to its affordability, durability, high compressive strength, thermal mass, and versatility. However, concrete exhibits low tensile strength and high compressive strength, making cracking inevitable (Puranik et al. 2019). Once cracks appear, the lifespan of concrete structures can be significantly reduced. Although various crack repair methods exist, they are often costly and time-consuming. A major concern is the increased risk of

* *Corresponding author*. E-mail address: mina_medhat@sh-eng.menofia.edu.eg (M. M. Youssef)
ISSN: 2548-0928 / DOI: https://doi.org/10.20528/cjcrl.2026.01.002

structural failure caused by cracks under service conditions, which may result from factors such as general loading, drying shrinkage, creep, and thermal stresses (Ganesh et al. 2020). These cracks create pathways for aggressive chemicals and fluids to penetrate, leading to deterioration of the embedded reinforcement or cement matrix. Since cracking in concrete structures during their service life is unavoidable, enhancing material performance and potentially facilitating crack closure solutions has become essential. Self-healing involves the formation of solid substances within cracks through chemical or physical reactions, thereby blocking the ingress of harmful agents (Ji et al. 2020). Today, concrete continues to dominate infrastructure construction worldwide is provided by the works of Mutitu (2009) and Wachira et al. (2019).

In recent years, self-healing concrete has emerged as a promising innovation in the construction industry (de Brito and Kurda 2021). Concrete structures are often exposed to harsh environmental conditions that compromise durability, leading to expansion, cracking, and potential structural failures. These issues not only reduce service life but also increase maintenance costs and safety risks. To address these challenges, researchers have focused on developing smart concrete solutions that incorporate self-healing technologies to enhance resilience and longevity. Self-healing mechanisms are particularly beneficial in inaccessible or hazardous environments, where conventional repair methods are impractical. By autonomously sealing cracks and preventing the ingress of harmful agents, self-healing concrete offers a sustainable approach to maintaining structural integrity under demanding conditions (Helal et al. 2024). Later research focuses on biotechnology and civil engineering aspects of developing self-healing concrete. The global demand for buildings has driven the widespread use of concrete since the era of ancient Rome (Ryparova et al. 2021). However, conventional repair methods present several drawbacks, including operational limitations during reconstruction, mismatched thermal expansion between the base matrix and repair material, and potential environmental hazards (Griño et al. 2023).

The combination of fibers and bacteria accelerates the self-repair process in concrete. Bacteria such as Bacillus subtilis and Bacillus sphaericus produce calcium carbonate ($CaCO_3$) which fills the cracks, while fibers help in reducing crack width and providing a scaffold for the deposition of healing materials (Su et al. 2021).

The development of bio-based self-healing concrete seeks to minimize durability problems caused by cracking. Consequently, scientists are exploring various self-repair techniques (Ahmed et al. 2021; Mohammed et al. 2020; Ryparova et al. 2021; Xu et al. 2020). Innovative bio-materials that enhance calcite precipitation have been designed to facilitate the self-healing of cracks (İsar et al. 2023; Nasser et al. 2022; Nimafar et al. 2023; Ryparova et al. 2021; Singh et al. 2023). Incorporating specific microorganisms into cementitious materials is recognized as a cost-efficient and environmentally friendly approach for repairing micro-cracks. The microbial self-healing mechanism presents a highly promising solution, as it enables continuous crack healing, resulting in significant enhancement of the physico-mechanical properties of bio-concrete (Ahmed et al. 2021; Mohammed et al. 2020; Ryparova et al. 2021; Saridhe and Selvaraj 2021). Microbial-induced calcite precipitation (MICP) is a biological process in which specific microorganisms facilitate the formation of calcite through various mechanisms (Ryparova et al. 2021; Sadeghpour and Baradaran 2023). As a result, it enhances the mechanical and structural properties of concrete structures without the need for expensive or time-intensive repairs. The inclusion of fibers and bacteria improves the compressive strength, tensile strength, and flexural strength of concrete. For instance, the use of natural fibers like flax and coir has shown substantial improvements in crack-healing and compressive strength (Rauf et al. 2020). The bio-induced precipitation of calcite, driven by microbial metabolic activity within the concrete matrix, enhances material durability and represents a natural self-healing mechanism (Ahmed et al. 2021; Rossi et al. 2021; Roy et al. 2021). Microbial self-healing in bio-concrete typically involves two metabolic pathways: one through urea hydrolysis by Ureolytic bacteria and the other through respiration by non-Ureolytic bacteria (Rossi et al. 2021; Ryparova et al. 2021; Xu et al. 2020). In this context, Ureolytic bacteria like Bacillus megaterium and W1 have attracted significant attention in bio-cementation methods. Both bacterial strains are commonly found in soil and aquatic environments. They are Gram-positive, aerobic, rod-shaped, non-pathogenic organisms that exhibit urease activity and can tolerate highly alkaline conditions (Bakr et al. 2024; Su et al. 2021; Islam and Waseem 2023; Han et al. 2020). Certain bacterial species can hydrolyze urea into carbonate ions and ammonium (Nasser et al. 2022; Wang et al. 2023). The resulting ammonia increases the pH, which promotes calcite precipitation within micro-cracks, effectively sealing them (Tang and Xu 2021). Utilizing sustainable, eco-friendly biomaterials in construction offers an alternative to conventional chemical-based methods, reducing potential environmental and health risks (Ryparova et al. 2021; Nasser et al. 2022). In line with this approach, the present study aims to develop a novel sustainable bio-concrete incorporating ureolytic bacteria. The research evaluates the physical and mechanical properties of the bio-concrete at different curing stages and highlights the quantifiable improvements in compressive, tensile, and flexural performance attributed to the inclusion of bacteria and fibers. (Ahmed et al. 2021; Nasser et al. 2022; Zahran et al. 2014).Despite several studies on self-healing concrete, few investigations have compared the effects of multiple bacterial types combined with different fiber reinforcements. Moreover, limited research has addressed the correlation between mechanical properties at the material scale and structural performance. These gaps justify the current study, which aims to evaluate the combined effect of bacterial self-healing and fiber reinforcement on both material and structural behavior of concrete.

2. Research Significance

This research highlights the promising role of combining bacterial self-healing technology with fiber rein-

forcement in enhancing concrete performance. The research significance lies in providing a systematic understanding of the mechanical behavior and structural performance of self-healing concrete reinforced with fibers, as well as external reinforcement.

The novelties of this investigation are three points: (i) obtaining fibrous self-healing concrete using polypropylene fibers or steel fibers, (ii) a comparative study on the combined two bacterium types, Bacillus megaterium and W1, to obtain self-healing concrete, and (iii) the evaluation of the structural performance of fibrous self-healing concrete slabs. These findings will support researchers and engineers in adopting such a concrete type in construction practices. By validating these benefits, the study contributes to advancing innovative materials that align with the growing global demand for resilient and eco-friendly construction practices.

3. Experimental Program

The experimental program was designed to evaluate the mechanical performance of bio-concrete incorporating bacteria and fibers. The overall procedure is summarized in the flow chart (Fig. 1).

3.1. Materials

3.1.1. Cement

Ordinary Portland Cement (OPC, CEM I 42.5N) was used, sourced from El Sewedy Cement, Egypt. The specific Gravity is 3.15 (dimensionless). The cement complied with the requirements of the Egyptian Standard Specifications (E.S.S. 4756-1/2022 (2022)). A fixed cement content of 500 kg/m^3 was adopted for all mixes.

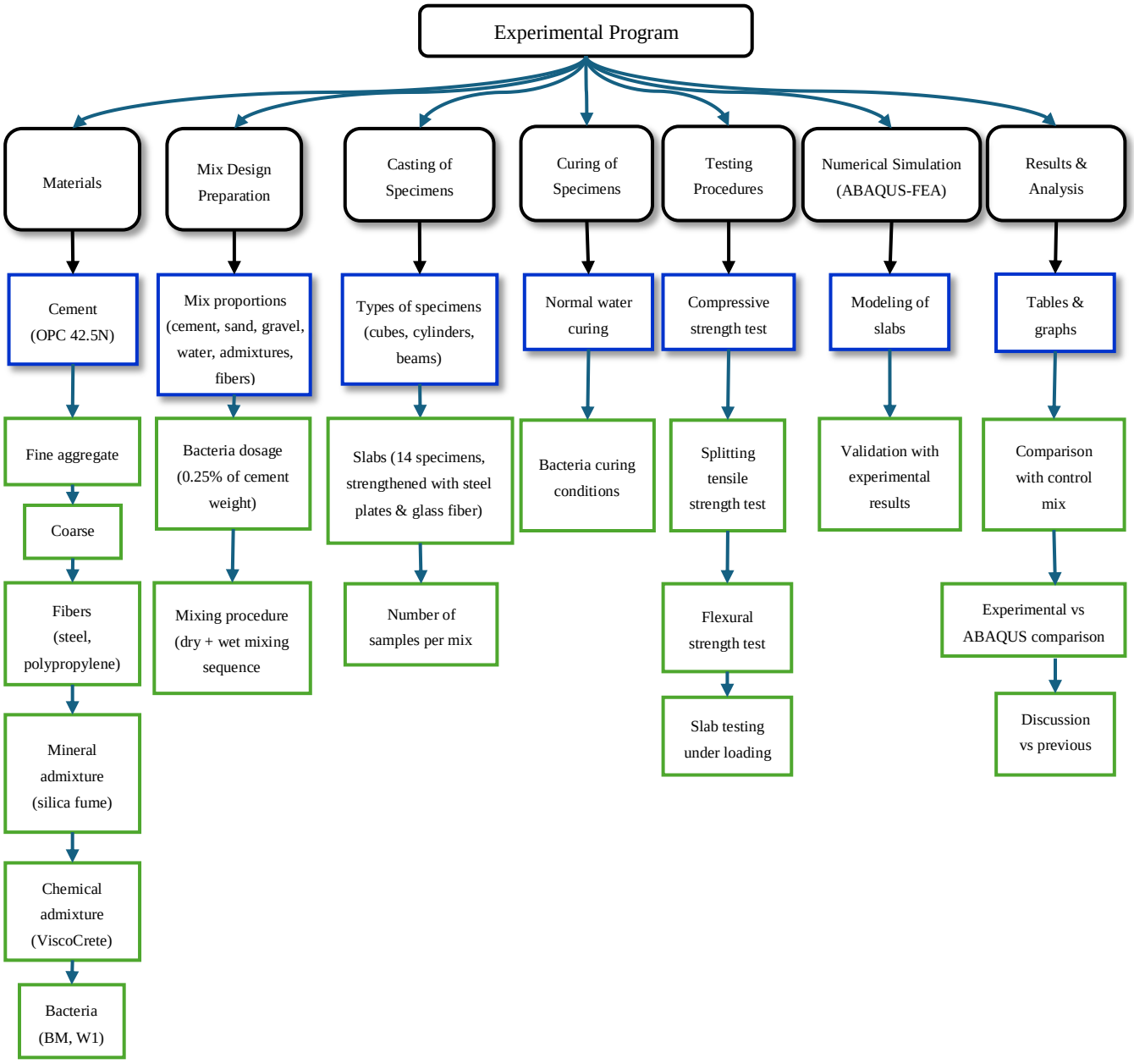

Fig. 1. Flow chart of research methodology.

3.1.2. Water

Fresh tap water, free from impurities, was used for casting and curing of all mixtures. The water-to-cement (W/C) is 0.42 for all mixes.

3.1.3. Fine aggregates

Well-graded sand was used as fine aggregate to minimize the void ratio. Standard characterization tests were conducted in accordance with ASTM procedures, including water absorption, specific gravity, and fineness modulus analysis. The results are presented in Table 1.

3.1.4. Coarse aggregates

Locally sourced crushed limestone with a maximum nominal size of 20 mm was employed as coarse aggregate. Characterization results for both fine and coarse aggregates are also summarized in Table 1.

Table 1. Physical properties of aggregate.

Physical property	Fine aggregate	Coarse aggregate
Specific gravity	2.60	2.62
Fineness modulus	2.36	4.1
Bulk density	1702 kg/m³	1456 kg/m³
Water absorption	0.85%	2%

3.1.5. Admixtures

Silica fume:

Silica fume (commercial product: Sika Fume, supplied by Sika Egypt) was incorporated as a supplementary cementitious material. The material consists of ultra-fine amorphous silicon dioxide particles with an average size of approximately 0.1 μm. In fresh concrete, silica fume enhances cohesion and water retention, while in hardened concrete, it chemically reacts with calcium hydroxide (free lime) released during cement hydration, forming additional calcium silicate hydrate (C–S–H) gel. This secondary hydration product densifies the microstructure and improves both strength and durability. The technical properties of the silica fume used in this study are summarized in Table 2.

Water-reducing admixture:

A high-range water-reducing admixture, Sika ViscoCrete®-3425, was used to enhance the workability of fresh concrete. This admixture is particularly suitable for producing mixes with high early strength development, significant water reduction, and superior flowability. It is chloride-free and does not contain any components that may accelerate steel reinforcement corrosion, thus making it appropriate for use in both reinforced and prestressed concrete. The main technical characteristics of Sika ViscoCrete®-3425 are provided in Table 3.

Table 2. Technical data of silica fume (obtained from the manufacturer).

Particle size (silicon dioxide)	~ 0.1 μm
Appearance / Color	Grey powder
Bulk density	300 kg/m³
Dosage	2–10% by weight of cement (in this product) for optimum results
SiO_2	≥ 85%
Specific gravity	2.3
Specific surface area	> 20 m²/g

Table 3. Technical data of superplasticizer used, "Sika ViscoCrete" (obtained from the manufacturer).

Base	Aqueous solution of modified polycarboxylates
Appearance/Color	Clear liquid
Density	1.08 kg/It (ASTM C494)
pH value	4.0
Solid content	40% by weight.

3.1.6. Fibers and plates

Steel (as internal and external reinforcement):

Steel fibers (Fig. 2) with a density of 7850 kg/m^3, a length of 3 cm, and an equivalent diameter of 0.2 mm were employed. These fibers exhibit an aspect ratio of 150. The fibers were procured from the Chemical for Modern Building Company, Egypt.

Steel plates (Fig. 2) with a thickness of 2 mm and a width of 5 cm along the slab span were employed as external reinforcement. The plates were sourced from locally fabricated by a certified metal workshop in Egypt.

Polypropylene fiber (as internal reinforcement):

The properties of polypropylene are governed by factors such as crystallinity, comonomer type and proportion, molecular weight, molecular weight distribution, and isotacticity. In this study, polypropylene fibers with a diameter of 0.05 mm, a length of 12 mm, and a density of 900 kg/m^3 were incorporated into bio-concrete. These fibers exhibit an aspect ratio of 240, a tensile strength of 400 MPa, and a modulus of elasticity of 3.5 GPa. The fibers were supplied by the Chemical for Modern Building Company, Egypt.

Glass fiber (as external reinforcement):

The CMB glass fiber is characterized by its lightweight nature, non-corrosiveness, and high durability. The fibers employed in this study had an average diameter of 14 μm, a length of 12 mm, a thickness of 1 mm, and a density of approximately 2,600 kg/m^3. They exhibit a tensile strength of 1,700 MPa and a modulus of elasticity ranging from 70 to 80 GPa. These fibers exhibit an aspect ratio of 857.

Fig. 2. Demonstration of the test materials.

3.1.7. Bacteria

Two bacterial strains were employed to induce microbial calcium carbonate precipitation (MICP) within the concrete matrix: Bacillus megaterium and strain W1. B. megaterium is a well-documented spore-forming bacterium widely recognized for its high urease activity, tolerance to alkaline environments, and compatibility with cementitious systems, whereas strain W1 was selected for its superior adaptability to harsh conditions and enhanced efficiency in calcium carbonate precipitation. Both strains are non-pathogenic, rod-shaped, Gram-positive bacteria capable of surviving the high-pH environment of concrete, as illustrated in Fig. 3. For cultivation, isolates were grown in Nutrient Broth (NB) medium containing 10 g/L peptone, 5 g/L sodium chloride (NaCl), and 10 g/L beef extract. To stimulate urease activity, the medium was supplemented with 20 g/L urea, and the pH was adjusted to 9.0–9.5 using 1 M NaOH. Cultures were incubated aerobically at 30 ± 2 °C in 2 L Erlenmeyer flasks under constant agitation at 150 rpm for 72–96 h. Growth was monitored by optical density at 600 nm (OD_{600}), and cells were harvested at OD ≈ 1.0 (≈10^8 CFU/mL), which was used as the working concentration for concrete mixing. To minimize contamination, bacterial suspensions were washed twice with sterile saline solution (0.9% NaCl) and resuspended in fresh medium immediately before use.

BM is gram-positive, spore-forming, effective at $CaCO_3$ precipitation, moderately alkali-tolerant. W1 is gram-negative, non-spore-forming, highly resistant to alkalinity and salinity, less studied but suitable for extreme conditions.

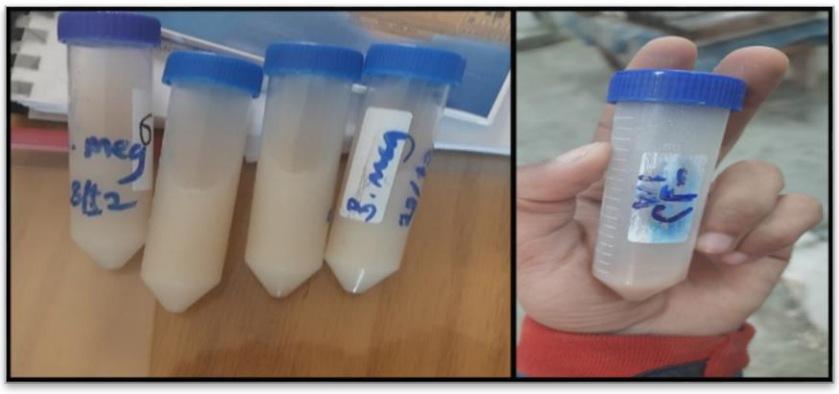

Fig. 3. Bacteria strains Bacillus megaterium and W1.

3.1.8. External reinforcement

Two types of reinforcement were used as external reinforcement for the slab samples used. Both reinforcement types were fixed on the bottom surface of the slabs (tension zone). The first type is steel plates with a thickness of 2 mm and a width of 5 cm along the slab span. Plates were fixed on the bottom surface of the slabs by using adhesive material to bond the concrete and steel plates. The adhesive used was Kima Poxy 165, which was obtained from the CMB Company in Egypt. The second type was glass fibre laminates, with the same width of steel plates (5 cm). Glass fibre laminates were fixed using polyester resin (Boytek).

3.2. Concrete mixing and mechanical testing

Concrete mixing was carried out in three successive stages. First, all dry constituents—including cement, fine aggregate, coarse aggregate, silica fume, and fibers—were blended for 2 min to ensure uniform distribution. In the second stage, 75% of the total mixing water, combined with the required dosage of superplasticizer (Sika ViscoCrete®-3425) and bacterial suspension (proportional to cement weight), was gradually added, followed by an additional 2 min of mixing. Finally, the remaining 25% of water, superplasticizer, and any residual fibers were incorporated, and mixing continued for 4 min until homogeneity was achieved. The fresh bio-concrete was cast into pre-oiled molds, compacted, demolded after 24 h, and then cured under controlled conditions until the designated testing ages. Additionally, the curing method under controlled conditions has been specified. All concrete specimens were cured at 26 ± 2 °C and 95% relative humidity for the designated curing period.

Six concrete mixes were prepared: a control mix, fiber-reinforced mixes using steel or polypropylene fibers, and bacteria-enhanced mixes using two bacterial strains (BM and W1) with and without fiber inclusion. All mixes contained a constant cement content of 500 kg/m^3, a W/C ratio of 0.42, and 10% silica fume replacement. The primary variable among the mixes was the type of fiber (steel or polypropylene) and the type of bacteria (BM or W1), added at 0.25% of cement weight. The mixed proportions are summarized in Table 4. The concrete mix proportions were designed according to ACI 211.1 (2009). The tests were conducted in accordance with ASTM C1609 (2019) using a displacement-controlled rate of 0.5 mm/min. Mechanical performance was evaluated in accordance with ES 1072/2008 (2008), ES 1658/2018 (2018), as follows:

- Compressive strength: Cubic specimens (100 × 100 × 100 mm) were tested after 7, 28, and 90 days. Reported values represent the mean of three replicates.
- Splitting tensile strength: Cylindrical specimens (100 × 200 mm) were tested after 28 and 90 days, with results averaged from three replicates.
- Flexural strength: Prismatic specimens (100 × 100 × 500 mm) were subjected to three-point bending in accordance with ASTM E399 (2020) at 28 and 90 days.
- Slab samples: Fourteen slab specimens (1000 × 500 × 50 mm with an effective span of 960 mm) were cast to evaluate structural performance. All slab, tested under four-point bending, up to failure. The slabs rested on two supports, a hinged one and a roller one. One slab was tested as a control slab. The other slabs were reinforced using two reinforcement methods: glass fiber laminates bonded with polyester resin (Boytek) and steel plates bonded with structural epoxy adhesive (CMB Epoxy 165). The reinforcing scheme is illustrated in Fig. 4. Effective span is 900 mm with simply supported boundary conditions allowing free rotation but no vertical displacement.

Table 4. Content of concrete mixes.

Mix	Cement (kg/m^3)	Water (kg/m^3)	Aggregates (kg/m^3)		Admixtures (kg/m^3)		Fiber type & dosage (volume fraction)	Bacteria type (by weight of cement)
			Coarse aggregate	Fine aggregate	Visco-Crete	Silica fume		
Control mix	500	210	1000	640	4	50	–	–
Mix 1 (ST)	500	210	1000	640	4	50	Steel fiber 0.3% (23.5 kg/m^3)	–
Mix 2 (PP)	500	210	1000	640	4	50	Polypropylene fiber 0.3% (2.7 kg/m^3)	–
Mix 3 (BMS)	500	210	1000	640	4	50	Steel fiber 0.3% (23.5 kg/m^3)	BM (0.25%)
Mix 4 (BMP)	500	210	1000	640	4	50	Polypropylene fiber 0.3% (2.7 kg/m^3)	BM (0.25%)
Mix 5 (W1S)	500	210	1000	640	4	50	Steel fiber 0.3% (23.5 kg/m^3)	W1 (0.25%)
Mix 6 (W1P)	500	210	1000	640	4	50	Polypropylene fiber 0.3% (2.7 kg/m^3)	W1 (0.25%)

Fig. 4. Glass fiber laminates and steel plate as external reinforcement.

4. Test Results

4.1. Fresh concrete properties

The flowability of fresh concrete mixes was assessed using the slump-flow spread test, and the measured values are reported in mm. Although some mixes exhibited high spread values, the concrete was not classified as self-compacting concrete (SCC). The slump-flow measurements are presented only as relative indicators of mixture flowability, and no segregation was observed during casting. The presence of high-range water-reducing admixtures (superplasticizers) and fibers can significantly influence workability. In this method, fresh concrete was placed in a cone mold, which was then lifted vertically to allow free spreading of the mix. The average spread diameter was determined by measuring in two perpendicular directions. Spread of fresh concrete is measured to indicate relative flowability. The mixes were not classified as self-compacting concrete (SCC); values are presented as indicators of workability only in Fig. 5, and the flowability results for bio-concrete mixes are summarized in Table 5.

Fig. 5. Flowability of fibrous bio-concrete.

Table 5. Flowability of bio-concrete.

Mix	Control	Mix 1 (ST)	Mix 2 (PP)	Mix 3 (BMS)	Mix 4 (BMP)	Mix 5 (W1S)	Mix 6 (W1P)
Flow (mm)	650	730	600	600	550	620	570

4.2. Hardened concrete properties

Structural performance was assessed based on slab deflection, ultimate load, and first cracking load. Compressive strength results at 7, 28, and 90 days, as well as splitting tensile and flexural strengths at 28 and 90 days, are summarized in Table 6. The mechanical properties of hardened concrete for the six investigated mixes are presented in Table 6.

Table 6. Mechanical properties of hardened concrete (MPa).

Mix	Compressive strength			Splitting tensile strength		Flexural strength	
	7 days	28 days	90 days	28 days	90 days	28 days	90 days
Control	26.67	34.33	44.67	2.34	2.44	2.67	3.55
Mix 1	33.67	46.33	58.30	2.65	2.87	3.04	4.35
Mix 2	35.00	45.00	51.33	2.61	2.65	2.70	4.35
Mix 3	33.67	49.00	51.67	2.60	2.70	3.74	4.49
Mix 4	31.00	45.33	50.00	2.65	2.76	3.21	4.94
Mix 5	42.30	52.67	58.67	2.50	2.79	3.04	4.80
Mix 6	37.67	52.00	54.00	2.44	2.90	3.31	4.82

4.2.1. Compressive strength

The compressive test setup is illustrated in Fig. 6. The average compressive strength of different mixes at 7, 28, and 90 days is shown in Fig. 7. Conventional concrete achieved strengths of 26.6, 34.3, and 44.6 MPa at these ages, respectively. All modified mixes exhibited higher values, with improvements ranging from 15% to 59% compared to the control, as follows:

- Steel fiber mix: 33.6, 46.3, and 58.3 MPa at 7, 28, and 90 days, reflecting increases of 26.3%, 34.9%, and 30.7%.
- Polypropylene fiber mix: 35, 51, and 51.3 MPa, with gains of 31.5%, 48.6%, and 15%.
- Bacillus megaterium + Steel fiber: 33.6, 49, and 51.6 MPa, corresponding to increases of 26.3%, 42.8%, and 15.6%.
- Bacillus megaterium + Polypropylene fiber: 31, 45.3, and 61 MPa, yielding improvements of 16.5%, 32%, and 36.7%.
- Bacterial W1 + Steel fiber (Mix 5): 42.3, 52.6, and 58.6 MPa, the highest overall gains of 59%, 53%, and 31%.
- Bacterial W1 + Polypropylene fiber: 37.6, 52, and 54 MPa, showing increases of 41.3%, 51.6%, and 21%.

Notably, the maximum strength of the control mix (34.3 MPa at 28 days) was matched or exceeded by bacterial–fiber concretes within just 7 days of curing, highlighting the enhanced bonding and accelerated strength development due to the fiber–bacteria interaction.

Overall, compressive strength results confirmed substantial improvements for all modified mixes. The predicted maximum load at failure closely matched the experimental ultimate load. The highest strength was obtained in Mix 5 (W1 + Steel fibers), reaching 58.67 MPa at 90 days, a 31.3% increase over the control. This enhancement is attributed to the synergistic effect of steel fibers (improved crack-bridging) and bacterial activity (calcium carbonate precipitation and densification of the microstructure).

These findings are consistent with previous studies (Helal et al. 2024; Mostofinejad et al. 2022), which reported strength gains above 37% when bacterial treatment was combined with steel fibers. Long-term studies extending to 180 days have even shown increases exceeding 45% using similar hybrid approaches.

Fig. 6. Compressive strength test.

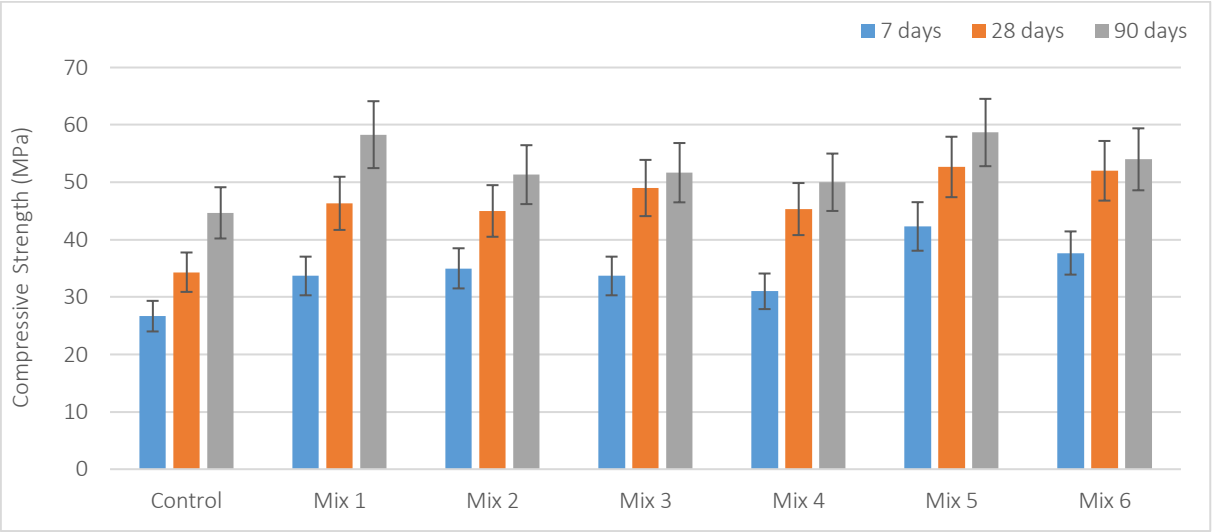

Fig. 7. The compressive strength test results.

4.2.2. Flexural strength

The loading test using the three-point loading system is illustrated in Fig.8. The mean flexural strength values of the tested mixes at 28 and 90 days are presented in Fig. 9. Conventional concrete achieved 2.66 MPa and 3.50 MPa at 28 and 90 days, respectively. All modified mixes exhibited higher values, with notable improvements depending on the type of fiber and bacterial addition, as follows:

- Steel fiber mix: 3.04 and 4.30 MPa, representing increases of 14.3% and 22.8%.
- Polypropylene fiber mix: 2.70 and 4.35 MPa, with gains of 1.5% and 24.2%.
- Bacillus megaterium + Steel fiber: 3.74 and 4.49 MPa, yielding improvements of 40% and 28.2%.
- Bacillus megaterium + Polypropylene fiber: 3.22 and 4.94 MPa, with increases of 21% and 41.1%.
- Bacterial W1 + Steel fiber: 3.04 and 5.87 MPa, the highest gain at 90 days, corresponding to 14.2% and 67.6%.
- Bacterial W1 + Polypropylene fiber: 3.31 and 4.82 MPa, showing 24.4% and 37.7% improvements.

A key observation is that the flexural strength attained by conventional concrete at 90 days was reached by bacterial fiber-reinforced concrete within 28 days, demonstrating accelerated strength development due to the synergistic effect of bacterial activity and fiber reinforcement.

Prism tests confirmed these findings, with the control mix recording 3.55 MPa at 90 days. The maximum value was observed in Mix 4 (BM + polypropylene fiber), reaching 4.94 MPa, a 39.15% increase over the control. The enhanced performance can be attributed to the combined action of fibers—which improve ductility and post-cracking load-carrying capacity—and bacterial activity, which refines the microstructure through calcium carbonate precipitation, thereby enhancing stiffness and toughness.

These results align well with previous studies (Helal et al. 2024), which reported flexural strength increases of up to 50% for bacterial concrete reinforced with steel fibers. The consistency of outcomes reinforces the evidence that microbial self-healing coupled with fiber reinforcement produces a significant synergistic effect, making bio-concrete a promising solution for durable structural applications.

Fig. 8. Flexural strength samples and test setup using a three-point loading system.

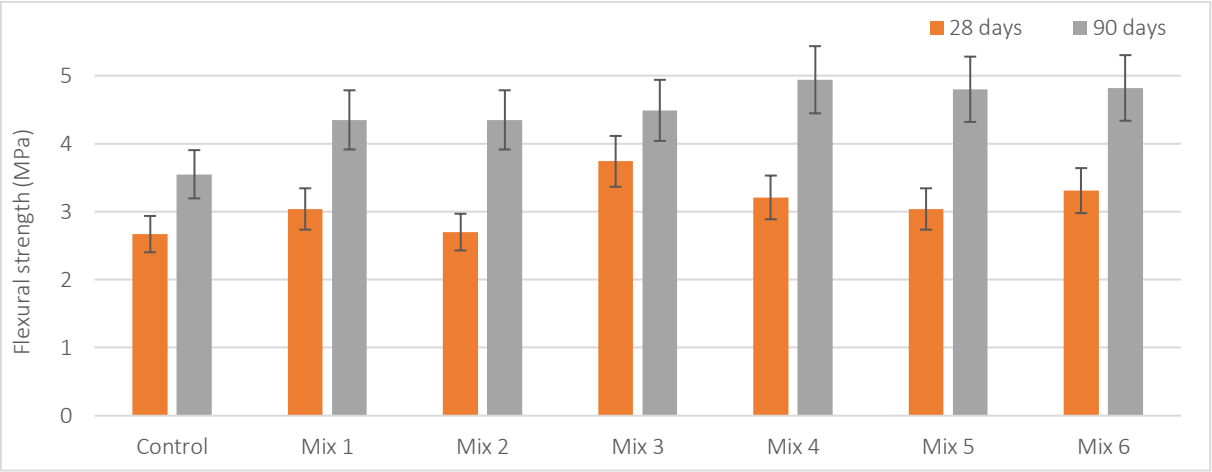

Fig. 9. The flexural strength test results.

The incorporation of fibers and bacterial strains significantly enhanced both compressive and flexural strengths of concrete, as shown in Table 7. Steel and polypropylene fibers improved load-bearing capacity and ductility by bridging microcracks, while bacterial activity (Bacillus megaterium and W1) promoted calcium carbonate precipitation, densifying the matrix and accelerating strength development.

Notably, W1-based mixes combined with steel fibers achieved the highest gains, with compressive and flexural strengths increasing up to 53% and 67.6%, respectively, and reaching conventional 90-day performance within 28 days. These results confirm a synergistic effect between fiber reinforcement and microbial self-healing, consistent with previous studies reporting 37–50% improvements under similar hybrid approaches (Helal et al. 2024; Mostofinejad et al. 2022). The findings highlight the potential of bacterial fiber-reinforced concrete for applications requiring early-age strength and enhanced durability.

Table 7. Effect of fiber reinforcement and bacterial addition on concrete mechanical properties.

Mix	Description	Compressive strength (MPa)	Increase vs. Control	Flexural strength (MPa)	Increase vs. Control
Control	Control mix	34.3 (28d)	–	3.50 (28d)	–
Mix 1	Steel fiber	46.3	34.9%	4.30	22.8%
Mix 2	Polypropylene fiber	51.0	48.6%	4.35	24.2%
Mix 3	BM + Steel fiber	49.0	42.8%	4.49	28.2%
Mix 4	BM + Polypropylene fiber	45.3	32.0%	4.94	41.1%
Mix 5	W1 + Steel fiber	52.6	53.0%	5.87	67.6%
Mix 6	W1 + Polypropylene fiber	52.0	51.6%	4.82	37.7%

4.2.3. Indirect tensile strength

The splitting tensile test setup is illustrated in Fig. 10. The mean splitting tensile strength of the tested concrete mixes at 28 and 90 days is presented in Fig. 11. Conventional concrete exhibited values of 2.34 MPa and 2.44 MPa at 28 and 90 days, respectively. All modified mixes showed improved performance, with the magnitude of increase depending on the type of fiber and bacterial addition:

- Steel fiber: 2.65 and 2.87 MPa (+13.2%, +17.6%).
- Polypropylene fiber: 2.76 and 2.65 MPa (+17.9%, +8.6%).
- Bacillus megaterium + Steel fiber: 2.60 and 2.70 MPa (+11.1%, +10.6%).
- Bacillus megaterium + Polypropylene fiber: 2.65 and 2.76 MPa (+13.2%, +13.1%).
- W1 + Steel fiber: 2.50 and 2.50 MPa (+6.8%, +2.5%).
- W1 + Polypropylene fiber: 2.44 and 2.90 MPa (+4.2%, +18.9%), achieving the highest tensile strength overall.

The results demonstrate that fiber addition enhances tensile capacity due to its inherent mechanical properties, while bacterial incorporation contributes further improvements via microbial calcium carbonate precipitation, which densifies the matrix and fills nanopores. Notably, Mix 6 (W1 + polypropylene fiber) recorded the highest 90-day splitting tensile strength of 2.90 MPa, representing an 18.8% increase over the control. Steel fiber mixes also showed substantial gains, reaching 2.87 MPa in 90 days (17.6% improvement).

These observations align with previous studies (Helal et al. 2024; Hosseinzadeh et al. 2023), where bacterial activity combined with fiber reinforcement enhanced splitting tensile strength by 17–31% over conventional concrete, confirming the synergistic effect of fibers and microbial self-healing in improving concrete tensile performance.

Fig. 10. Splitting tensile strength molds and test setup.

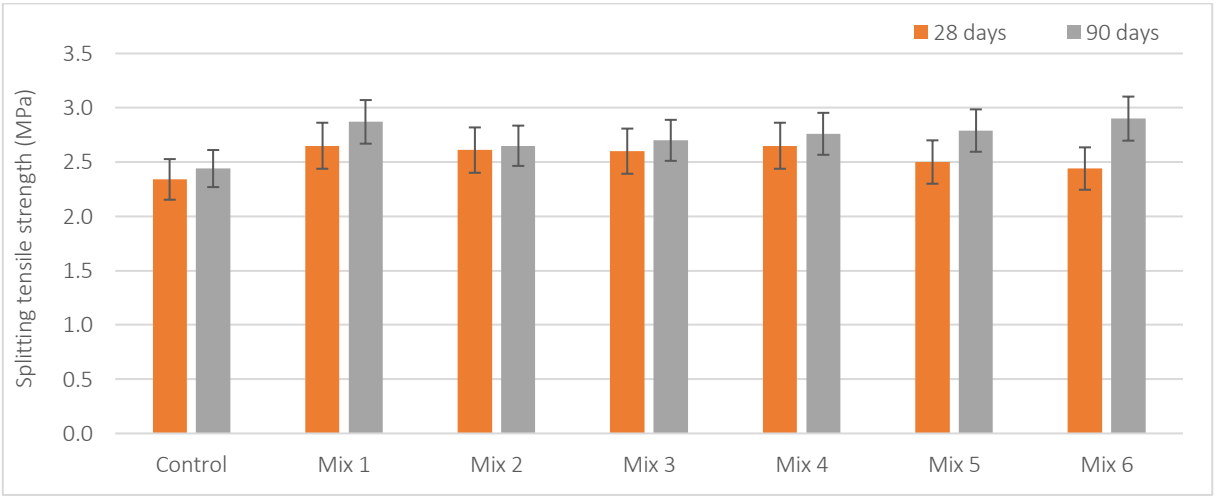

Fig. 11. Splitting tensile strength test results.

4.3. Behavior of fibrous self-healing concrete slabs

To evaluate the relative effectiveness of internal fiber reinforcement versus external reinforcement, a total of 14 concrete slabs were cast and tested under a four-point bending setup (Fig. 12). Internal reinforcement was provided by steel or polypropylene fibers incorporated into the concrete matrix, while external reinforcement involved bonding steel plates or glass fiber sheets to the slab surface. Two dial gauges were installed on each slab to measure vertical deflections at mid-span and beneath a loading point, capturing both global and localized responses. The resulting load–deflection curves (Figs. 13–15) illustrate the influence of different reinforcement strategies on stiffness, ductility, and ultimate load capacity.

The experimental results indicate that fiber-reinforced concrete slabs showed improved flexural strength and crack control compared to unreinforced control slabs, achieving higher loads before the onset of cracking. However, slabs externally strengthened with steel plates or glass fibers demonstrated significantly greater ultimate loads and reduced deflections, highlighting the effectiveness of external reinforcement in enhancing structural capacity. Notably, the combination of bacterial fiber-reinforced concrete with external reinforcement produced the highest load-bearing capacity, suggesting that internal fibers and microbial self-healing provide beneficial pre-crack microstructural improvements, which are further amplified by externally applied reinforcement.

These findings underscore the complementary roles of internal fiber reinforcement and external reinforcement: fibers enhance early-age strength, ductility, and self-healing, while external reinforcements allow substantial increases in ultimate flexural capacity, making them particularly valuable for retrofitting or strengthening applications.

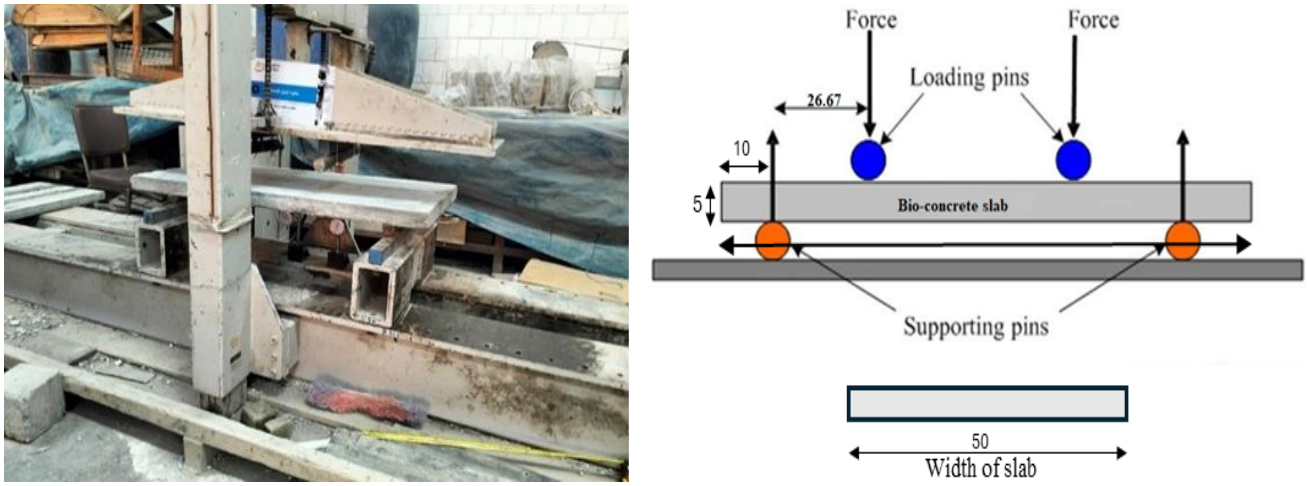

Fig. 12. Four-point loading test setup for slab samples.

Table 7 presents the experimental results for 14 slabs, including ultimate load and displacements/deflection at ultimate load. Fig. 13 shows the cracking patterns of the tested slabs, while Figs. 14 and 15 show the load-displacement curves. Each slab configuration was tested with external steel plates and glass fiber sheets to assess the influence of reinforcement on flexural performance. Across all six mixes (Table 7), slabs reinforced with steel plates consistently exhibited higher ultimate load capacities compared to those strengthened with glass fiber laminates, showing increases of approximately 15–30% over the control mix.

These results align with previous studies (İsar et al. 2023; Xie et al. 2025), which reported ultimate loads of 96.3 kN for steel-reinforced slabs versus 83.7 kN for GFRP-reinforced slabs, corresponding to a performance advantage of 15–17% in favor of steel reinforcement. The findings confirm that steel plate reinforcement provides superior flexural and impact resistance compared to GFRP-based systems, highlighting its effectiveness for structural enhancement of slabs.

Each slab configuration was tested with external steel plates and glass fiber sheets to evaluate the effect of reinforcement type on flexural behavior. Across all six mixes (Table 7), steel plate–strengthened slabs consistently demonstrated 15–30% higher ultimate load capacities than both the control and their glass fiber–strengthened counterparts. These findings are consistent with prior research (İsar et al. 2023; Xie et al. 2025), which reported ultimate loads of 96.3 kN for steel-reinforced slabs versus 83.7 kN for GFRP-reinforced slabs, a 15–17% performance advantage in favor of steel reinforcement. Overall, the results confirm that steel plate reinforcement outperforms GFRP systems in terms of flexural and impact resistance, making it a more effective technique for structural slab enhancement.

The load–deflection responses exhibited clear distinctions among the mixes. Steel fiber reinforcement (Mix 1) produced higher peak loads and pronounced ductility, whereas PP fibers (Mix 2) primarily enhanced post-cracking deformation with modest strength gains. Hybrid mixes with steel fibers and bacteria (Mixes 3 and 5) achieved the greatest improvements in ductility and load capacity, reflecting the reported synergy that elevates compressive, tensile, and flexural strengths by up to 55%, 80%, and 50%, respectively. PP fibers with bacteria (Mixes 4 and 6) also improved ductility but attained lower peak loads than their steel-fiber counterparts. Overall, the steel fiber–bacteria system provided the most effective enhancement, combining increased stiffness with superior toughness.

Each slab configuration was tested with external steel plates and glass fiber sheets to evaluate the effect of strengthening type on flexural behavior. Across all six mixes (Table 8), steel plate–strengthened slabs consistently demonstrated 15–30% higher ultimate load capacities than both the control and their glass fiber–strengthened counterparts. These findings are consistent with prior research (İsar et al. 2023; Xie et al. 2025), which reported ultimate loads of 96.3 kN for steel-reinforced slabs versus 83.7 kN for GFRP-reinforced slabs, a 15–17% performance advantage in favor of steel reinforcement. Overall, the results confirm that steel plate strengthening outperforms GFRP systems in terms of flexural and impact resistance, making it a more effective technique for structural slab enhancement.

The load–deflection responses exhibited clear distinctions among the mixes. Steel fiber reinforcement (Mix 1) produced higher peak loads and pronounced ductility, whereas PP fibers (Mix 2) primarily enhanced post-cracking deformation with modest strength gains. Hybrid mixes with steel fibers and bacteria (Mixes 3 and 5) achieved the greatest improvements in ductility and load capacity, reflecting the reported synergy that elevates compressive, tensile, and flexural strengths by up to 55%, 80%, and 50%, respectively. PP fibers with bacteria (Mixes 4 and 6) also improved ductility but attained lower peak loads than their steel-fiber counterparts. Overall, the steel fiber–bacteria system provided the most effective enhancement, combining increased stiffness with superior toughness.

It should be noted that this study does not provide direct microstructural evidence of bacterial-induced $CaCO_3$ precipitation; however, the observed improvements in mechanical properties are based on experimental observations and supported by findings from previous studies.

Mix	Steel plates	Glass fiber laminates
Control	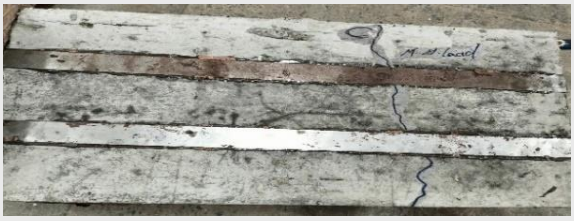	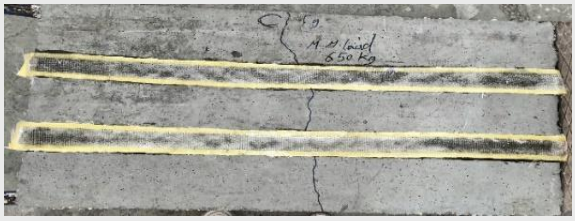
Mix 1		
Mix 2		
Mix 3		
Mix 4	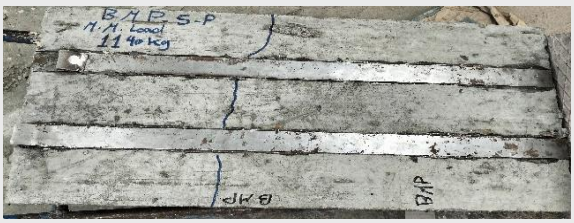	
Mix 5		
Mix 6		

Fig. 13. Cracking pattern of investigated slabs.

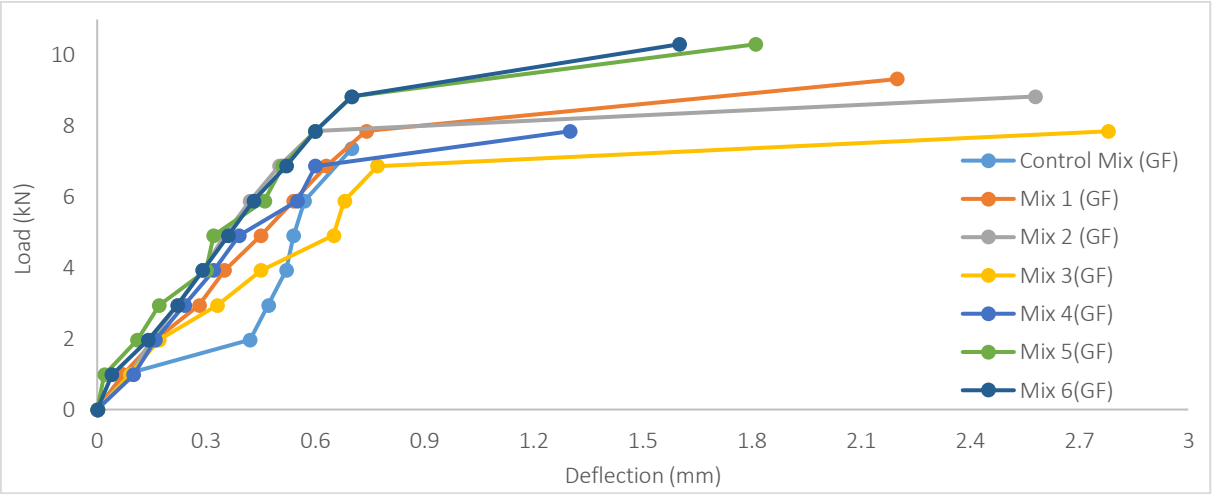

Fig. 14. Load-deflection curve when using glass fiber laminates as external reinforcement.

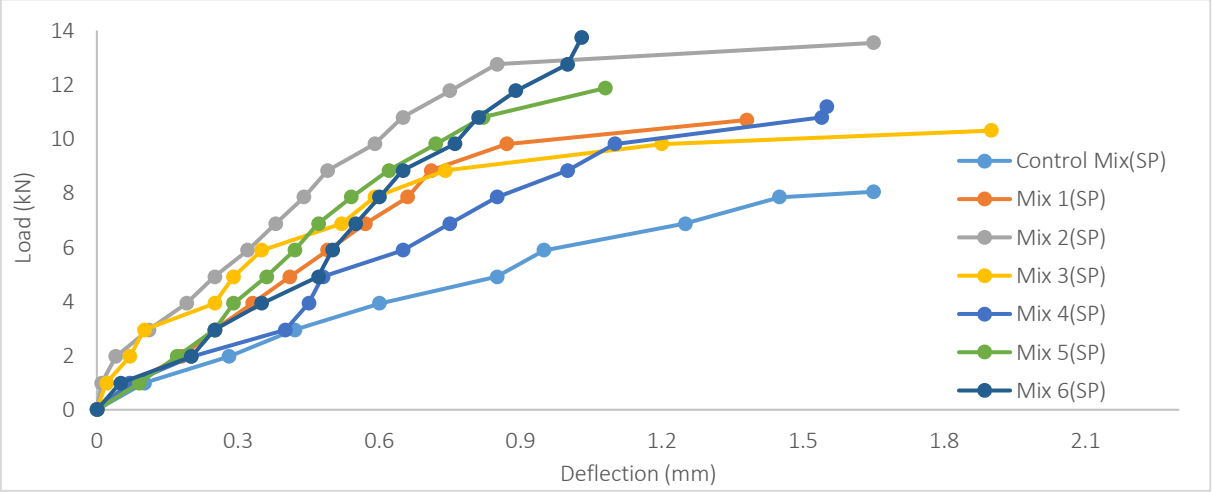

Fig. 15. Load-deflection curve when using steel plates as external reinforcement.

Table 8. Comparison between internal and external reinforcement of slabs under a four-point loading system.

Slab no.	Internal reinforcement	External reinforcement	Ultimate load (kN)	Mid-span deflection at failure (mm)	Notes
1	None (Control)	Steel plate	8.04	0.8	Baseline
2	Steel fiber	Steel plate	10.69	2.2	Improved ductility
3	Polypropylene fiber	Steel plate	13.54	2.58	Moderate improvement
4	Bacillus megaterium + Steel fiber	Steel plate	10.3	2.78	Enhanced microstructure
5	Bacillus megaterium + Polypropylene fiber	Steel plate	11.18	1.55	Moderate gain
6	W1 + Steel fiber	Steel plate	12.65	1.81	High early-age strength
7	W1 + Polypropylene fiber	Steel plate	13.74	1.03	Highest tensile gain among fibers
8	None (Control)	Glass fiber sheet	7.36	0.6	Significant ultimate load increase
9	Steel fiber	Glass fiber sheet	9.32	1.38	Synergistic improvement
10	Polypropylene fiber	Glass fiber sheet	8.83	1.65	Moderate load gain
11	Bacillus megaterium + Steel fiber	Glass fiber sheet	8.04	1.9	Moderate load gain
12	Bacillus megaterium + Polypropylene fiber	Glass fiber sheet	7.85	1.3	High ultimate load
13	W1 + Steel fiber	Glass fiber sheet	10.3	1.08	Stiffness improvement
14	W1 + Polypropylene fiber	Glass fiber sheet	10.3	0.7	Maximum ultimate load

5. Numerical Simulation

5.1. Geometry and boundary conditions

The numerical model was developed to replicate the experimental four-point bending test of reinforced concrete slabs with dimensions of 1.0 m × 0.5 m × 0.05 m. Simply supported boundary conditions were applied at both slab ends, and the load was introduced at two symmetrically placed points, each located 26.67 cm from the supports. This ensured full consistency between the experimental and numerical configurations. Fig. 16 shows the slab model in Abaqus.

5.2. Material modeling

Concrete behavior was represented using the Concrete Damaged Plasticity (CDP) model in Abaqus/CAE, which captures both tensile cracking and compressive crushing. Steel reinforcement was modeled as embedded truss elements with elastic–plastic properties, fully bonded to the concrete matrix. Material parameters for both concrete and reinforcement were derived from experimental tests to ensure accuracy.

5.3. Loading and analysis procedure

Incremental loading was applied through two concentrated forces at the same locations as in the laboratory setup. A static general analysis was performed to capture nonlinear stress–strain behavior, stiffness degradation, and crack propagation. Outputs included stress distribution, crack initiation and growth, mid-span deflection, and ultimate load capacity.

5.4. Model validation

The predicted load–deflection response and ultimate load capacity from the FE model showed close agreement with the experimental results. This confirmed that the developed model could reliably reproduce slab flexural performance and failure mechanisms. Table 9 shows a Comparison of Experimental and Numerical Results for Control and Mix 5.

5.5. Parametric analysis

To extend the experimental findings, a limited parametric analysis was carried out by comparing the control mix with Mix 5 (W1 + steel fiber + bacteria). This comparison focused on the influence of bacterial self-healing and polypropylene fibers on flexural performance. The analysis highlighted clear differences in load capacity, stiffness, and crack propagation patterns, providing insight into the synergistic contribution of microbial activity and fiber reinforcement.

5.6. Material properties

5.6.1. Concrete

The concrete used in the numerical model had a compressive strength of 35 MPa, an elastic modulus of 30 GPa, a Poisson's ratio of 0.2, a density of 2400 kg/m^3, and its stress–strain behavior was represented using the Madrid–Barbora model.

5.6.2. Steel plates

The steel plates used in the numerical model were defined using linear elastic properties with a Young's modulus of 225 GPa, Poisson's ratio of 0.25, and a density of 7850 kg/m^3.

5.6.3. Concrete stress–strain relationship

The nonlinear compressive behavior of concrete in the FE model was defined using the Madrid Parabola stress–strain relationship. This model captures both the ascending branch up to the peak compressive stress and the descending softening branch after cracking. A compressive strength of 35 MPa and peak strain 0.002 were used, with an elastic modulus calculated as $E_c = 4700\sqrt{f'c}$, and Poisson's ratio 0.2. In tension, concrete was modeled as linear elastic up to $f_t = 3.2$ MPa, followed by a tension-stiffening softening curve. The Concrete Damaged Plasticity (CDP) model was used with standard parameters ($\psi = 35°$, eccentricity = 0.1, $f_{b0}/f_{c0} = 1.16$, $K = 0.667$, viscosity = 0.0005), calibrated to match the experimental response.

The numerical model has been updated to clearly specify the element types used for each component, where concrete was modeled using 3D solid elements and steel plates using linear elastic shell/solid elements, as appropriate.

The GFRP and strengthening schemes were not included in the numerical model because the FE simulation was intended only to validate the experimental response of the control slab and Mix 5. The objective was to verify load–deflection behavior rather than simulate strengthening mechanisms.

The FEM predictions showed strong agreement with the experimental load–deflection behavior for both slabs, confirming the accuracy of the numerical modeling approach.

6. Conclusions

Based on the experiments conducted in this study to evaluate the main mechanical properties as well as the structural performance of fibrous self-healing slabs, the following conclusions can be drawn:

- Integrating bacterial self-healing agents with fibers markedly enhanced both the mechanical properties and structural performance of reinforced concrete slabs compared to the Control Mix at 90 days. The combined action of bacterial calcium carbonate precipitation and fiber crack-bridging was identified as the primary mechanism driving these improvements.
- Among the tested mixes, steel fiber–bacteria concretes achieved the highest compressive strength, with Mix 5 recording a 31.3% gain, while polypropylene fiber–bacteria concretes showed the greatest increase in splitting tensile strength, with Mix 6 achieving an 18.8% improvement.

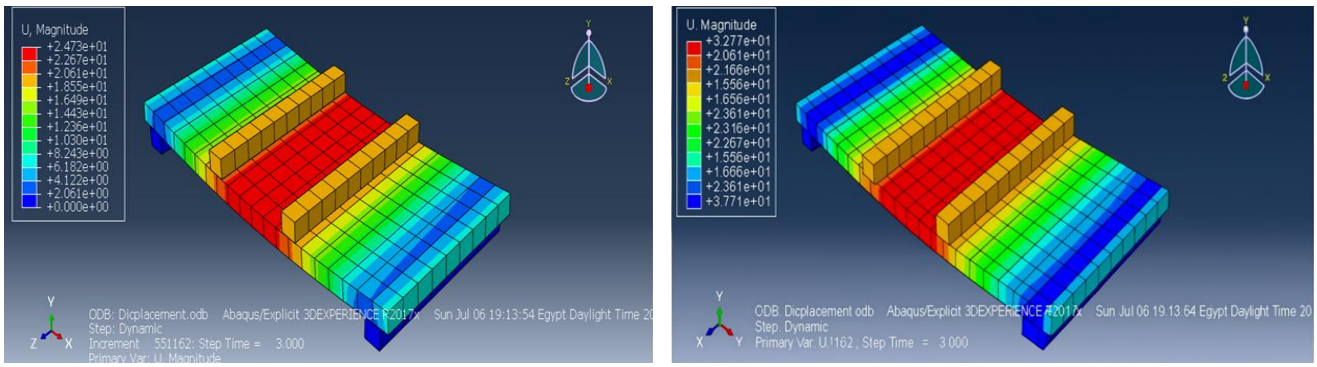

Fig. 16. Slab model simulations in Abaqus (Control Slab and Mix 5).

Table 9. Comparison between experimental and numerical results for Control Mix and Mix 6.

Mix	Ultimate load – Exp. (kN)	Ultimate load – FEM (kN)	Mid-span deflection at peak – Exp. (mm)	Mid-span deflection at peak – FEM (mm)	Stiffness trend	Remarks
Control	8.04	8.93	0.8	0.88	Lower stiffness, brittle failure	Rapid crack propagation, limited ductility
Mix 5 (W1 + SF + Bacteria)	12.65	14.22	1.03	1.12	Higher stiffness, ductile response	Enhanced crack control, delayed failure

- Flexural strength was also significantly enhanced, with Mix 4 reaching a 39.2% increase relative to the control. These findings align with previous reports that the hybrid approach of microbial self-healing and fiber reinforcement can improve concrete strength by more than 30–40% within 90 days, with potential for even greater long-term benefits.
- At the structural level, reinforcing slabs with steel plates was more effective than using glass fiber laminates, achieving gains of 15–17% and confirming the superiority of steel reinforcement. Overall, the combined use of bacteria and fibers demonstrated substantial improvements, with compressive strength enhancements reaching up to 55%, underscoring the promise of hybrid microbial–fibrous systems for high-performance, durable concrete.
- The selected mix proportions ensured adequate workability in all mixes despite fiber addition. The hardened properties showed that steel fibers enhanced compressive and flexural strength, while bacterial inclusion contributed to micro-crack healing in mixes BMS, BMP, W1S, and W1P.
- Generally, the combination of bacteria with fibers significantly boosts concrete performance, with compressive, tensile, and flexural strengths showing remarkable gains. The synergy of microbial self-healing and fiber reinforcement achieved improvements up to 55%. Steel plate reinforcing further enhanced slab behavior, offering a durable, practical, and sustainable solution for construction.

7. Recommendations

- Extend numerical simulations to include GFRP and full external strengthening schemes.
- Examine long-term durability and self-healing performance of bacterial-fiber concrete under realistic environmental conditions.
- Study the combined effects of conventional reinforcement, fibers, and bacteria on RC slab performance.
- Evaluate the influence of different bacterial species, dosages, and fiber types on mechanical properties and crack-healing behavior.

Acknowledgements

None declared.

Funding

The authors received no financial support for the research, authorship, and/or publication of this manuscript.

Conflict of Interest

The authors declare no potential conflicts of interest with respect to the research, authorship, and/or publication of this manuscript.

Data Availability

The datasets generated and/or analyzed during the current study are not publicly available but are available from the corresponding author upon reasonable request.

AI Assistance

No AI-based tools were used in the preparation of this manuscript.

Author Contributions

All authors made substantial contributions to the conception and design of the study, acquisition of data, analysis and interpretation of data; drafted or critically revised the manuscript for important intellectual content; and approved the final version to be published.

REFERENCES

ACI 211.1 (2009). Standard practice for selecting proportions for normal, heavyweight, and mass concrete. American Concrete Institute, Farmington Hills, MI, USA.

Ahmed SO, Nasser AAA, Abbas RN, Kamal MM, Zahran MA, Sorour NM (2021). Production of bioconcrete with improved durability properties using alkaliphilic Egyptian bacteria. *3 Biotech*, 11(5), 231.

ASTM C1609/C1609M (2019). Standard test method for flexural performance of fiber-reinforced concrete (using beam with third-point loading). ASTM International, West Conshohocken, PA, USA.

ASTM E399 (2020). Standard test method for linear-elastic plane-strain fracture toughness of metallic materials. ASTM International, West Conshohocken, PA, USA.

Bakr MA, Hussain A, Singh PK, Singh BK, Prajakti (2024). Effects of bacterial consortium-enhanced recycled coarse aggregates on self-healing concrete immobilized with Bacillus megaterium MTCC 1684 and Bacillus subtilis NCIM 2193. *Structural Concrete*, 25(3), 1840–1864.

de Brito J, Kurda R (2021). The past and future of sustainable concrete: A critical review and new strategies on cement-based materials. *Journal of Cleaner Production*, 281, 123558.

ES 1072/2008 (2008). Egyptian standard specification for Portland cement. Egyptian Organization for Standardization and Quality, Cairo, Egypt.

ES 1658/2018 (2018). Egyptian standard specification for aggregates used in concrete. Egyptian Organization for Standardization and Quality, Cairo, Egypt.

E.S.S. 4756-1/2022 (2022). Egyptian standard specification for fiber-reinforced concrete – Part 1: Requirements. Egyptian Organization for Standardization and Quality, Cairo, Egypt.

Ganesh S, Danish P, Jessie JA, Ganie MA, Raina CS (2020). Experimental study on self-healing concrete with the effect of Bacillus subtilis bacteria to improve the strength and sustainability of the concrete. *Journal of Green Engineering*, 10(4), 1909–1923.

Griño AA, Soriano HSP, Promentilla MAB, Ongpeng JMC (2023). Exploring the potential of polypropylene fibers and bacterial co-culture in repairing and strengthening geopolymer-based construction materials. *Buildings*, 13(10), 2668.

Han S, Jang I, Choi EK, Park W, Yi C, Chung N (2020). Bacterial self-healing performance of coated expanded clay in concrete. *Journal of Environmental Engineering*, 146(7), 04020072.

Helal Z, Salim H, Ahmad SSE, Elemam H, Mohamed AIH, Elmahdy MAR (2024). Sustainable bacteria-based self-healing steel fiber reinforced concrete. *Case Studies in Construction Materials*, 20, e03389.

Hosseinzadeh H, Salehi AM, Mehraein M, Asadollahfardi G (2023). The effects of steel, polypropylene, and high-performance macro polypropylene fibers on mechanical properties and durability of high-strength concrete. *Construction and Building Materials*, 386, 131589.

Igbokwe E, Ibekwe S, Mensah P, Agu O, Abedin R (2022). Efficacy of cellulose fiber as a bacterial carrier for self-healing concrete and 3D polymer microstructure. *Proceedings for the American Society for Composites-Thirty Seventh Technical Conference*, Tucson, AZ.

Islam SU, Waseem SA (2023). Strength retrieval and microstructural characterization of Bacillus subtilis and Bacillus megaterium incorporated into plain and reinforced concrete. *Construction and Building Materials*, 404, 133331.

İsar A, Sürmelioğlu S, Andiç-Çakir Ö, Hameş EE (2023). Improvement of microstructure of cementitious composites by microbially-induced calcite precipitation. *World Journal of Microbiology and Biotechnology*, 39(3), 76.

Ji HM, Liang SM, Li XW, Chen DL (2020). Kinking and cracking behavior in nacre under stepwise compressive loading. *Materials Science and Engineering: C*, 108, 110364.

Mohammed H, Ortoneda-Pedrola M, Nakouti I, Bras A (2020). Experimental characterisation of non-encapsulated bio-based concrete with self-healing capacity. *Construction and Building Materials*, 256, 119411.

Mostofinejad D, Karimi N, Tayebani B (2022). Effect of bacterial spore in surface-treated fiber-reinforced concrete. *ACI Materials Journal*, 119, 1–12.

Mutitu DK (2019). Influence of Lysinibacillus sphaericus on compressive strength and water sorptivity in microbial cement mortar. *M.Sc. thesis*, Jomo Kenyatta University, Kenya.

Nasser AA, Esmail RF, Abbas RY, Sorour NM (2022). Effect of Bacillus megaterium bacteria and different calcium sources on strength and permeation properties of concrete. *Engineering Research Journal*, 45(3), 401–412.

Nasser AA, Sorour NM, Saafan MA, Abbas RN (2022). Microbially-induced calcite precipitation (MICP): A biotechnological approach to enhance the durability of concrete using Bacillus pasteurii and Bacillus sphaericus. *Heliyon*, 8(7), e09948.

Nimafar M, Hosseini SJ, Akhlaghi A, Samali B, Soltaninia S (2023). Effect of bacterial carbonate precipitation on the durability of concrete specimens exposed to high temperatures. *Journal of Materials in Civil Engineering*, 35(1), 04022394.

Puranik SA, Jain S, Sritam G, Sandbhor S (2019). Bacterial concrete—a sustainable solution for concrete maintenance. *International Journal of Innovative Technology and Exploring Engineering*, 8, 227–232.

Rauf M, Khaliq W, Khushnood RA, Ahmed I (2020). Comparative performance of different bacteria immobilized in natural fibers for self-healing in concrete. *Construction and Building Materials*, 259, 119788.

Rossi E, Vermeer CM, Mors R, Kleerebezem R, Copuroglu O, Jonkers HM (2021). On the applicability of a precursor derived from organic waste streams for bacteria-based self-healing concrete. *Frontiers in Built Environment*, 7, 632921.

Roy R, Rossi E, Silfwerbrand J, Jonkers H (2021). Self-healing capacity of mortars with added-in bio-plastic bacteria-based agents: Characterization and quantification through micro-scale techniques. *Construction and Building Materials*, 297, 123793.

Ryparova P, Prošek Z, Schreiberova H, Bílỳ P, Tesarek P (2021). The role of bacterially induced calcite precipitation in self-healing of cement paste. *Journal of Building Engineering*, 39, 102299.

Sadeghpour M, Baradaran M (2023). Effect of bacteria on the self-healing ability of fly ash concrete. *Construction and Building Materials*, 364, 129956.

Saridhe SP, Selvaraj T (2021). Microbial precipitation of calcium carbonate in cementitious materials–A critical review. *Materials Today: Proceedings*, 43, 1232–1240.

Singh OP, Kulhar KS, Upadhyai RP (2023). The comparison of the experimental investigations of strength characteristics of conventional and bacterial concrete. *Materials Today: Proceedings*.

Su Y, Qian C, Rui Y, Feng J (2021). Exploring the coupled mechanism of fibers and bacteria on self-healing concrete from bacterial extracellular polymeric substances (EPS). *Cement and Concrete Composites*, 120, 103896.

Su Y, Zheng T, Qian C (2021). Application potential of Bacillus megaterium encapsulated by low alkaline sulphoaluminate cement in self-healing concrete. *Construction and Building Materials*, 273, 121740.

Tang Y, Xu J (2021). Application of microbial precipitation in self-healing concrete: A review on the protection strategies for bacteria. *Construction and Building Materials*, 306, 124950.

Wachira JM, Thiong'o JK, Marangu JM, Murithi LG (2019). Physicochemical performance of Portland-rice husk ash-calcined clay-dried acetylene lime sludge cement in sulphate and chloride media. *Advances in Materials Science and Engineering*, 2019, 5618743.

Wang Y, Jiang N, Saracho AC, Doygun O, Du Y, Han X (2023). Compressibility characteristics of bio-cemented calcareous sand treated through the bio-stimulation approach. *Journal of Rock Mechanics and Geotechnical Engineering*, 15(2), 510–522.

Xie F, Tian W, Li S, Diez P, Zlotnik S, Gonzalez AG (2025). Experimental study on the structural performance of glass-fiber-reinforced concrete slabs reinforced with glass-fiber-reinforced polymer (GFRP) bars: A sustainable alternative to steel in challenging environments. *Polymers*, 17(8), 1068.

Xu J, Tang Y, Wang X (2020). A correlation study on optimum conditions of microbial precipitation and prerequisites for self-healing concrete. *Process Biochemistry*, 94, 266–272.

Zahran MA, Attia M, Nasser AA (2014). Self-healing of cracked concrete with bacterial approach. *ERJ Engineering Research Journal*, 37(2), 255-264.

Challenge Journal of CONCRETE RESEARCH LETTERS

Research Article

Using the efflorescence mechanism of portland cement to obtain a shiny calcium carbonate surface

Juan Carlos Hernandez Palacios [a], Imelda Olivas Armendariz [a], Juan Francisco Hernandez Paz [a], Pedro Perez Rodriguez [a], Jose Luis Sandoval Granados [b], Hortensia Reyes Blas [a], Lorena Rivera Rios [a], Claudia Alejandra Rodriguez Gonzalez [a,*]

[a] *Department of Physics and Mathematics, Institute of Engineering and Technology, Universidad Autónoma de Ciudad Juarez, 32310 Cd Juárez, Chih., Mexico*
[b] *Department of Architecture, Institute of Arquitecture, Design and Arts, Universidad Autónoma de Ciudad Juarez, 32310 Cd Juárez, Chih., Mexico*

ABSTRACT

This study presents a novel curing strategy to produce a smooth and shiny surface on Portland cement paste by controlling efflorescence. The proposed methodology consists of curing fresh cement paste in contact with a smooth, polystyrene mold, which modifies the boundary conditions at the cement–mold interface by limiting evaporation and promoting local moisture retention during early hydration. Although direct exposure to the atmosphere is restricted, carbon dioxide from the environment can still diffuse through the cement pore network and specimen edges. Under these conditions, calcium ion migration toward the interface is facilitated, leading to the controlled precipitation of a thin, calcium carbonate–rich surface layer. The surface and bulk evolution of the cement paste were investigated after 7, 14, and 28 days of curing using scanning electron microscopy (SEM), energy-dispersive X-ray spectroscopy (EDS), X-ray diffraction (XRD), Fourier transform infrared spectroscopy (FTIR), surface gloss measurements, and compressive strength testing. The analyses reveal the formation of a uniform near-surface region enriched in calcium-containing phases, while the bulk phase assemblage remains dominated by typical hydration products. Quantitative gloss measurements show an increase in surface reflectivity with curing time, reaching approximately 57 ± 1.3 gloss units after 28 days. Compressive strength results indicate that the formation of the shiny surface layer does not adversely affect the mechanical performance of the material. Overall, the results indicate that under the proposed curing conditions, controlled efflorescence could be harnessed as a surface engineering approach to obtain visually uniform and chemically stable surfaces without the use of additives or post-processing treatments.

ARTICLE INFO

Article history:
Received – September 4, 2025
Revision requested – October 1, 2025
Revision received – January 1, 2026
Accepted – January 9, 2026

Keywords:
Efflorescence
Portland cement
Controlled carbonation
Calcium carbonate surface layer

Citation: Hernandez Palacios JC, Olivas Armendariz I, Hernandez Paz JF, Perez Rodriguez P, Sandoval Granados JL, Reyes Blas H, Rivera Rios L, Rodriguez Gonzalez CA (2026). Using the efflorescence mechanism of portland cement to obtain a shiny calcium carbonate surface. *Challenge Journal of Concrete Research Letters*, 17(1), 30–40.

1. Introduction

Cement, primarily in the form of Portland cement, remains the most widely used hydraulic binder in modern construction, with global production exceeding 4.2 billion tons annually (Scrivener et al. 2018). Its widespread use is due to its favorable combination of mechanical strength, cost-effectiveness, and versatility across structural and architectural applications. As the key component in concrete, mortars, grouts, and surface finishes, it plays a central role in infrastructure development worldwide. However, the aesthetic and surface

* *Corresponding author*. E-mail address: claudia.rodriguez@uacj.mx (C. A. Rodriguez Gonzalez)
ISSN: 2548-0928 / DOI: https://doi.org/10.20528/cjcrl.2026.01.003

durability of cement-based materials continues to present challenges, particularly in architectural contexts where surface quality and appearance are critical (Neville 2011).

One of the most common surface-related issues in cement-based materials is efflorescence, characterized by the formation of white crystalline deposits—primarily calcium carbonate—on the exposed surface. These deposits, while chemically benign, are perceived as defects due to their high visual contrast and irregular distribution, which compromise the intended aesthetic (Kosmatka et al. 2002; Brocken and Nijland 2004; Brick Industry Association 2006). Efflorescence can also indicate ongoing moisture transport, which may lead to concerns about durability or permeability, even when these concerns are not mechanically substantiated (Al-Jabari 2022).

Efflorescence is primarily driven by the migration of soluble salts, especially calcium hydroxide (portlandite), through capillary pores during early hydration or due to environmental moisture exposure. Once at the surface, these salts react with atmospheric CO_2, precipitating as calcium carbonate ($CaCO_3$) in a process often referred to as carbonation-induced efflorescence (Ramachandran 1996; Taylor 1997). In complex environmental or cement systems, other phases such as alkali sulfates, thenardite (Na_2SO_4), glaserite ($K_3Na(SO_4)_2$), syngenite ($K_2Ca(SO_4)_2{\cdot}H_2O$), and even ettringite may also appear (Ma and Qian 2018; Bai 2009). Efflorescence is generally categorized into two types: primary efflorescence, which occurs during initial hydration and curing, and secondary efflorescence, which emerges due to water ingress after curing, often through rain, condensation, or rising damp (Dahri 2022; Sutan and Sinin 2013).

Efforts to mitigate efflorescence have traditionally focused on reducing water-to-cement ratios, modifying mix design (e.g., with pozzolanic additions or blended cements), controlling curing conditions, or applying surface sealants to reduce permeability (Liang et al. 2022; Zhang et al. 2014, 2018). The use of admixtures such as sodium stearate, or hydrophobic agents has also been explored, though results vary depending on the system and exposure conditions (Xue et al. 2018; Chindaprasirt et al. 2022; Lothenbach et al. 2011). However, most of these methods seek to suppress the efflorescence mechanism rather than leverage it.

This study investigates an alternative curing approach in which efflorescence is deliberately controlled to promote the formation of a smooth, carbonate-rich surface layer. Instead of eliminating the migration of calcium salts, we control it to produce a smooth, shiny, and durable surface finish. By curing the cementitious material in contact with a smooth, non-porous polymeric mold under controlled humidity, we guide the migration and crystallization of calcium carbonate into a thin, homogeneous surface layer. The result is a naturally shiny and aesthetically appealing finish that exploits the same physicochemical mechanisms responsible for undesired efflorescence, transforming them into a design opportunity.

This methodology, currently under patent application (Mx/a/2016/002861), enables the controlled formation of functional calcium carbonate coatings during early hydration. These coatings exhibit uniform shine, enhanced surface texture, and potentially improved durability against weathering or abrasion. Moreover, the process is compatible with conventional cementitious materials and does not require post-processing treatments or additives. The aim of this work is to investigate the microstructural and surface implications of this approach and evaluate its potential for sustainable, low-cost, and architecturally expressive cement-based surfaces.

2. Experimental Procedure and Materials

2.1. Materials

The materials used for the procedure were sourced locally. The Portland cement used was a standard Type I cement commonly distributed in the region. The water used in the experiments was supplied by the city's water and sanitation company.

2.2. Experimental procedure

Samples were prepared using Type I Portland cement and water at a water-to-cement ratio (w/c) of 0.50 by mass. The cement powder was sifted using a sieve to ensure uniform particle size and then mixed with water. The mixture was stirred continuously until a homogeneous composition was achieved. The prepared mixture was poured into polystyrene containers with dimensions of 7 cm in height, 8 cm in width, and 18.5 cm in length. After casting, the specimens remained in the polystyrene molds and were cured under uncontrolled ambient indoor conditions typical of the laboratory environment in Ciudad Juárez (Chihuahua, Mexico). During the curing period, the indoor temperature averaged 23 ± 2 °C, with a relative humidity of 25–35 %, consistent with the local semi-arid climate. The indoor CO_2 concentration was not actively regulated but generally remained within 420–650 ppm, which corresponds to typical atmospheric levels for indoor environments in the region. No external load or confinement was applied; the only contact pressure exerted on the samples was due to their own self-weight against the smooth polystyrene surface. The specimens were cured for 7, 14, and 28 days under these conditions.

Surface gloss was quantitatively evaluated using a portable glossmeter Landtek GM60 (measurement geometry: 60°, in accordance with ISO 2813). Gloss measurements were performed directly on the cement surfaces after 7, 14, and 28 days of curing. For each curing age, measurements were taken at three different locations on the sample surface, and the average value was reported in gloss units (GU), together with the corresponding standard deviation. For the chemical stability test, shiny-surface specimens cured for 28 days were immersed in aqueous solutions with pH 4, 7, and 11 for 5 minutes at room temperature. After immersion, the samples were rinsed with deionized water to remove residual solution and then allowed to air-dry for 6 hours under laboratory conditions until the surface was completely dry. Surface gloss was measured before immersion and after drying using the same measurement con-

ditions described above. The variation in gloss values was used as an indicator of the short-term chemical stability of the surface layer.

The morphology and elemental chemical composition of the samples were analyzed using scanning electron microscopy (SEM, Hitachi model SU5000) and Energy Dispersive X-Ray Spectroscopy (EDS, Bruker), with an acceleration voltage of 15 kV. Phase identification and structural analysis were performed by X-ray diffraction (XRD) using a PANalytical X'Pert Pro diffractometer with Cu Kα radiation (λ = 0.1542 nm). Measurements were carried out on intact cement paste specimens, with the exposed surface facing the incident X-ray beam. As a result, the diffraction patterns mainly reflect the bulk phase composition of the material, while allowing qualitative comparison between samples. Functional groups present in the samples were identified using Fourier Transform Infrared Spectroscopy (FT-IR, Nicolet 6700) in the range of 500-3000 cm^{-1}. FTIR and XRD measurements were performed on replicate specimens for each curing age and condition, showing consistent spectral features; therefore, representative spectra are reported.

3. Results and Discussion

Fig. 1 presents the surface appearance of Portland cement samples cured for 7, 14, and 28 days, together with the corresponding quantitative gloss measurements. After 28 days, the surface exhibits a distinctly smooth and reflective appearance. This visual evolution is corroborated by the gloss measurements, which show a systematic increase in gloss units with curing time. The average surface gloss increased progressively from 22 ± 3 GU at 7 days to 35 ± 1.7 GU at 14 days, reaching 57 ± 1.3 GU at 28 days. The progressive reduction in standard deviation suggests enhanced surface uniformity and a more homogeneous development of the shiny surface layer over time.

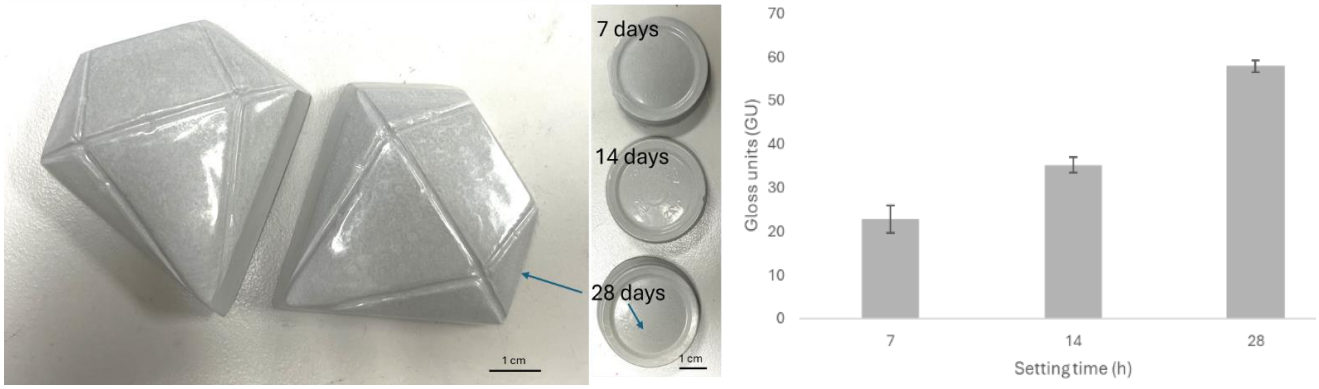

Fig. 1. Progressive development of shiny surfaces in Portland cement samples over 7, 14, and 28 days of curing.

Figs. 2–4 present a comparison between samples set using a conventional process and those treated according to the methodology proposed in this study, utilizing a surface in contact with polystyrene, after 7, 14, and 28 days of curing. From day 7 onward, a significant difference is observed in both the roughness and morphology of the surface, as well as in the phases present, evidenced by the varying gray tones in the backscattered electron images. The conventionally cured sample exhibits a more irregular surface morphology, with predominantly spherical particles and some polyhedral features. This is consistent with the findings reported previously for Portland cement, where the morphology of cement particles is typically characterized by spherical and irregular shapes due to the grinding and clinker formation processes (Taylor 1997; Bogue 1955). In contrast, the surface set using the proposed methodology appears visually smoother and is composed of two main phases: one with an acicular shape (lighter gray) and the other with spherical particles.

After 14 days, the roughness on both surfaces has decreased. The surface set conventionally exhibits microcracks or irregularities and is primarily composed of spherical particles with the presence of some needle-like structures. This aligns with findings reported in the literature, where the morphology of conventional Portland cement over time typically shows a decrease in surface roughness and the formation of microcracks as hydration progresses (Taylor 1997; Bogue 1955; Lura et al. 2003). In contrast, the surface set using the procedure proposed in this study still shows two distinct phases: spherical particles and acicular ones. However, the acicular phase appears to have undergone some growth, and the needle-like structures are now less noticeable.

After 28 days of conventional curing, at low magnifications, the surface appears to have minimal roughness. At higher magnifications, larger particles are observed, covered by small spherical particles, with the presence of some needle-like structures. This aligns with previous studies, where the morphology of Portland cement at later stages of hydration typically shows the development of larger particles covered by finer spherical ones, along with the formation of needle-like structures such as ettringite (Taylor 1997). In contrast, for the curing process proposed in this study, the surface roughness has decreased even at higher magnifications. Both phases, spherical particles and acicular structures, are still present, but the needle-like structures have grown and now cover almost the entire surface. This is consistent with the evolution of the microstructure described in the literature, where needle-like crystals tend to grow and eventually dominate the surface as hydration progresses (Bogue 1955; Lura et al. 2003).

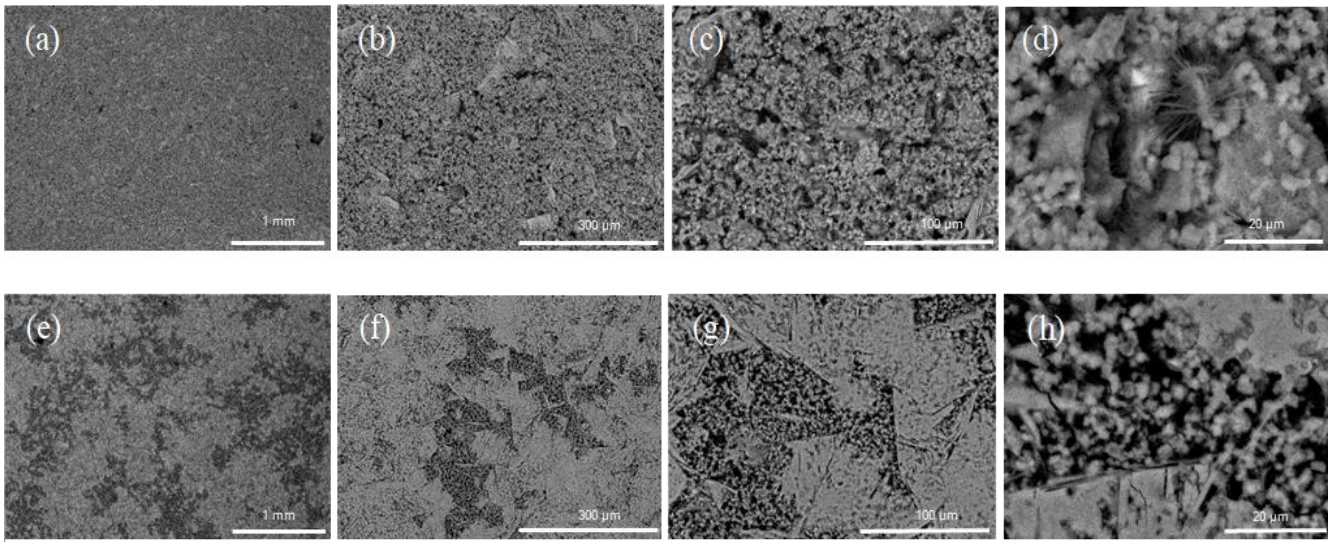

Fig. 2. SEM–BSE surface morphology after 7 days of curing for conventional (a–d) and shiny (e–h) cement paste samples. Imaging conditions: 20 kV, WD 19–23 mm, 30 Pa.

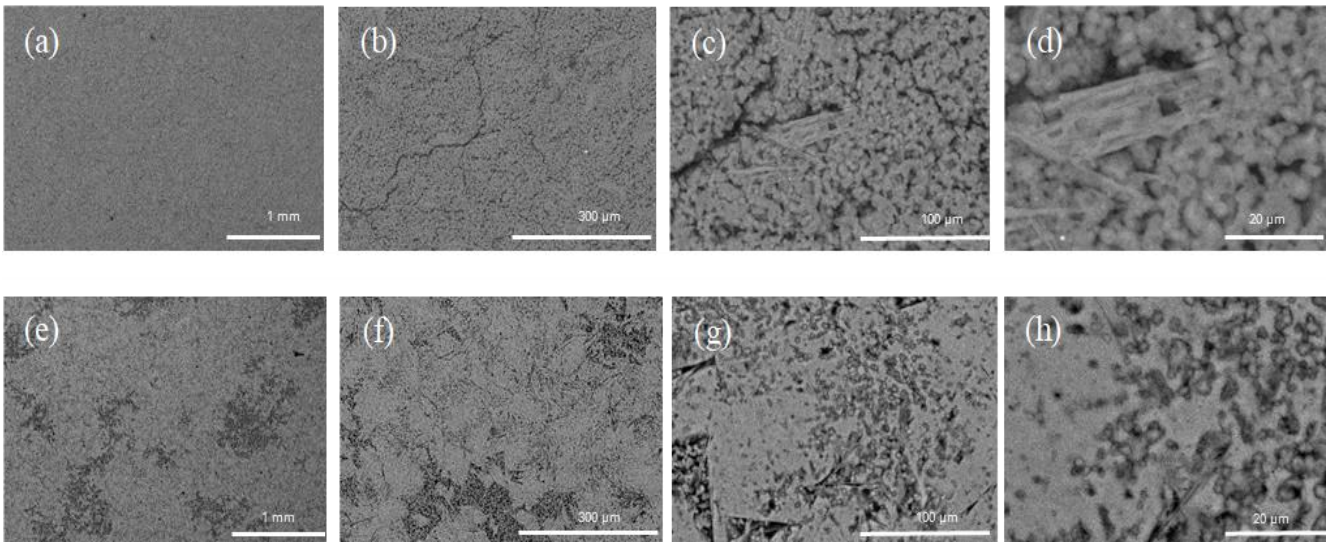

Fig. 3. SEM–BSE surface morphology after 14 days of curing for conventional (a–d) and shiny (e–h) cement paste samples. Imaging conditions: 20 kV, WD 19–23 mm, 30 Pa.

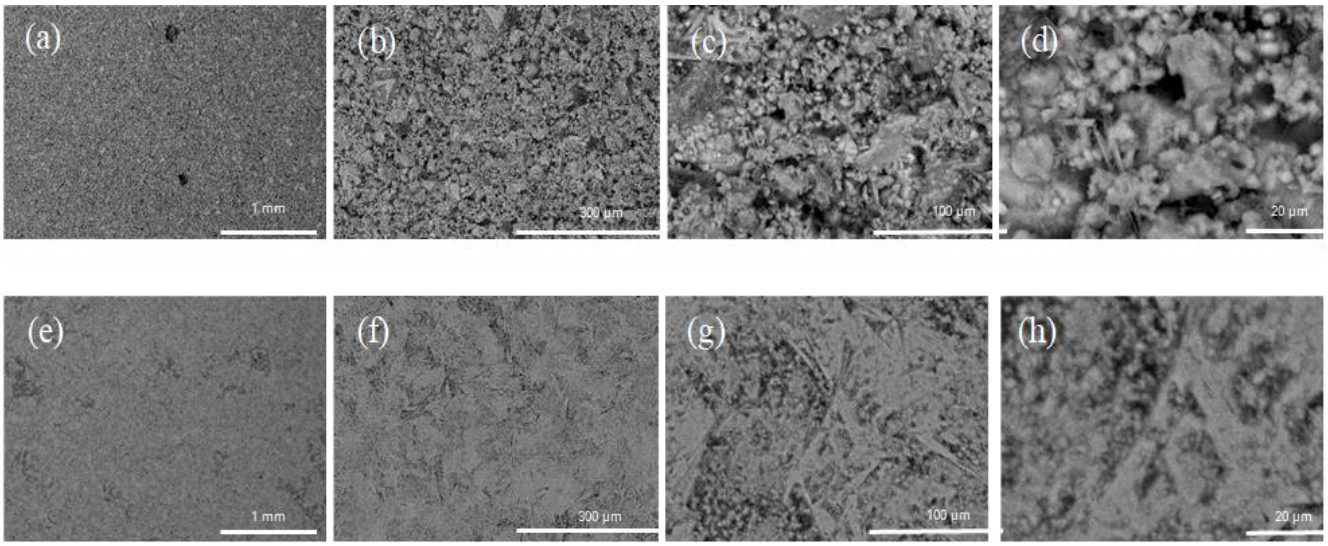

Fig. 4. SEM–BSE surface morphology after 28 days of curing for conventional (a–d) and shiny (e–h) cement paste samples. Imaging conditions: 20 kV, WD 19–23 mm, 30 Pa.

Fig. 5 presents the XRD patterns of Portland cement paste specimens cured for 7, 14, and 28 days, together with a conventional reference sample. All diffractograms are dominated by a broad amorphous background attributed to calcium silicate hydrate (C–S–H), along with crystalline reflections corresponding to portlandite ($Ca(OH)_2$) and calcium carbonate ($CaCO_3$) (Taylor, 1997). Weak and partially overlapped reflections associated with residual clinker phases, mainly tricalcium silicate (C_3S) and dicalcium silicate (C_2S), are also detected.

The conventional sample exhibits more clearly defined reflections associated with residual clinker phases compared to the specimens cured against the smooth polymeric surface. Given the limited surface sensitivity of conventional powder XRD, these differences should be interpreted with caution and primarily reflect variations in the bulk phase contribution. With increasing curing time, the relative intensity of $CaCO_3$ reflections increases for all samples, while the overall phase assemblage remains unchanged (Lura et al. 2003).

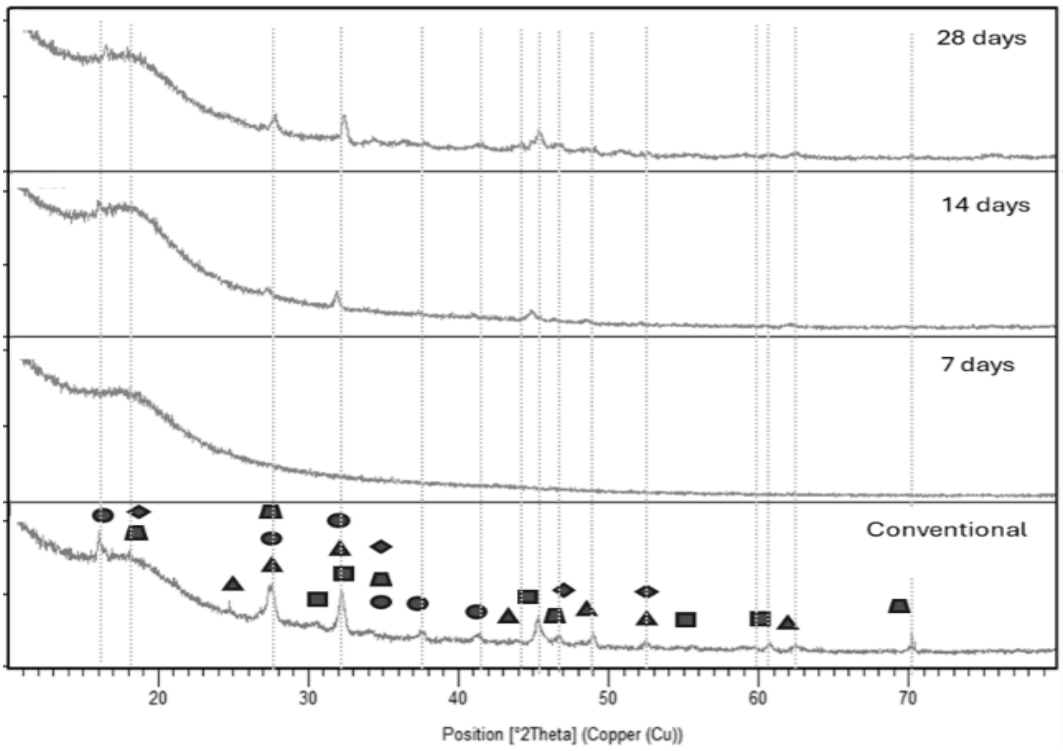

	Phase	Chemical formula	PDF reference	Main 2θ (°)	d-spacing (Å)	Conventional	7 days	14 days	28 days
▲	**Portlandite**	$Ca(OH)_2$	00-044-1481	~18.0	4.90	✓	✓	✓	✓
				~34.1	2.63	✓	✓	✓	✓
				~47.1	1.93	~	~	~	~
▲	**Calcium carbonate ($CaCO_3$)**	$CaCO_3$	00-033-0268	~29.4	3.03	✓	✓	✓	✓
				~39.4	2.28	~	~	✓	✓
				~43.1	2.10	~	~	~	✓
◆	**Alite**	Ca_3SiO_5	00-031-0301	~29.3	3.05	~	~	~	~
				~32.1	2.78	~	~	~	~
				~51.7	1.77	—	—	—	~
■	**Belite**	Ca_2SiO_4	01-087-1260	~32.3	2.77	~	~	~	~
				~41.1	2.19	—	—	~	~
				~51.5	1.77	—	—	—	~
●	**Ettringite (minor)**	$Ca_6Al_2(SO_4)_3(OH)_{12}\cdot 26H_2O$	00-041-1451	~15.8	5.60	~	~	~	~
				~22.9	3.88	—	—	—	—
				~31.1	2.87	—	—	~	~

Notation: ✓ = clearly observed, ~ = weak/overlapped, — = not resolved

Fig. 5. XRD patterns of Portland cement paste under modified curing conditions after 7, 14, and 28 days.

The FTIR spectra (Fig. 6) of both conventional and shiny samples consistently display the main hydration and carbonation bands characteristic of Portland cement systems. In all cases, the sharp O–H stretching vibration of portlandite is observed at 3643 cm^{-1}, together with a broad O–H band above 3000 cm^{-1} and the H_2O bending mode around 1650 cm^{-1}. The Si–O stretching of C–S–H is identified near 970–990 cm^{-1}, while sulfate vibrations appear in the region of 1110–1140 cm^{-1}. Carbonate formation is indicated by the bands at 1450 cm^{-1} (ν_3, asymmetric stretching), 1070–1090 cm^{-1} (ν_1, symmetric stretching), and 874–878 cm^{-1} (ν_2, out-of-plane bending) (Ylmen and Jäglid 2013; Chakrabarty and Mahapatra 1999; Jennings 2000). These features are present in both curing conditions and at all curing ages (7, 14, and 28 days), with variations in relative intensity and definition that reflect progressive hydration and carbonation processes. In addition, an FTIR spectrum of the mold material was recorded to document the polymer used for sample casting (Fig. 7). The spectrum shows the characteristic absorption bands of polystyrene, confirming the nature of the mold material employed in this study.

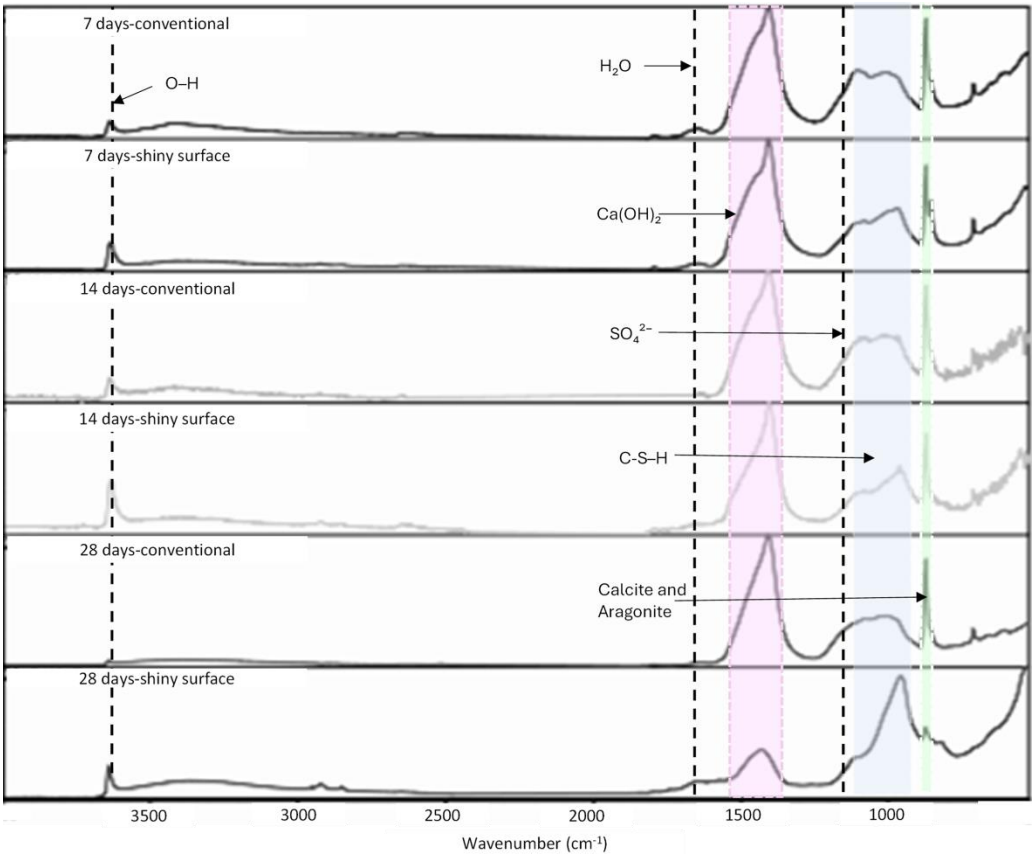

Fig. 6. FTIR analysis of the shiny surface and the Portland cement samples.

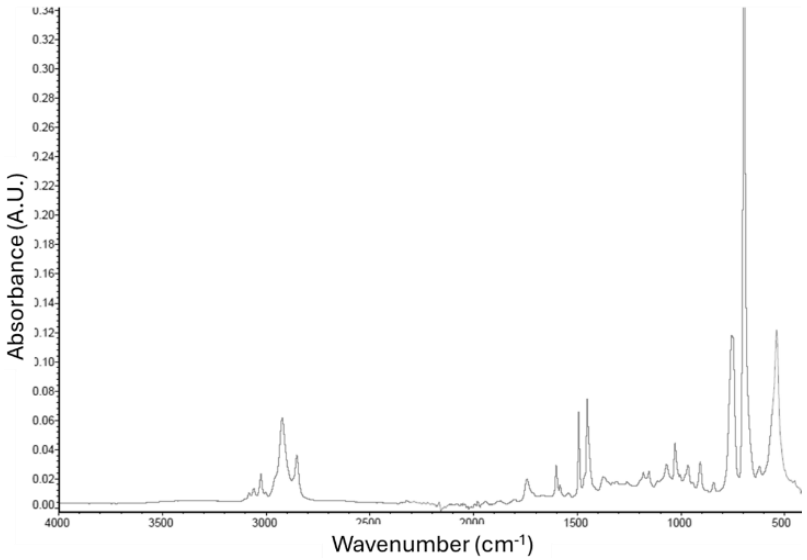

Wavenumber (cm^{-1})	Functional group / vibration	Assignment
3000–3100	Aromatic C–H stretching	Vibrations associated with the benzene ring of polystyrene
2924, 2846	Aliphatic C–H stretching (–CH_2–)	Asymmetric and symmetric stretching of methylene groups in the polymer backbone
1600, 1490, 1447	Aromatic C=C ring stretching	Characteristic phenyl ring vibrations of polystyrene
1000–1030	Aromatic ring deformation / C–H in-plane bending	Phenyl ring deformation modes
750, 700	Aromatic C–H out-of-plane bending	Diagnostic bands of mono-substituted benzene rings (pendant phenyl groups)

Fig. 7. FTIR spectrum of the polystyrene mold used for casting the Portland cement samples.

Fig. 8 presents cross-sectional SEM images and corresponding EDS spectra of Portland cement samples cured using the proposed methodology, which results in a visibly shiny surface layer. The SEM micrographs reveal a compact and dense outer region, particularly within the top ~50 μm of the surface, where the structure appears homogeneously packed. This dense morphology is attributed to minimized evaporation and restricted ion migration, induced using a smooth, non-porous polymeric mold during the early stages of hydration (Khayat 1999).

Within the microstructure, hydration products such as calcium silicate hydrate (C–S–H) and portlandite are clearly observed. The coexistence of fibrous, amorphous, and acicular phases suggests a well-developed and active hydration process, with no significant signs of microcracking, shrinkage, or surface deterioration. These features indicate that the curing method not only preserves structural integrity but may also promote surface densification, consistent with observations in high-performance and self-consolidating concretes where controlled curing conditions influence near-surface compactness.

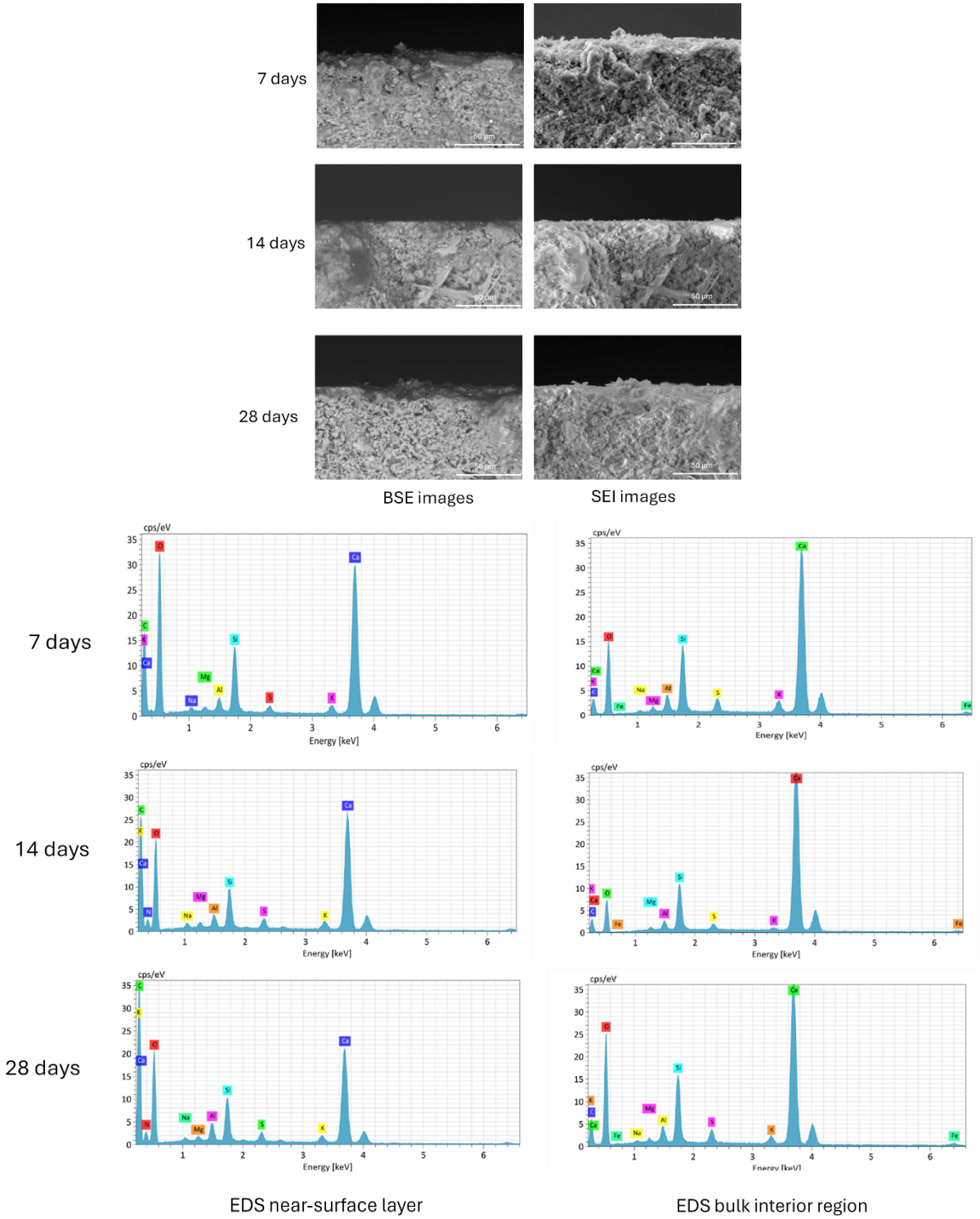

Fig. 8. Cross-sectional SEM images and corresponding EDS analyses of Portland cement paste cured using the proposed methodology after (a) 7, (b) 14, and (c) 28 days. Imaging conditions: 20 kV, working distance 11–14.2 mm, 30 Pa.

EDS elemental mapping (Fig. 9) confirms a marked increase and surface-level enrichment of calcium, particularly in specimens cured against smooth polymeric molds. This calcium-rich layer supports the formation of a dense, carbonate-containing coating, which is consistent with the enhanced reflectivity and "shiny" appearance observed macroscopically. This correlates with FTIR results, where stronger absorption bands for CO_3^{2-} groups are observed. While early stage XRD data revealed low surface crystallinity, the FTIR and SEM/EDS analyses demonstrate that carbonate formation is already underway at both the microstructural and molecular levels, though initially in amorphous or nano-crystalline form. The observed surface densification and spatial continuity in SEM images support the interpretation that smooth-surface curing promotes a controlled and delayed crystallization, which preserves surface integrity and contributes to long-term uniformity. In contrast, the conventionally cured control sample shows a less uniform calcium distribution and a more porous, irregular surface structure. This finding is consistent with the sharper diffraction peaks and earlier crystallization observed via XRD. The microstructural differences reinforce that the proposed curing strategy not only modulates hydration kinetics and carbonation pathways, but also improves aesthetic, protective, and potentially functional properties of the cement surface by forming a shiny, compact mineral layer.

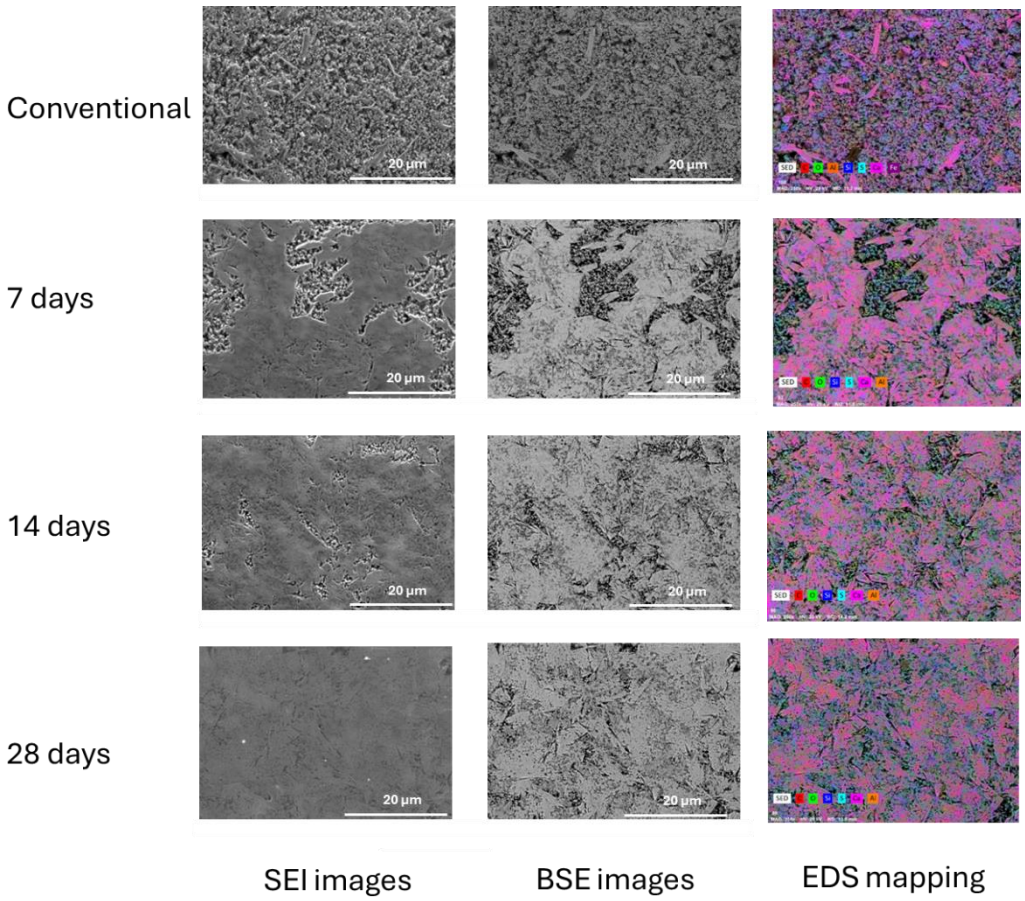

Fig. 9. SEM images and EDS elemental maps comparing a conventional Portland cement sample cured for 28 days with samples prepared using the proposed methodology after 7, 14, and 28 days of curing. Imaging conditions: 20 kV, working distance 10.8–14.2 mm, 30 Pa.

The formation of the shiny surface can be attributed to modified curing boundary conditions imposed by the smooth polymeric mold, which reduce surface evaporation and promote higher local moisture retention. Although direct exposure to the atmosphere is limited, CO_2 can still diffuse through the cement pore network and from specimen edges, enabling localized carbonation. These conditions are consistent with enhanced migration and accumulation of calcium-rich species near the surface, leading to the formation of a thin, dense carbonate-containing layer. This proposed mechanism (Fig. 10) is supported by SEM–EDS evidence of near-surface Ca enrichment, FTIR carbonate bands, and increased surface gloss with curing time. Due to the bulk sensitivity of conventional XRD, these effects are interpreted as near-surface phenomena rather than bulk phase transformations.

Table 1 summarizes the maximum compressive strength obtained for the analyzed samples. At 7 and 14 days, specimens with a shiny surface exhibited slightly higher compressive strength values than the conventional samples, with increases of approximately 0.9 % and 1.3 %, respectively. However, these differences fall within the range of experimental variability typically reported for compressive strength tests on Portland cement pastes and mortars (Mindess et al. 2003; Neville

2011). At 28 days, both sample types reached very similar maximum compressive strength values, indicating that the surface condition does not exert a significant influence on long-term mechanical performance. Overall, these results suggest that the formation of the shiny layer induced by controlled efflorescence is confined to the near-surface region and does not adversely affect the bulk mechanical response of the material.

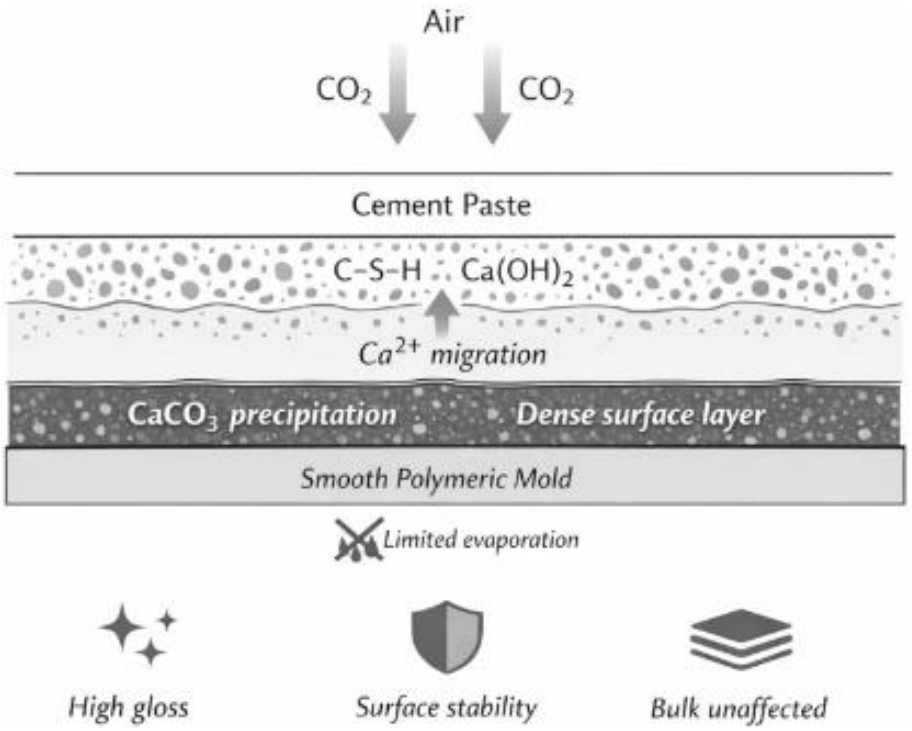

Fig. 10. Schematic illustration of the proposed mechanism for the formation of the shiny surface on Portland cement paste cured against a smooth polymeric mold (AI-assisted).

Table 1. Maximum compressive strength of conventional and shiny samples at different curing ages.

Sample / Curing age	7 days (conventional)	7 days (shiny)	14 days (conventional)	14 days (shiny)	28 days (conventional)	28 days (shiny)
Maximum compressive strength (MPa)	70.4 ± 3.1	71.0 ± 2.8	79.9 ± 2.5	81.0 ± 2.2	89.3 ± 2.0	89.0 ± 1.9

Fig. 11 shows the variation in surface gloss (expressed in gloss units, GU) of the shiny surfaces of Portland cement samples cured for 28 days, measured before and immediately after exposure to aqueous solutions with pH 4, 7, and 11, which were used to evaluate the chemical resistance of the surface layer. The results indicate that the initial gloss value of the shiny surface (≈ 58 GU) remains essentially unchanged after contact with the different media, with only minor fluctuations of less than ±2 GU, which fall within the experimental error margin. This stability indicates that the shiny surface layer exhibits a high resistance to immediate chemical attack, with no evidence of dissolution, loss of reflectance, or visible surface degradation. The preservation of gloss under pH 4 conditions suggests adequate tolerance to acidic environments, while the absence of significant gloss reduction at pH 11 demonstrates stability in alkaline media, consistent with the basic nature of Portland cement and its carbonated surface layer. Overall, these results confirm that the shiny finish not only provides aesthetic stability but also functions as a chemically stable surface barrier under short-term exposure to different chemical environments, preserving its optical properties and visual integrity even under controlled aggressive conditions.

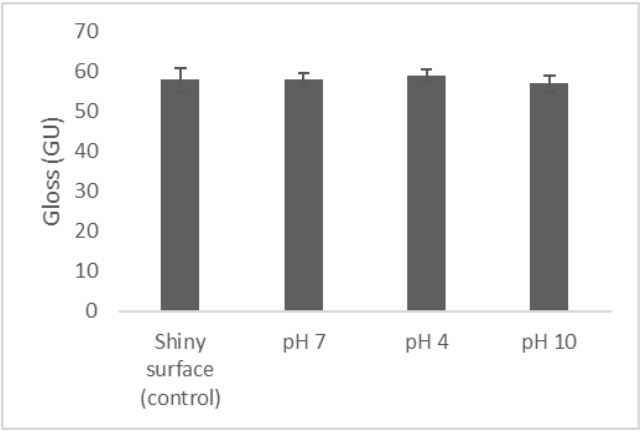

Fig. 11. Surface gloss values (GU) of shiny Portland cement samples cured for 28 days, measured before and after exposure to aqueous solutions with pH 4, 7, and 11.

4. Conclusions

This study presents an approach to reframe efflorescence in Portland cement as a controlled mechanism for achieving a functional and aesthetically appealing surface finish. By employing a smooth polymeric interface during curing, the migration of calcium-rich species and their subsequent reaction with atmospheric carbon dioxide were guided to promote the formation of a homogeneous, shiny surface layer rich in crystalline calcium carbonate. Microstructural and chemical analyses (SEM, EDS, XRD, and FTIR) confirmed the progressive development of this near-surface layer, while the bulk cement matrix retained the typical hydration products such as C–S–H, portlandite, and ettringite.

Importantly, quantitative surface gloss measurements and compressive strength testing demonstrate that the formation of the shiny layer is confined to the outer region of the material and does not adversely affect its mechanical performance. These findings indicate that the observed surface modification is not merely cosmetic, but rather reflects a localized mineralogical evolution driven by altered curing boundary conditions. Within the scope of this study, controlled efflorescence is shown to be a promising surface engineering approach that does not require additives or post-processing treatments. Beyond its potential architectural and prefabrication applications, this strategy provides new insight into the role of moisture transport, ion migration, and carbonation during early cement hydration and may inform future strategies for designing functional cement-based surfaces. From a sustainability perspective, the proposed methodology relies exclusively on controlled curing conditions, which may reduce material consumption, surface rework, and associated environmental impacts.

Acknowledgements

The authors declare that the methodology described in this study is subject to a patent application (Mx/a/2016/002861).

The biocompatibility and bioactivity of a similar material obtained under controlled conditions were reported in Vol. 7, No. 1 (2020) of Memorias del XLII Congreso Nacional de Ingeniería Biomédica, associated with the conference held on October 15-17, 2020.

This research has previously been presented at the XXX International Materials Research Congress (IMRC2022) held in Cancun, QR, Mexico, on August 14-19, 2022. Extended version of the research has been submitted to Challenge Journal of Concrete Research Letters and has been peer-reviewed prior to the publication.

Funding

The authors received no financial support for the research, authorship, and/or publication of this manuscript.

Conflict of Interest

The authors declare no potential conflicts of interest with respect to the research, authorship, and/or publication of this manuscript.

Data Availability

The datasets generated and/or analyzed during the current study are not publicly available but are available from the corresponding author upon reasonable request.

AI Assistance

During the preparation of this manuscript, ChatGPT-5 (OpenAI) was used exclusively for image creation. The authors take full responsibility for the content, interpretation, and conclusions of the published article.

Author Contributions

All authors made substantial contributions to the conception and design of the study, acquisition of data, analysis and interpretation of data; drafted or critically revised the manuscript for important intellectual content; and approved the final version to be published.

References

Al-Jabari M (2022). Concrete durability problems: physicochemical and transport mechanisms. In: *Integral Waterproofing of Concrete Structures*. Springer, Cham, Switzerland, 69–107.

Bai J (2009). Durability of sustainable concrete materials. In: Khatib JM, editor. Sustainability of Construction Materials. Woodhead Publishing, Cambridge, UK, 239–253.

Bogue RH (1955). The Chemistry of Portland Cement. Reinhold Publishing Corporation, New York, USA.

Brick Industry Association (2006). Efflorescence – Causes and prevention. Technical Note 23A. https://www.gobrick.com/docs/default-source/read-research-documents/technicalnotes/tn23a.pdf [accessed 01-09-2024].

Brocken HJP, Nijland TG (2004). White efflorescence on brick masonry and concrete masonry blocks, with special emphasis on sulfate efflorescence on concrete blocks. *Construction and Building Materials*, 18(5), 315–323.

Chakrabarty D, Mahapatra S (1999). Aragonite crystals with unconventional morphologies. *Journal of Materials Chemistry*, 9(11), 2953–2957.

Chindaprasirt P, Jitsangiam P, Rattanasak U (2022). Hydrophobicity and efflorescence of lightweight fly ash geopolymer incorporated with calcium stearate. *Journal of Cleaner Production*, 364, 132449.

Dahri AA (2022). Experimental study of effects of efflorescence control admixture in cement mortar. *Quaid-e-Awam University Research Journal of Engineering Science and Technology*, 20(2), 71–76.

Jennings HM (2000). A model for the microstructure of calcium silicate hydrate in cement paste. *Cement and Concrete Research*, 30(1), 101–116.

Khayat KH (1999). Workability, testing, and performance of self-consolidating concrete. *ACI Materials Journal*, 96(3), 346–353.

Kosmatka SH, Kerkhoff B, Panarese WC (2002). Design and Control of Concrete Mixtures. Portland Cement Association, Skokie, IL, USA.

Liang K, Cui K, Sabri MMS, Huang J (2022). Influence factors in the wide application of alkali-activated materials: A critical review about efflorescence. *Materials*, 15(18), 6436.

Lothenbach B, Scrivener K, Hooton RD (2011). Supplementary cementitious materials. *Cement and Concrete Research*, 41(12), 1244–1256.

Lura P, Jensen OM, Van Breugel K (2003). Autogenous shrinkage in high-performance cement paste: An evaluation of basic mechanisms. *Cement and Concrete Research*, 33(2), 223–232.

Ma Y, Qian J (2018). Influence of alkali sulfates in clinker on the hydration and hardening of Portland cement. *Construction and Building Materials*, 180, 351–363.

Mehta PK, Monteiro PJM (2014). Concrete: Microstructure, Properties, and Materials. 4th ed. McGraw-Hill Education, New York, USA.

Mindess S, Young JF, Darwin D (2003). *Concrete*. 2nd ed. Prentice Hall, Upper Saddle River, NJ, USA.

Neville AM (2011). Properties of Concrete. 5th ed. Pearson Education, London, UK.

Provis JL, van Deventer JSJ (2014). Alkali Activated Materials. Springer, Dordrecht, Netherlands.

Ramachandran VS (1996). Concrete Admixtures Handbook. 2nd ed. William Andrew Publishing, Norwich, NY, USA.

Scrivener KL, John VM, Gartner EM (2018). Eco-efficient cements: Potential, economically viable solutions for a low-CO_2, cement-

based materials industry. *Cement and Concrete Research*, 114, 2–26.

Sutan NM, Sinin H (2013). Efflorescence phenomenon on concrete structures. *Advanced Materials Research*, 626, 747–750.

Taylor HFW (1997). Cement Chemistry. 2nd ed. Thomas Telford, London, UK.

Xue X, Liu YL, Dai JG, Poon CS, Zhang WD, Zhang P (2018). Inhibiting efflorescence formation on fly ash–based geopolymer via silane surface modification. *Cement and Concrete Composites*, 94, 43–52.

Ylmen R, Jäglid U (2013). Carbonation of Portland cement studied by diffuse reflection Fourier transform infrared spectroscopy. *International Journal of Concrete Structures and Materials*, 7(2), 119–125.

Zhang Z, Provis JL, Reid A, Wang H (2014). Fly ash-based geopolymers: The relationship between composition, pore structure and efflorescence. *Cement and Concrete Research*, 64, 30–41.

Zhang Z, Provis JL, Ma X, Reid A, Wang H (2018). Efflorescence and subflorescence induced microstructural and mechanical evolution in fly ash-based geopolymers. *Cement and Concrete Composites*, 92, 165–177.

Challenge Journal of CONCRETE RESEARCH LETTERS

Research Article

Mechanical properties assessment of recycled brick aggregate concrete using demolition waste from century-old masonry buildings in Nepal

Bipul Niroula [a], Mahesh Raj Bhatt [a,*]

[a] *Department of Civil Engineering, Kathmandu University, 54200 Dhulikhel-Kavre, Nepal*

ABSTRACT

This study explores the potential of recycling bricks from dismantled old buildings into brick aggregates and utilizing them as coarse aggregates in recycled brick aggregate concrete. Nepal, being susceptible to seismic events, generates large amounts of construction debris, with bricks being a major portion of this, which is mainly disposed of through landfilling. Additionally, the increasing use of reinforced cement concrete construction has been significant, which poses a toll on natural aggregate resources, resulting in the depletion of finite resources. To address these issues, this study focuses on recycling bricks as coarse aggregates in concrete. An experimental approach was adopted to determine properties of bricks and concrete ingredients, including cement, sand, brick aggregates, and coarse aggregates. The mechanical and physical properties of concrete, that is, compressive, split-tensile, and flexural strengths were studied by replacing natural coarse aggregates with recycled crushed brick aggregates at different percentages (0%, 10%, 20%, 30%, and 100%), denoted as B0%, B10%, B20%, B30% and B100%, respectively. Meanwhile, ultrasonic pulse velocity was performed to determine the quality of recycled brick aggregate concrete. With respect to the control mix (B0%), percentage decrease in compressive strength, tensile strength, and flexural strength for B10% and B100% are 0.72% and 28.26%, 4.68% and 25.16%, and 2.95% and 7.58%, respectively. From the ultrasonic pulse velocity, all mixes except B100% had excellent quality as per Indian Standards. Results highlight that recycled brick aggregate seems suitable up to 30% replacement, considering the strength decrement in compressive and flexural strengths relative to the control mix.

ARTICLE INFO

Article history:
Received – November 12, 2025
Revision requested – December 9, 2025
Revision received – December 29, 2025
Accepted – January 10, 2026

Keywords:
Recycled brick aggregate concrete
Brick aggregates
Compressive strength
Flexural strength
Ultrasonic pulse velocity
Splitting tensile strength

Citation: Niroula B, Bhatt MR (2026). Mechanical properties assessment of recycled brick aggregate concrete using demolition waste from century-old masonry buildings in Nepal. *Challenge Journal of Concrete Research Letters*, 17(1), 41–56.

1. Introduction

The devastating Gorkha earthquake of 7.6 magnitude occurred on April 25, 2015, followed by a series of aftershocks, including a major 6.8 magnitude aftershock on May 12, 2015 (National Planning Commission 2015). The earthquake resulted in 3.23 million tons of potential debris in the core city area of the Kathmandu Valley, of which 1.07 million tons were cleared, 0.63 mil-lion tons were disposed of on riverbanks and in open spaces, and the remaining 0.44 million tons were salvaged for reuse, recycling, or disposal in isolated areas (Poudel et al. 2019). The debris was further classified, and brick/stone accounted for 74.66% of the total debris (Poudel et al. 2019). Currently, about 82.90% of total houses in Nepal are built with brick/stone bonded in mud or cement mortar for outer walls (Central Bureau of Statistics 2021).

* *Corresponding author*. E-mail address: mahesh.bhatt@ku.edu.np (M. R. Bhatt)
ISSN: 2548-0928 / DOI: https://doi.org/10.20528/cjcrl.2026.01.004

Globally, increasing concrete production affects water consumption, natural aggregate use, and cement production. In 2017, the production of natural aggregates was about 45 billion tons, and it was estimated to rise to 65 billion tons by 2025 (De Brito et al. 2019). The construction industry consumes around 40% of global resources, and one third of this is aggregates used in cement-based products (Pacheco-Torgal 2017). In Nepal, based on the number of households, reinforced concrete (RC) buildings have increased tremendously by 63.9% within a span of ten years from 2011 to 2021 (Central Bureau of Statistics 2021). This rapid growth has substantially increased the demand for natural aggregates, resulting in rampant extraction of natural aggregates, degradation of natural landscapes, depletion of finite natural resources, and escalating construction costs. Simultaneously, the disposal of building debris along riverbanks, open spaces, and landfilling has led to land pollution, degradation of the city landscape, a shortage of landfilling areas, and increased landfilling charges (Poudel et al. 2019).

Construction debris, such as concrete, bricks, and stones, is not organic waste and thus cannot decompose naturally (Gyawali 2022). The common practice is disposal by landfilling or dumping it in open spaces, which has a significant impact on the environment and human health. In the United States, recycling one ton of concrete, brick, and block costs approximately $21 per ton, while landfilling costs approximately $136 per ton (Lennon 2005). Recycling such construction debris as aggregates can help preserve finite natural resources, reduce waste, landfill sites, and improve economic efficiency. The first significant use of crushed brick aggregates in new concrete was for reconstruction during the Second World War, while its first documented use dates back to 1860 in Germany, for manufacturing concrete products (Adamson et al. 2015).

Several studies have investigated the mechanical performance of concrete utilizing recycled brick aggregates. De Brito et al. (2005) found a 22% and 45% decrement in compressive strength at 33% and 100% natural aggregate replacement, respectively. Debieb and Kenai (2008) reported a 20% to 35% reduction in strength when both coarse and fine aggregates were replaced with crushed brick aggregates. Cachim (2009) studied the mechanical properties of recycled brick aggregate concrete (RBAC) using bricks from two sources at two water-cement ratios and reported that higher-density brick aggregate yielded better compressive and tensile strengths. Aliabdo et al. (2014) reported increased compressive strength at 25% fine aggregate replacement, while all other mixes resulted in reduced compressive and tensile strength. Bhanbhro et al. (2014) reported a 37% decrease in compressive strength at 100% replacement. Hachemi et al. (2022) found that replacing 20% of both coarse and fine aggregates in concrete improved compressive strength and density. Gyawali (2022) reported an increase in compressive strength when oven-dried brick aggregates at 20% was replaced with natural coarse aggregates. Aboalella and Elmalky (2023) observed increased compressive, tensile, and flexural strength at 50% fine aggregate replacement with crushed brick and 50% coarse aggregate replacement with recycled concrete. Bhatta et al. (2024) found comparable compressive strength to the control mix at 20% replacement, highlighting its potential for construction applications. Basit et al. (2024) studied the structural performance of concrete using recycled concrete aggregates (RCA) and recycled brick aggregates (RBA). Modest decreases in compressive strength were observed when coarse aggregates were replaced, while RCAs showed better bond performance, and 50% natural aggregate replacement showed comparable performance to the control mix in flexure tests. Şamdan et al. (2024) studied the use of crushed brick clay as a replacement for coarse and medium aggregate in concrete at several replacement levels and found that such replacement decreased compressive strength and modulus of elasticity by up to 66%. Poudel et al. (2025) studied on enhancing the mechanical performance of recycled aggregate concrete using glass fibers with fly ash and found that 20% fly ash with 0.5% fibers provided balanced mechanical performance suitable for low-grade structural applications. Bajracharya et al. (2025) explored recycling old concrete as aggregates into concrete. They found that 50% replacement achieved strength comparable to conventional concrete, and also suggested that recycled concrete aggregates are socially, economically, and technically viable based on the sustainability index. Khadka et al. (2025) found a decrease in compressive strength of 34% to 39% when replacing natural coarse aggregates with brick aggregates at 100%, and also developed predictive relationships for concrete compressive strength based on rebound hammer tests.

Although numerous studies have investigated the use of recycled brick aggregates as coarse and fine aggregates in concrete, most have focused on recycled aggregates obtained from relatively recent brick waste. Limited attention has been given to aggregates produced from century-old bricks. Brick aggregates derived from such old bricks may exhibit distinct mechanical and physical characteristics due to prolonged environmental exposure, aging, and material degradation. This study experimentally evaluates the mechanical properties of recycled brick aggregate concrete (RBAC) produced using brick aggregates derived from a dismantled century-old masonry building as a partial to full replacement of natural coarse aggregates. The experimental program was conducted using M20 grade concrete, where M represents the mix and the following number 20 represents the specified compressive strength in MPa measured on a 150 mm cube. The M20 grade concrete was selected because it is widely used in Nepal for low-rise residential and other structures, and represents the minimum standard for reinforced concrete construction under Indian Standards.

The novelty of this research lies in the utilization of brick aggregates derived from century-old bricks exposed to long-term environmental exposure and aging, while comparing the properties of brick, brick aggregates, and recycled concrete with properties of modern and historic bricks from existing literature. Furthermore, the study compares aggregate-level quality indicators in relation to concrete performance and examines the feasibility of partial replacement of natural coarse aggregates under material constraints relevant to developing countries. This research is particularly relevant in the Nepalese context, where bricks have been historically used in structures such as load-bearing masonry buildings, arch bridges, and partition walls. With aging infrastructure, seismic vulnerability, and ongoing expan-

sion projects such as highway widening, large values of historic brick masonry are expected to be dismantled or demolished; however, systematic disposal or recycling practices remain largely absent.

2. Experimental Program

The experimental program comprised testing five concrete mixes with different percentages of recycled crushed brick aggregates, ranging from partial to full replacements of natural coarse aggregates. The replacement levels considered were 0%, 10%, 20%, 30%, and 100%, designated as B0% (control mix), B10%, B20%, B30%, and B100%, respectively. A total of 55 specimens were cast to evaluate compressive strength, splitting tensile strength, and flexural strength tests. Physical and mechanical tests of the constituent materials of concrete were also conducted and subsequently used for the design mix of concrete mixes. All experiments and tests in this study were carried out in accordance with Indian Standards (IS) at the Material Testing Laboratory of Kathmandu University, Dhulikhel, Nepal, and Nepal Engineering Lab Pvt. Ltd., Banepa, Nepal.

2.1. Materials

Ordinary Portland Cement (OPC) of 43 grade, with a specific gravity of 3.06, was used for the preparation of all concrete specimens. Physical tests for hydraulic cement were performed as per IS 4031 (Part 1) (1996), IS 4031 (Part 4) (1988), and IS 4031 (Part 11) (1988). The results from various tests performed on cement are presented in Table 1.

Table 1. Properties of cement.

Properties	Results	IS 4031 limits (parts 1, 4, and 11)
Specific gravity	3.06	–
Consistency	32%	–
Fineness	0.80%	< 10%

A well-graded sand passing a 4.75 mm sieve has been used as fine aggregate for the preparation of concrete. Tests for water absorption and specific gravity were performed as per IS 2386 (Part 3) (1963), while sieve analysis was carried out following IS 2386 (Part 1) (1963). The sand conformed to zone II and satisfied the grade limits conforming to IS 383 (2016). The results of physical tests of natural fine aggregate are tabulated in Table 6, while the particle size distribution and particle size distribution curve are presented in Table 2 and Fig. 1.

Table 2. Particle size distribution of natural fine aggregate (NFA).

Sieve size (mm)	% Passing	IS 383 (2016) limits (% passing)
4.75	100	90–100
2.36	86	75–100
1.18	74	55–90
0.60	54	35–59
0.30	26	8–30
0.15	9	0–10

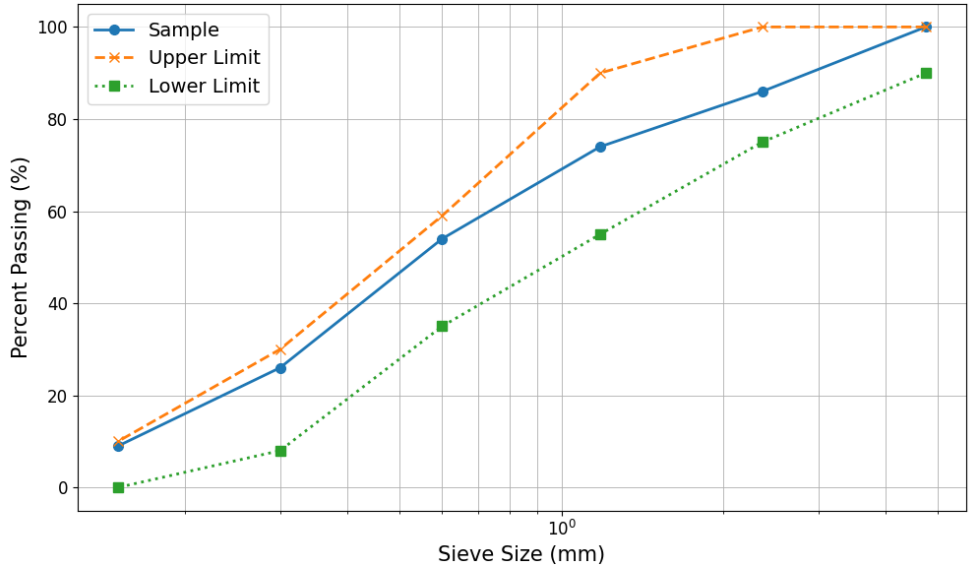

Fig. 1. Particle size distribution curve for natural fine aggregates.

Both natural coarse aggregates (NCA) and recycled crushed brick aggregates (RCBA) were tested for specific gravity, water absorption, Los Angeles abrasion value (LAAV), and aggregate impact value (AIV). Brick aggregates were prepared by manually crushing bricks from a dismantled century-old masonry building located at Sangha, Kabhrepalanchok, Nepal. The preparation process of brick aggregate is illustrated in Fig. 2.

The century-old masonry building from which the bricks were collected and subsequently crushed into brick aggregates is shown in Fig. 3.

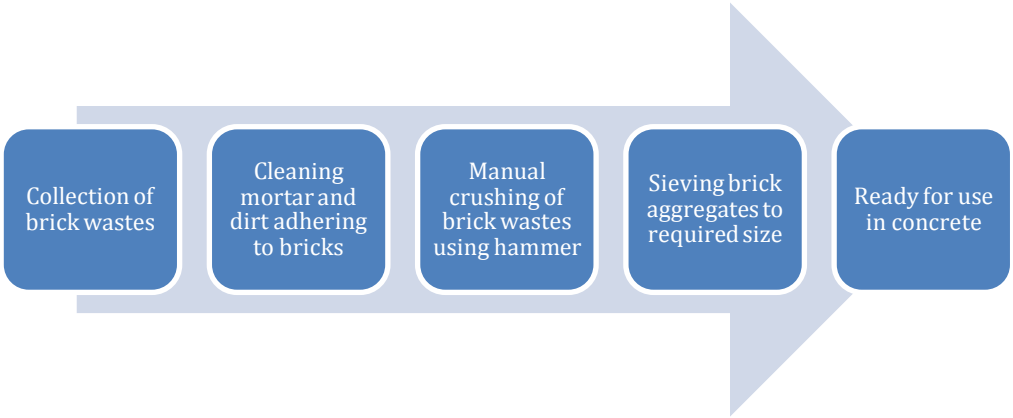

Fig. 2. Preparation process of brick aggregate.

Fig. 3. Collection of bricks and brick aggregates: (a) Century-old brick masonry building located at Sangha, Kabhrepalanchok, Nepal; (b) Dismantled brick from masonry building; (c) Crushed brick aggregates prepared in laboratory.

The specific gravity and water absorption tests were carried out following IS 2386 (Part 3) (1963), while the Los Angeles abrasion test and aggregate impact value test were performed as per IS 2386 (Part 4) (1963). The sieve analysis was conducted following IS 2386 (Part 1) (1963). Both NCA and RCBA were well graded as per IS 383 (2016). The Los Angeles abrasion value (LAAV) and aggregate impact value (AIV) of NCA were within the permissible limits for concrete applications in non-wearing surface (LAAV ≤ 45% and AIV ≤ 50%), whereas RCBA exhibited values exceeding the limits specified in IS 383 (2016). The particle size distributions of NCA and RCBA are presented in Tables 3 and 4. The particle size distribution curve for NCA and RCBA is shown in Fig. 4.

The results from the physical and mechanical tests of the aggregates are compared in Table 5.

The bricks used for the preparation of brick aggregates were approximately a century old, as confirmed by local residents. These bricks were salvaged from a dismantled masonry building constructed using mud mortar. Adhered mud mortar was scraped off and cleaned before crushing the bricks into aggregates. The physical and mechanical properties of the bricks were determined in accordance with IS 1077 (1992), and the test results are summarized in Table 6.

Table 3. Particle size distribution of natural coarse aggregate (NCA).

Sieve size (mm)	% Passing	IS 383 (2016) limits (% passing)
20	100	90–100
10	25	25–55
4.75	1	0–10

Table 4. Particle size distribution of recycled crushed brick aggregate (RCBA).

Sieve size (mm)	% Passing	IS 383 (2016) limits (% passing)
20	100	90–100
10	29	25–55
4.75	1	0–10

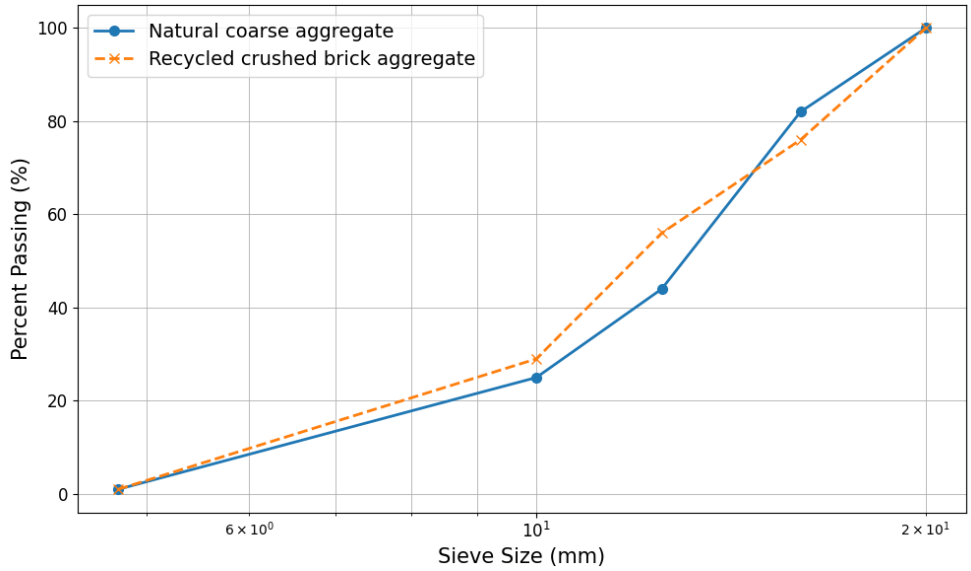

Fig. 4. Particle size distribution curve for natural coarse aggregates and recycled crushed brick aggregate.

Table 5. Test results of aggregates.

Materials	Specific gravity	Water absorption	Open porosity	Apparent density (kg/m³)	Los-Angeles abrasion value	Aggregate impact value
Natural fine aggregate	2.62	1.00%	–	2623.02	–	–
Natural coarse aggregate	2.71	0.60%	1.63%	2702.48	35.60%	15.04%
Recycled crushed brick aggregate	1.61	15.25%	28.94%	2219.46	59.20%	52.94%

Table 6. Experimental results for properties of bricks.

Description	Values
Water absorption (%)	19.51
Apparent porosity (%)	31.12
Bulk dry density (kg/m³)	1597.17
Compressive strength (N/mm²)	4.41
Ultrasonic pulse velocity (UPV) (m/s)	1363.91

2.2. Mix design and preparation

The concrete mix design consisted of five mixes at varying levels of RCBA replacement as coarse aggregate in M20 grade concrete with a water-cement ratio (W/C) of 0.5. The mixes included B0% (control mix), B10%, B20%, B30%, and B100% at 10%, 20%, 30%, and 100% replacement of natural coarse aggregates with recycled crushed brick aggregates by weight, respectively. Mix design calculations were performed following IS 10262 (2019), and the details are presented in Table 7.

Table 7. Proportioning of materials as per the mix design.

Concrete mix	B0%	B10%	B20%	B30%	B100%
Cement (kg/m³)	383	383	383	383	383
Water (kg/m³)	191.58	191.58	191.58	191.58	191.58
Total water-cement ratio	0.535	0.534	0.532	0.53	0.518
Effective water-cement ratio	0.5	0.5	0.5	0.5	0.5
Natural fine aggregate in SSD (kg/m³)	689.58	689.58	689.58	689.58	689.58
Natural coarse aggregate in SSD (kg/m³)	1115.63	1004.07	892.5	780.94	0
Recycled crushed brick aggregate in SSD (kg/m³)	0	66.28	132.56	198.84	662.79

SSD = Saturated Surface Dry

All mixes were prepared with a constant cement content of 383 kg/m³ and designed to achieve a slump of 75 mm, corresponding to medium workability commonly adopted in general construction practice.

To address workability issues, natural fine aggregates (NFA) and natural coarse aggregates (NCA) were washed and oven-dried at 105 ˚C for 24 hours. The additional water required to reach saturated surface dry con-

ditions for NFA and NCA was added during mixing. RCBA was pre-soaked for 2 hours and then dried to saturated surface dry (SSD) condition before mixing. This procedure was adopted to prevent the highly porous RCBA from absorbing water required for the hydration of cement. The pre-wetting duration of 2 hours was selected because RCBA absorbs most of the water during the initial few minutes. The additional water required was calculated based on the water absorption of the coarse and fine aggregates. Consequently, the effective water-cement ratio was maintained at 0.5 while the total water-cement ratio varied from 0.518 to 0.535 depending on the replacement percentage. The total water-cement ratio excludes the water required for pre-saturation of brick aggregates. Preparation of materials, mixing, casting, and curing of concrete for all mixes are illustrated in Fig. 5.

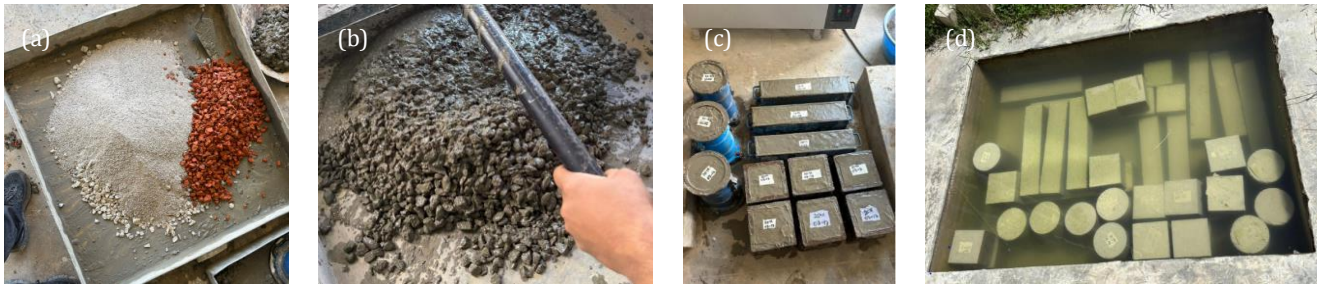

Fig. 5. Preparation process of concrete: (a) Preparation of materials; (b) Mixing of concrete; (c) Casting of concrete specimens; (d) Curing of concrete specimens.

2.3. Test specimens and procedure

Concrete cubes of dimensions 150 mm x 150 mm x 150 mm were cast for compressive strength testing, while cylindrical specimens of 150 mm diameter and 300 mm height were used for splitting tensile strength tests. Similarly, beam specimens measuring 500 mm x 100 mm x 100 mm were cast to evaluate the flexural strength of concrete. Batching, mixing, and casting were done in accordance with relevant Indian Standards. After casting, the concrete specimens were demolded after 24 hours and cured by immersion in a curing pond at a temperature of 23 ± 2 ˚C until the time of testing. All mechanical tests were conducted at 28 days in accordance with IS 516 (Part I/Sec 1) (2021). The tests were performed on calibration-certified testing machines, and the alignment of loading platens was also checked before testing. Error bars were calculated based on the standard deviation obtained from the total number of specimens tested for each mix. Furthermore, the variability of test results was assessed using the coefficient of variation (CoV), calculated as the ratio of standard deviation to mean value. The number of specimens for each mix complied with IS 456 (2000), which specifies a minimum of three specimens per sample, and the number of specimens per mix used in this study is consistent with investigations on recycled brick aggregate concrete (De Brito et al. 2005; Adamson et al. 2015). The number of specimens prepared for each mix and for different testing is shown in Table 8.

2.4. Non-destructive test

Ultrasonic pulse velocity (UPV) test was conducted on concrete cubes before compression strength testing at 28 days. The tests were performed using the direct transmission method on the cubes in SSD conditions, approximately one hour after removal from the curing pond. The time taken by the pulse to travel through the cube was measured. The ultrasonic pulse velocity was calculated by dividing the travel path length by the measured time. The device used for the UPV test was RTUL UX460X, and the calibration of the device was done by observing the time required for the pulse to travel through a standard prism of known time. The UPV was compared against the limits specified by IS 516 (Part 5/Sec 1) (2018) to determine the quality of the concrete. The direct method of the ultrasonic pulse velocity test performed on a concrete cube is shown in Fig. 6.

Table 8. Number of experimental specimens prepared.

	Number of specimens		
	Concrete cubes	Concrete cylinders	Concrete beams
B0% (control mix)	5	3	3
B10%	5	3	3
B20%	6	3	3
B30%	6	3	3
B100%	3	3	3
Total	25	15	15

Fig. 6. Ultrasonic pulse velocity test on a concrete cube using the direct method.

3. Results and Discussion

3.1. Bricks and brick aggregates

The bricks used in this study were collected from a century-old dismantled masonry building and subsequently crushed to produce recycled crushed brick aggregates. The bricks exhibited an average compressive strength of 4.41 MPa and a water absorption of 19.51%. According to IS 1077 (1992), these bricks can be classified as Class 3.5 bricks based on their compressive strength and water absorption. The UPV of the century-old bricks was evaluated against the quality assessment criteria for burnt clay bricks by Azam et al. (2022). The measured pulse velocity was below 2000 m/s, indicating poor brick quality and further corroborating the classification based on mechanical properties.

The physical and mechanical properties of the century-old bricks used in this study are consistent with those reported for historic and ancient bricks in the literature. Studies on historic bricks in Nepal have reported dry density values ranging from 1.2 to 1.8 g/cm^3, water absorption of 10 to 28%, apparent porosity of 17 to 33%, and compressive strength of 3.49 to 26.9 MPa (Parajuli 2012; Parajuli et al. 2020; Bhattarai et al. 2018). Similarly, studies on modern bricks in Nepal have reported dry density values of 1.1 to 2.82 g/cm^3, water absorption of 5 to 30%, apparent porosity of 10 to 53.99%, and compressive strength of 3.35 to 23.49 MPa (Chapagain et al. 2020; Bohara et al. 2020; Subedi 2020; Shrestha, 2019; Khanal and Paudel, 2023; Thapaliya et al. 2024).

A comparative summary of physical and mechanical properties for modern bricks, old bricks, and bricks used in this study is presented in Table 9.

Table 9. Physical and mechanical properties of modern and old bricks of Nepal.

Author	Water absorption (%)	Compressive strength (MPa)	Apparent porosity (%)	Dry density (g/cm^3)	Remarks
Parajuli (2012)	–	11.03	–	1.77	Historical bricks from Patan Durbar Square
Bhattarai et al. (2018)	10 to 28%	5.00 to 23.00	17 to 33%	1.2 to 1.8	Ancient brick of Nepal
Shrestha (2019)	8.8 to 23.93%	7.83 to 22.1	19.28 to 53.99%	1.55 to 2.82	Modern bricks
Bohara et al. (2020)	11 to 23%	15.6 to 17.1	19 to 37%	1.5 to 1.65	Modern bricks
Chapagain et al. (2020)	5 to 30%	3.35 to 10.53	10 to 40%	1.1 to 2.15	Modern bricks
Subedi (2020)	4 to 12%	3.72 to 20.16	-	1.34 to 1.82	Modern bricks
Parajuli et al. (2020)	13 to 18%	3.49 to 26.90	–	–	Historical bricks from Shreemahal and Singhadurbar
Khanal and Paudel (2023)	9.36 to 16.89%	7.02 to 23.49	18.25 to 27.95	1.65 to 1.949	Modern bricks
Thapaliya et al. (2024)	6 to 25%	8.6 to 15		1 to 2	Modern bricks
This study	19.51%	4.41	31.12%	1.6	Century-old brick

The physical and mechanical properties of recycled crushed brick aggregates (RCBA) were further compared with those reported in previous studies (Debieb and Kenai 2008; Aliabdo et al. 2014; Gyawali 2022; Hachemi et al. 2022; Cachim 2009; Adamson et al. 2015). These studies reported water absorption values ranging from 1.79 to 20%, specific gravity from 2.04 to 2.40, porosity from 9.5 to 38.82%, and Los Angeles abrasion values between 30.06 to 31.6%.

In contrast, the RCBA used in this study exhibited a lower specific gravity of 1.61, which can be attributed to the high porosity and lower density of century-old bricks from which the aggregates were derived. Although the water absorption and porosity values of RCBA were within the ranges reported in previous studies, they were relatively higher than those of NCA. The Los Angeles abrasion value of RCBA was higher and exceeded the limits specified by IS 383 (2016), indicating lower abrasion resistance.

Overall, the physico-mechanical behavior of the old bricks used in this study aligns closely with that of historic bricks and also falls within the broad range of properties reported for modern bricks, albeit toward the lower strength and higher porosity. The origin of these properties differs, as the characteristics of century-old bricks are primarily influenced by long-term aging, environmental exposure, and material degradation rather than a controlled manufacturing process for modern bricks. These factors likely contributed to the lower density, higher water absorption, higher porosity, reduced abrasion resistance, and impact resistance observed in the RCBA used in this study as compared to natural coarse aggregates.

3.2. Density of concrete

The density of concrete was determined by measuring the mass of each cube and dividing it by its volume. The density of the recycled brick aggregate concrete (RBAC) decreased with increasing brick aggregate replacement levels. The maximum reduction in density was 13.24% for B100% mix compared to the control mix. This decreasing trend is consistent with the findings reported by De Brito et al. (2005) and Bhanbhro et al. (2014), who observed density reductions of 9.18% and 16%, at 100% replacement, respectively.

The decrement in density is primarily attributed to the lower specific gravity of brick aggregates compared to natural coarse aggregates, resulting in a relatively lighter concrete. The average density values and corresponding coefficient of variation are presented in Table 10. The CoV values ranged from 0.58% to 1.07%, indicating excellent uniformity of the concrete specimens. The density variation across different mixes with error bars is illustrated in Fig. 7.

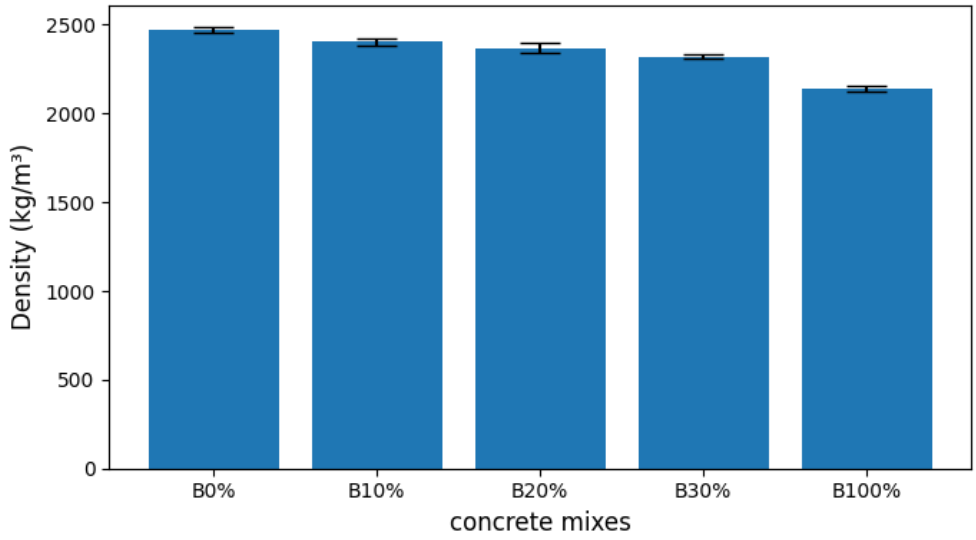

Fig. 7. Density values of various concrete mixes at 28 days.

3.3. Compressive strength

The compressive strength was determined from the peak load at failure, and crack patterns were also observed. The control mix (B0%) exhibited the highest compressive strength, while the strength decreased with increasing RCBA replacement. The reduction in compressive strength relative to the control mix were 0.72%, 3.27%, 5.99%, and 28.26% at 10%, 20%, 30%, and 100% replacement, respectively. The reduction in compressive strength with the increasing replacement percentage is consistent with the findings of previous studies (Debieb and Kenai 2008; Aliabdo et al. 2014; Bhanbhro et al. 2014).

The reduction in compressive strength can be attributed to the replacement of NCA with RCBA, which possesses lower density, higher water absorption, and microcracking induced during crushing. These characteristics lead to a weaker aggregate skeleton and a heterogeneous interfacial transition zone (ITZ) as reported by Silva et al. (2014). Under compressive loading, brick aggregates act as stress concentrators, promoting crack initiation and propagation at the aggregate-paste interface rather than through the cement matrix (Xiao et al. 2012; Silva et al. 2014). At lower replacement levels, brick aggregates are distributed discontinuously within the concrete matrix, which limits the crack connectivity and allows load transfers to be governed predominantly by NCA and hydrated cement paste. This explains the relatively small reduction in compressive strength observed at partial replacement levels, whereas the pronounced loss of strength at 100% replacement is attributed to the formation of a continuous weak aggregate-paste network.

The average compressive strength values and corresponding CoV are presented in Table 10, while Fig. 8 shows the compressive strength results with error bars.

The compressive strength was evaluated as the average of at least three specimens for each concrete mix, or based on the number of specimens indicated in Table 8. In accordance with IS 516 (Part 1/Sec 1) (2021), test results deviating more than ± 15% from the mean compressive strength were treated as outliers and excluded from analysis. One outlier was identified in both B10% and B20% mixes. The standard deviation for mixes B0% to B100% were 1.22, 1.74, 1.54, 2.08, and 0.4, all of which are smaller than the standard deviation value of 4 specified for M20 concrete. The CoV values ranged from 2.22% to 8.86%, indicating low variability and good repeatability of test results after exclusion of outliers.

The failure patterns of the cubes were examined visually, and the Fig. 9 illustrates the observed failure for different concrete mixes. Failure was mostly due to the formation of vertical cracks resulting from laterally induced tensile stress perpendicular to the applied compressive load. Cone-shaped failure was also observed in a limited number of specimens. Overall, the failure behavior was satisfactory as specified in IS 516 (Part 1/Sec 1) (2021).

Table 10. Average values for physical and mechanical properties of concrete with their CoVs.

Concrete mix	Density (kg/m³)	CoV	Compressive strength (MPa)	CoV	Splitting tensile strength (MPa)	CoV	Flexural strength (MPa)	CoV	UPV (m/s)	CoV
B0%	2467.79	0.67	25.05	4.88	2.92	2.14	4.13	6.43	4429.11	1.12
B10%	2404.03	0.80	24.51	7.10	2.79	2.05	3.99	0.68	4152.17	1.30
B20%	2369.58	1.07	24.23	6.37	2.69	1.85	3.95	3.28	4083.14	1.38
B30%	2319.31	0.58	23.55	8.86	2.61	3.17	3.87	1.06	4046.92	0.85
B100%	2141.04	0.65	17.97	2.22	2.19	1.14	3.70	0.88	3655.69	0.28

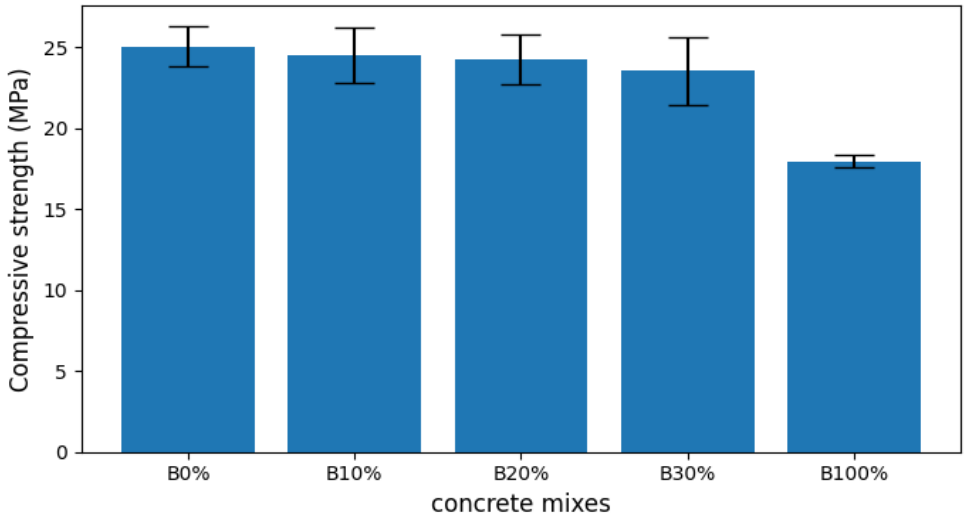

Fig. 8. Compressive strength values of various concrete mixes at 28 days.

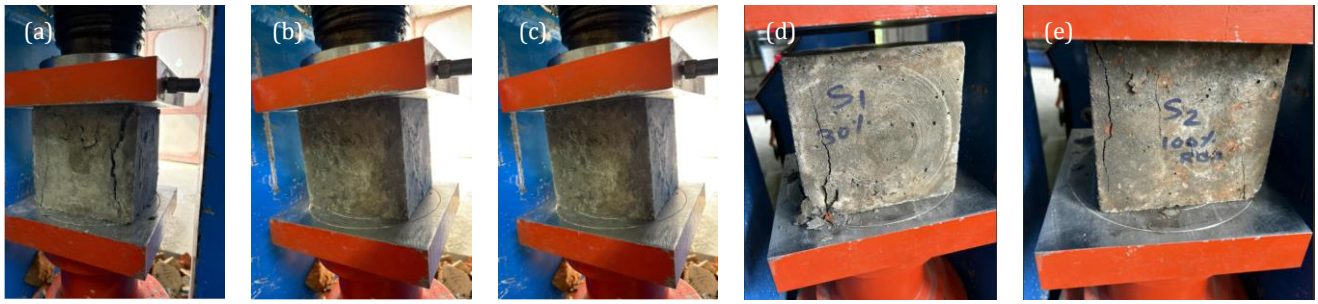

Fig. 9. Typical failure of cubes at different replacement percentages: (a) 0%; (b) 10%; (c) 20%; (d)30%; (e)100%.

3.4. Splitting tensile strength

The splitting tensile strength test of concrete was performed as per IS 516 (Part I/Sec 1) (2021), in which the load was applied to the cylindrical surface radially. The control mix (B0%) exhibited the highest tensile strength, and the tensile strength decreased with an increase in the brick aggregates replacement levels. The decrement in tensile strength relative to the control mix at 10%, 20%, 30%, and 100% replacements were 4.68%, 8.06%, 10.65% and 25.16%, respectively. This decreasing trend of tensile strength is similar to compressive strength and agrees with the findings of Aliabdo et al. (2014), who reported a reduction in tensile strength with increasing RCBA replacement percentage.

The average tensile strength values and their corresponding coefficient of variation are presented in Table 10. Furthermore, the splitting tensile strength results exhibited very low variability, with CoV values ranging from 1.14% to 3.17%, indicating excellent repeatability of experimental results. The tensile strength for various concrete mixes with error bars is presented in Fig. 10.

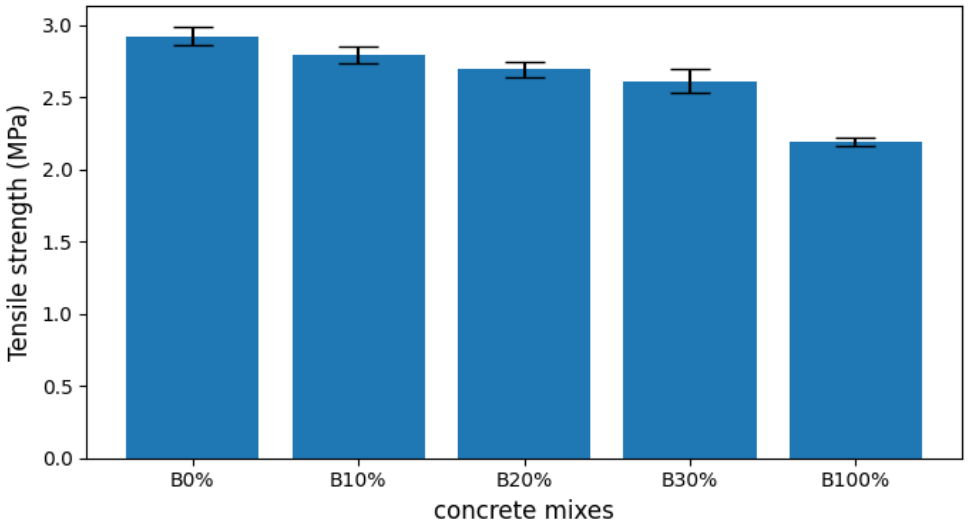

Fig. 10. Splitting tensile strength values of various concrete mixes at 28 days.

The failure was governed by the development of lateral tensile stresses perpendicular to the applied compressive load. This initiated the crack along the loading line, which propagated through the cylinder, resulting in a sudden, brittle failure once the tensile strength of concrete was exceeded. The specimens were split into two halves along the longitudinal axis, as shown in Fig. 11.

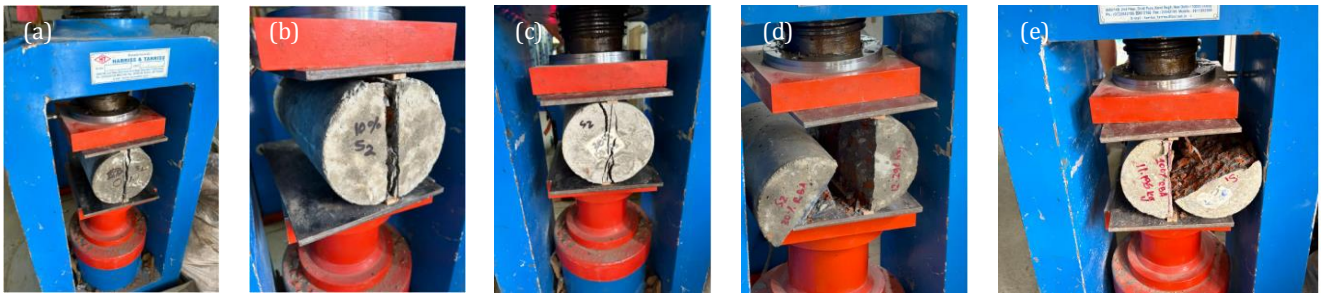

Fig. 11. Typical failure of cylinders at different replacement percentages: (a) 0%; (b) 10%; (c) 20%; (d)30%; (e)100%.

3.5. Flexural strength

Plain cement concrete beams with dimensions 500 x 100 x 100 mm were tested at 28 days to determine the modulus of rupture (MOR) as per IS 516 (Part 1/Sec 1) (2021). A four-point bending test was employed, in which the load was applied through two points at the top, while two supports were provided at the bottom. The B0% mix showed the highest modulus of rupture; however, all concrete mixes exhibited higher experimentally obtained MOR values higher than those calculated using the empirical relationship in IS 456 (2000). The decrease in flexural strength as compared to the control mix at 10%, 20%, 30%, and 100% replacements were 2.95%, 4.42%, 6.32% and 7.58%, respectively. This reduction in flexural strength is similar to the declining trend of compressive strength, where strength decreases with an increase in aggregate replacement percentage and aligns with the findings of De Brito et al. (2005).

The average flexural strength values and the corresponding coefficient of variation are presented in Table 10. The results showed low variability, with CoV values ranging from 0.68% to 6.43%, indicating good to excellent repeatability of experimental data. The flexural strength results with error bars is illustrated in Fig. 12.

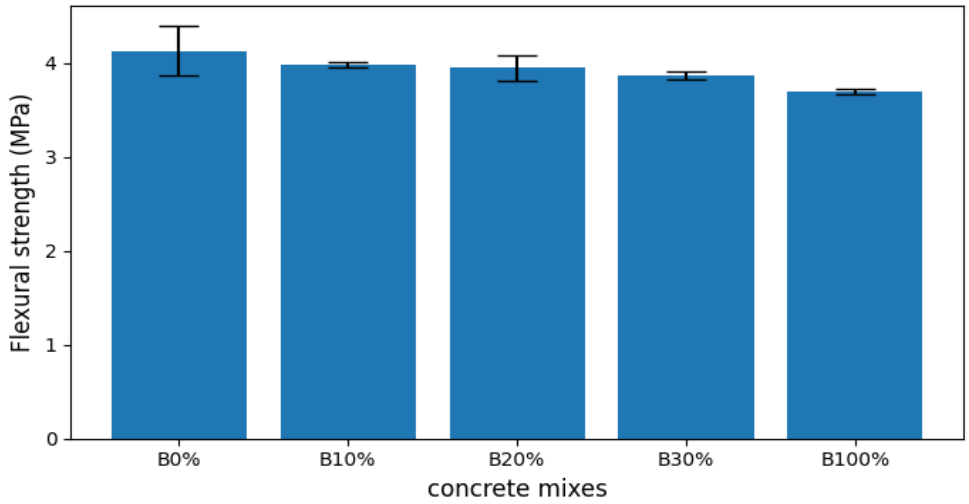

Fig. 12. Flexural tensile strength values of various concrete mixes at 28 days.

Failure of the beams occurred due to the development of flexure cracks parallel to the direction of loading. Cracks initiated from the bottom face and propagated toward the top of the beam. For all concrete mixes, failure was observed in the central region of the beam, and was found to be satisfactory as per IS 516 (Part 1/Sec 1) (2021). The observed failure patterns are presented in Fig. 13.

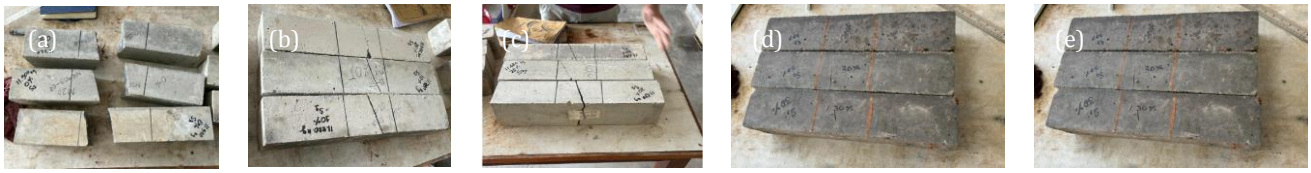

Fig. 13. Typical failure of beams at different replacement percentages: (a) 0%; (b) 10%; (c) 20%; (d)30%; (e)100%.

Fig. 14 illustrates the failure modes of concrete cubes, cylinders, and beams in compression, indirect tension, and flexure, respectively. The post-failure cross-sections of the specimens reveal the distribution of brick aggregates within the concrete matrix.

Fig. 14. Failure of different concrete specimens showing cross-section:
(a) Cubes of B30%; (b) Cylinders of B30%; (c) Cylinders of B100%; (d) Beams of B100%.

3.6. Strength index

Strength index was developed to quantify the contribution of natural coarse aggregates and brick aggregates to the overall strength of concrete, following an approach similar to Cachim (2009). The specific strength ratio, *R*, is given by:

$$R = \frac{f}{q} \tag{1}$$

where *f* is the compressive strength of concrete in MPa, while *q* denotes the quantity of natural coarse aggregate in percentage. The parameter R_n represents the contribution of natural coarse aggregates to overall strength and is the specific strength ratio of concrete with natural coarse aggregates only.

The parameter R_b expresses the contribution of unit natural coarse aggregates to the strength of concrete. $R_n = R_b$ when $q = 100\%$, while R_r is the contribution of brick aggregates to overall strength:

$$R_r = R_b - R_a \tag{2}$$

The specific strength ratio, *K*, is:

$$K = \frac{R_b}{R_n} \tag{3}$$

which is greater than 1 if the reduction in strength is less than the percentage of natural aggregates replaced. Additionally, *P* represents the contribution of brick aggregates to the overall strength of concrete in percentage and is defined as:

$$P = \frac{100R_r}{R_b} \tag{4}$$

The *P* value implies that if it is greater than the amount of aggregate replaced, then it signifies a positive contribution of brick aggregate to overall strength. The strength index developed for concrete cubes tested in compression at 28 days is presented in Table 11. A slight reduction (0.65%) in the contribution of brick aggregate to overall strength at 10% replacement. This contribution of brick aggregates has further decreased with an increase in brick aggregate replacement percentage, as observed for B20% and B30% mixes.

Table 11. Strength Index based on compressive strength.

Concrete mixes	*q*	*f*	R_b	R_r	*K*	*P*
B0%	100	25.05	0.25	0	1	0
B10%	90	24.87	0.28	0.03	1.10	9.35
B20%	80	24.23	0.30	0.05	1.21	17.29
B30%	70	23.55	0.34	0.09	1.34	25.54

3.7. Ultrasonic pulse velocity

The UPV decreased with increasing brick aggregate replacement, while the control mix (B0%) exhibited the highest UPV values. The UPV values were further used to assess the quality of RBAC. According to the limits specified by IS 516 (Part 5/Sec 1) (2018), all concrete mixes except B100% exhibited excellent concrete quality (UPV > 4000 m/s), whereas B100% mix showed doubtful quality (UPV = 3000 m/s to 3750 m/s). As the proportion of brick aggregates increased, the UPV has decreased, which is in agreement with the findings reported by Rao (2018) and Hachemi et al. (2022).

This decrement in UPV is attributed to the higher porosity of RCBA compared to NCA. This increased porosity resulted in greater scattering and attenuation of ultrasonic waves, leading to longer travel times and lower UPV. This trend indicates that increasing brick aggregate content results in reduced concrete density, which is associated with lower compressive strength and degradation in overall concrete quality. Table 10 presents the average UPV values with their coefficient of variation. The CoV for UPV tests ranged from 0.285% to 1.379%, indicating a low variability of results. The UPV for different concrete mixes with error bars are presented in Fig. 15.

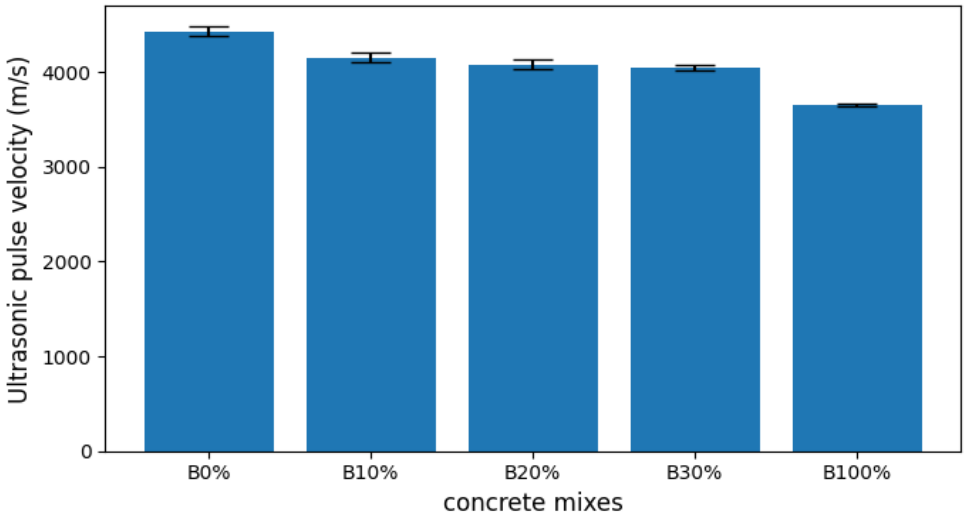

Fig. 15. UPV values of various concrete mixes at 28 days.

3.8. Relationship between physical and mechanical properties of concrete

The results from the experimental test of RBAC were plotted against the density, and linear regression analysis was performed to quantify the influence of density on the mechanical strengths of concrete. Fig. 16 illustrates the relationship between density and strength properties of RBAC. The coefficients of determination (R^2) obtained were 0.93, 0.99, and 0.96 for density versus compressive strength, splitting tensile strength, and flexural strength, respectively. These high R^2 values indicate a strong positive correlation between density and mechanical properties, demonstrating that an increase in density leads to improved mechanical performance of RBAC.

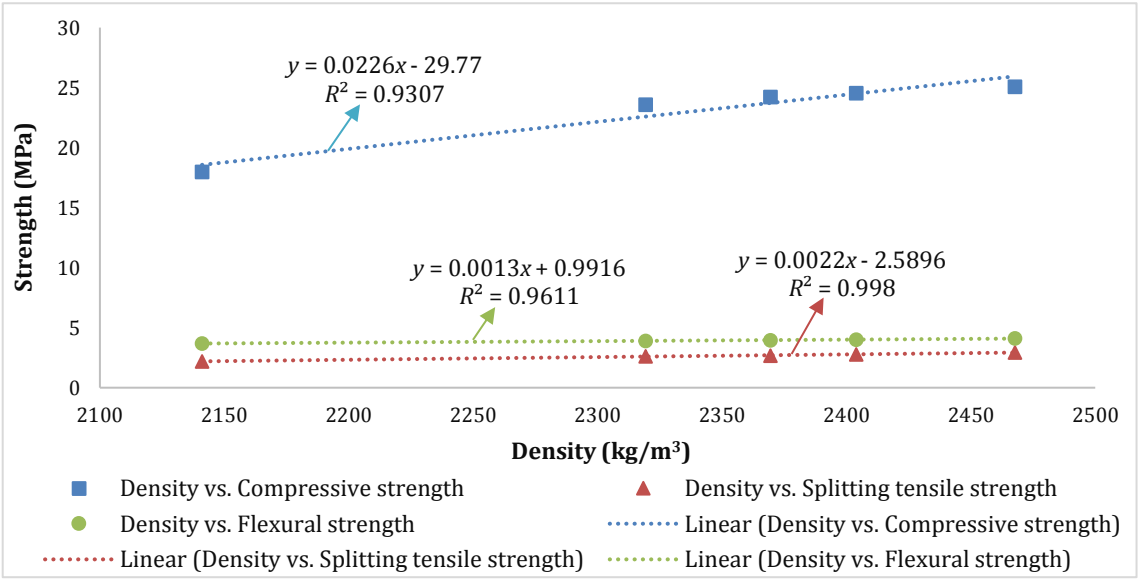

Fig. 16. Relationship between density and strength properties of RBAC.

Similarly, linear regression analysis was conducted to establish relationships among the mechanical properties themselves. Fig. 17 presents the correlation between compressive, splitting and flexural strength of recycled brick aggregate concrete. The coefficients of determination (R^2) were 0.94 for splitting tensile strength versus compressive strength and 0.80 for flexural strength versus compressive strength, respectively. These values indicate a significant correlation between the mechanical properties of recycled concrete, confirming that compressive strength increases with increasing splitting tensile and flexural strengths.

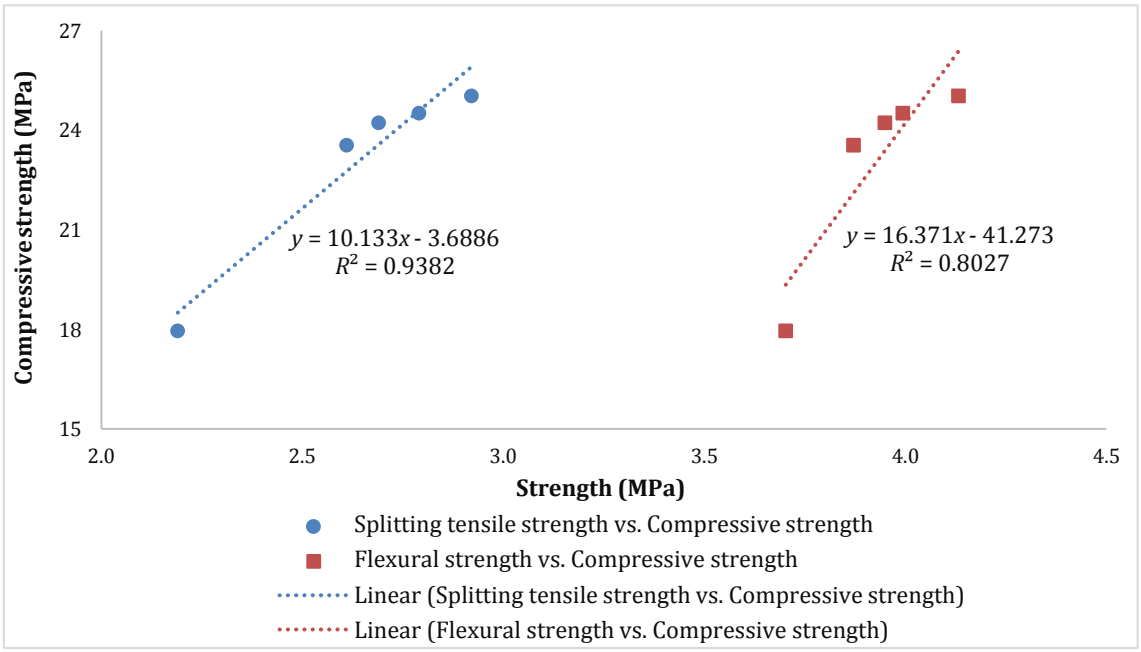

Fig. 17. Relationship between compressive, splitting and flexural strength values of RBAC.

3.9. Comparison of the mechanical performance of recycled brick aggregate concrete

The experimental findings of the present study were compared with findings reported in previous literature. Earlier studies have reported a decrement in the mechanical performance of recycled concrete with increasing brick aggregate replacement percentage, and the results of this study are generally consistent with these findings. Table 12 presents a comparative summary of the mechanical performance of recycled brick aggregate concrete reported in previous studies and the present investigation.

Table 12. Comparison of mechanical properties from various studies.

Authors	Coarse aggregate replacement percentage	W/C ratio	Variation in strength relative to the control mix		
			Compressive strength	Tensile strength	Flexural strength
De Brito et al. (2005)	100%	0.6	−45.00%	–	−25.71%
Debieb and Kenai (2008)	100%	0.57	−35.00%	–	−33.11%
Cachim (2009)	30%	0.45	−10.00% to −24.00%	−10% to −20%	–
		0.5	−10.00% to −20.00%	−12.50% to +4.27%	–
Aliabdo et al. (2014)	100%	0.5	−36.50%	−28.10%	–
		0.7	−30.80%	−60.00%	–
Bhanbhro et al. (2014)	100%	0.5	−37.00%	–	–
Gyawali (2022)	20%	0.5 (oven-dried aggregates)	10.12%	–	–
		0.5 (saturated aggregates)	−14.98%	–	–
This study	10%	0.5	−0.72%	−4.68%	−2.95%
	20%		−3.27%	−8.06%	−4.42%
	30%		−5.99%	−10.65%	−6.32%
	100%		−28.26%	−25.16%	−7.58%

At 100% brick aggregate replacement, the reduction in compressive strength observed in the present study is consistent with findings from previous studies (Debieb and Kenai 2008; Aliabdo et al. 2014; Bhanbhro et al. 2014). Although these studies have reported higher strength reductions, the results are comparable in magnitude. At replacement levels below 100%, most studies have reported a reduction in compressive strength. An exception is reported by Gyawali (2022), who observed a strength gain at 20% replacement when oven-dried brick aggregates were used. In contrast, the present study showed lower strength reductions relative to control mix up to 30% replacement.

Similarly, the percentage reduction in tensile strength at 100% replacement levels is consistent with the results reported by Aliabdo et al. (2014) for a water-cement ratio of 0.5. Although Cachim (2009) reported a tensile strength gain at 30% replacement, the present study showed a gradual reduction in tensile strength with increasing brick aggregate concrete. De Brito et al. (2005) and Debieb and Kenai (2008) reported 25%-34% reductions in flexural strength at 100% replacements. In comparison, the present study recorded a substantially lower reduction of about 8%, despite using brick aggregates sourced from century-old masonry.

Overall, the recycled brick aggregate concrete in this study exhibited smaller percentage reductions in mechanical strength relative to the control mix as compared to previously reported studies, despite the inherently weaker properties of aggregates. This behavior suggests that aggregate-level indicators such as abrasion and impact resistance alone do not fully govern the strength of concrete. One contributing factor may be the higher water absorption capacity of brick aggregates, which can supply additional water for cement hydration, causing an internal curing effect (Cachim 2009; Aliabdo et al 2014; Xiao et al. 2012). Moreover, strict control of the effective water-cement ratio through pre-soaking of brick aggregates to a saturated surface dry condition prevented absorption of mixing water. Even if the absorbed water does not actively participate in cement hydration, it remains within the brick pores, contributing to a denser aggregate structure (Cachim 2009). Collectively, these factors likely contributed to the improved strength retention observed in the present study.

4. Conclusions

This study investigated the effects of replacing natural coarse aggregate with recycled crushed brick aggregates derived from century-old bricks on the mechanical properties of the resulting concrete. The conclusions of the study are drawn as follows:

- The properties of century-old bricks in this study fall within the broader range reported for modern bricks; however, the properties of resulting brick aggregates are comparatively inferior, which may be due to long term environmental exposure and material degradation with aging.
- Brick aggregates exhibited higher porosity and water absorption than natural coarse aggregates. Therefore, the water required for mixing needs to be adjusted to prevent the brick aggregates from absorbing mixing water and to maintain effective cement hydration.
- Brick aggregates presented lower abrasion and impact resistance compared to natural coarse aggregates; however, the mechanical performance of the resulting RBAC was satisfactory based on experimental results of concrete at 28 days.
- Brick aggregates showed lower specific gravity and density as compared to natural coarse aggregates, which resulted in reduced compressive strength with increasing replacement levels of natural coarse aggregates.
- Compressive strength decreased with increasing brick aggregate content; however, all mixes except B100% satisfied the strength requirements for M20 concrete.
- Both splitting tensile strength and flexural strength decreased with increasing brick aggregate replacement. Nevertheless, the experimentally obtained flexural strength values for all mixes exceeded the theoretical values predicted by the empirical relationship specified in IS 456 (2000).
- Ultrasonic pulse velocity decreased with increasing replacement of brick aggregates, supporting the influence of lower density and higher porosity of brick aggregates on reduced compressive strength.
- According to IS 516 (Part 5/Sec 1) (2018), all concrete mixes except B100% exhibited excellent concrete quality based on ultrasonic pulse velocity measurements, while B100% mix demonstrated doubtful concrete quality.
- Strength index analysis indicated that the contribution of brick aggregates to the overall compressive strength of the concrete decreases progressively with increasing brick aggregate replacement levels.

From the results of this study, it can be summarized that natural coarse aggregates can be replaced by recycled coarse brick aggregates up to 30% without significant loss in compressive strength, while achieving adequate flexural strength at all replacement levels. This demonstrates the potential for recycling old masonry bricks as brick aggregates in concrete. The findings suggest that recycled brick aggregates derived from old bricks may be used in non-structural concrete, low-load-bearing concrete structures subjected primarily to gravity loads, and the production of concrete blocks where sustainability is prioritized despite the relatively low abrasion and impact resistance of brick aggregates. However, the long-term durability performance of RBAC was not investigated in this study.

This study was limited to laboratory-scale testing and focused mainly on the mechanical properties of recycled brick aggregate concrete using brick aggregates from a single century-old masonry building. The number of test specimens was limited; therefore, advanced statistical analysis was not considered. Microstructural characterization was beyond the scope of this study, and interpretations related to porosity and interfacial transition zone behavior are based on indirect experimental observations and existing literature.

Future studies should focus on the durability performance and microstructural analysis of recycled brick ag-

gregate concrete. Further investigations are also needed to evaluate the influence of brick age, firing characteristics, source variability, and properties of brick aggregates on the performance of recycled concrete. In addition, design mix optimization of recycled concrete at higher replacement levels using mineral and chemical admixtures could also be a suitable area for further study.

Acknowledgements

The authors would like to thank Mr. Bibek Bhusal, Mr. Aditya Deo, Mr. Anubhav Chaurasiya, Mr. Sanjiv Maharjan, and Mr. Saroj Sapkota from Kathmandu University, Nepal because of their assistance in laboratory works to execute this study and further authors acknowledge Department of Civil Engineering, Kathmandu University, Nepal for the laboratory facility and materials for execution of the research.

Funding

The authors received no financial support for the research, authorship, and/or publication of this manuscript.

Conflict of Interest

The authors declare no potential conflicts of interest with respect to the research, authorship, and/or publication of this manuscript.

Data Availability

The datasets generated and/or analyzed during the current study are not publicly available but are available from the corresponding author upon reasonable request.

AI Assistance

No AI-based tools were used in the preparation of this manuscript.

Author Contributions

All authors made substantial contributions to the conception and design of the study, acquisition of data, analysis and interpretation of data; drafted or critically revised the manuscript for important intellectual content; and approved the final version to be published.

REFERENCES

Aboalella AA, Elmalky A (2023). Use of crushed bricks and recycled concrete as replacement for fine and coarse aggregates for sustainable concrete production. *Challenge Journal of Concrete Research Letters*, 14(2), 39–46.

Adamson M, Razmjoo A, Poursaee A (2015). Durability of concrete incorporating crushed brick as coarse aggregate. *Construction and Building Materials*, 94, 426–432.

Aliabdo AA, Abd-Elmoaty A-E M, Hassan HH (2014). Utilization of crushed clay brick in concrete industry. *Alexandria Engineering Journal*, 53, 151–168.

Azam R, Riaz MR, Haq EU, Shihata A, Zawam M (2022). Development of quality assessment criteria for burnt clay bricks of different ages based on ultrasonic pulse velocity test. *Buildings*, 12, 1069.

Bajracharya S, Phuyal S, Acharya S, Timilsena S, Regmi S, Chaudhary UK, Nepal B, Shrestha AR (2025). Sustainability assessment of recycled concrete aggregate in the Kathmandu Valley: a comparative analysis with natural coarse aggregate. *Discover Civil Engineering*, 2, 78.

Basit A, Hameed R, Abbas S, Karam M, Shahzad S, Kazmi S, Munir M (2024). Impact of recycled concrete and brick aggregates on the flexural and bond performance of reinforced concrete. *Applied Sciences*, 14, 2719.

Bhanbhro R, Memon I, Ansari A, Shah A, Memon BA (2014). Properties evaluation of concrete using local used bricks as coarse aggregate. *Engineering*, 6, 211–216.

Bhatta N, Adhikari A, Ghimire A, Bhandari N, Subedi A, Sahani K (2024). Comparing crushed brick as coarse aggregate substitute in concrete: experimental vs. numerical study. *Iranian Journal of Science and Technology, Transactions of Civil Engineering*, 48, 4255–4274.

Bhattarai J, Ghale DB, Chapagain YP, Bohara NB, Duwal N (2018). Study on the physical and mechanical properties of ancient clay brick samples of Kathmandu Valley, Nepal. *Tribhuvan University Journal*, 32, 1–18.

Bohara N, Ghale D, Chapagain Y, Duwal N, Bhattarai J (2020). Effect of firing temperature on physico-mechanical properties of contemporary clay brick productions in Lalitpur, Nepal. *Bangladesh Journal of Scientific and Industrial Research*, 55, 43–52.

Cachim PB (2009). Mechanical properties of brick aggregate concrete. *Construction and Building Materials*, 23, 1292–1297.

Central Bureau of Statistics (2021). National Population and Housing Census 2021. National Statistics Office, Office of the Prime Minister and Council of Ministers, Government of Nepal. https://censusnepal.cbs.gov.np/results [accessed 27-10-2025].

Rao MC (2018). Properties of recycled aggregate and recycled aggregate concrete: effect of parent concrete. *Asian Journal of Civil Engineering*, 19, 103–110.

Chapagain YP, Sapkota S, Ghale DB, Bohara NB, Duwal N, Bhattarai J (2020). A case study on mineralogy and physico-mechanical properties of commercial bricks produced in Nepal. *SN Applied Sciences*, 2, 1856.

De Brito J, Agrela F, Silva RV (2019). Construction and demolition waste. In: New Trends in Eco-Efficient and Recycled Concrete. Elsevier, pp. 1–22.

De Brito J, Pereira AS, Correia JR (2005). Mechanical behaviour of non-structural concrete made with recycled ceramic aggregates. *Cement and Concrete Composites*, 27, 429–433.

Debieb F, Kenai S (2008). The use of coarse and fine crushed bricks as aggregate in concrete. *Construction and Building Materials*, 22, 886–893.

Gyawali TR (2022). Re-use of concrete/brick debris emerged from big earthquake in recycled concrete with zero residues. *Cleaner Waste Systems*, 2, 100007.

Hachemi S, Khattab M, Benzetta H (2022). The effects of recycled brick and water/cement ratios on the physical and mechanical performance of recycled aggregates concrete. *Innovative Infrastructure Solutions*, 7, 270.

IS 383 (2016). Coarse and fine aggregate for concrete – Specification. Bureau of Indian Standards, New Delhi, India.

IS 456 (2000). Plain and reinforced concrete – Code of practice. Bureau of Indian Standards, New Delhi, India.

IS 516 (Part I/Sec 1) (2021). Method of tests for strength of concrete – Part I: Determination of strength of hardened concrete. Bureau of Indian Standards, New Delhi, India.

IS 516 (Part 5/Sec 1) (2018). Method of tests for strength of concrete – Part 5: Non-destructive testing of concrete – Section 1: Ultrasonic pulse velocity. Bureau of Indian Standards, New Delhi, India.

IS 1077 (1992). Common burnt clay building bricks – Specification. Bureau of Indian Standards, New Delhi, India.

IS 2386 (Part I) (1963). Methods of test for aggregates for concrete – Part I: Particle size and shape. Bureau of Indian Standards, New Delhi, India.

IS 2386 (Part III) (1963). Methods of test for aggregates for concrete – Part III: Specific gravity, density, voids, absorption and bulking. Bureau of Indian Standards, New Delhi, India.

IS 2386 (Part IV) (1963). Methods of test for aggregates for concrete – Part IV: Mechanical properties. Bureau of Indian Standards, New Delhi, India.

IS 4031 (Part 1) (1996). Methods of physical tests for hydraulic cement – Part 1: Determination of fineness by sieving. Bureau of Indian Standards, New Delhi, India.

IS 4031 (Part 4) (1988). Methods of physical tests for hydraulic cement – Part 4: Determination of consistency of standard cement paste. Bureau of Indian Standards, New Delhi, India

IS 4031 (Part 11) (1988). Methods of physical tests for hydraulic cement – Part 11: Determination of density. Bureau of Indian Standards, New Delhi, India.

IS 10262 (2019). Concrete mix proportioning – Guidelines. Bureau of Indian Standards, New Delhi, India.

Khadka A, Timisina P, Adhikari S (2025). Comparative analysis of compressive strength of natural and brick aggregate concrete. *Journal of UTEC Engineering and Management*, 3, 112–123.

Khanal D, Paudel MR (2023). Quality assessment of bricks produced in Chitwan District, central Nepal. *Journal of Nepal Geological Society*, 65, 141–150.

Lennon M (2005). Recycling construction and demolition wastes: a guide for architects and contractors. *Commonwealth of Massachusetts*, Department of Environmental Protection, Boston, USA.

National Planning Commission (2015). Nepal Earthquake 2015 – Post Disaster Needs Assessment, Vol. B: Sector Reports. National Planning Commission, Government of Nepal. https://nepal.unfpa.org/sites/default/files/pub-pdf/PDNA_volume_BFinalVersion.pdf [accessed 27-10-2025].

Pacheco-Torgal F (2017). High tech startup creation for energy efficient built environment. *Renewable and Sustainable Energy Reviews*, 71, 618–629.

Parajuli HR (2012). Determination of mechanical properties of the Kathmandu World Heritage brick masonry buildings. *Proceedings of the 15th World Conference on Earthquake Engineering.* Lisbon, Portugal.

Parajuli RR, Furukawa A, Gautam D (2020). Experimental characterization of monumental brick masonry in Nepal. *Structures*, 28, 1314–1321.

Poudel R, Hirai Y, Asari M, Sakai S (2019). Field study of disaster waste management and disposal status of debris after Gorkha Earthquake in Kathmandu, Nepal. *Journal of Material Cycles and Waste Management*, 21, 753–765.

Poudel S, Subedi A, Khadka B, Poudel A, Adhikari B, Thapa BB, Gyawali TR (2025). Study on the mechanical properties of concrete with recycled aggregates, glass fibers, and fly ash: exploring environmental waste utilization. *Innovative Infrastructure Solutions*, 10, 377.

Şamdan F, Çelikyürek İ, Canbaz M (2024). Determination of waste crushed baked clay aggregate concrete with granular composite material preparations. *Challenge Journal of Concrete Research Letters*, 15(4), 112–119.

Shrestha S (2019). A case study of brick properties manufacture in Bhaktapur. *Journal of Science and Engineering*, 7, 27–33

Silva RV, de Brito J, Dhir RK (2014). Properties and composition of recycled aggregates from construction and demolition waste suitable for concrete production. *Construction and Building Materials*, 65, 201–217.

Subedi SK (2020). Study of characteristics of bricks produced in Kathmandu, Nepal. *American Journal of Civil Engineering*, 8, 64.

Thapaliya N, Karki N, Badu L, Karki R, Bagale U, Timalsina I, Ali Y, Thapa S, Bhatt MR (2024). Study on properties and uses of clay burnt bricks as a popular construction material: A case study of Bhaktapur, Nepal. *Proceedings of the 11th International Conference on Challenges in Earth-Based Interior Architecture; Current Issue in Earth-Based Materials, Construction Techniques and Approaches*, Kayseri, Turkey.

Xiao J, Li W, Fan Y, Huang X (2012). An overview of study on recycled aggregate concrete in China (1996–2011). *Construction and Building Materials*, 31, 364–383.

Challenge Journal of CONCRETE RESEARCH LETTERS

Research Article

Effects of maximum aggregate grain size and gradation on roller compacted concrete pavements

Ömer Faruk Keleş [a,*]

[a] *Department of Civil Engineering, Erzincan Binali Yıldırım University, 24100 Erzincan, Türkiye*

ABSTRACT

Roller compacted concrete (RCC) pavements, which stand out as an alternative to conventional concrete and asphalt pavements, are increasingly preferred because of their high strength, fast construction, and low cost advantages. The properties of aggregates directly affect the performance in roller compacted concrete mixtures. In particular, the maximum aggregate particle size (D_{max}) and gradation play a determining influence on the mixture's density, compressibility, and mechanical strength. This study aimed to investigate the effects of maximum aggregate particle size and gradation on the mechanical performance of roller compacted concrete pavement mixtures. Within this scope, roller compacted concrete pavement mixtures were produced using three D_{max} (12.5, 19, and 25 mm) and three different cement dosages (300, 350, and 400 kg). Tests for physical properties on mixtures were conducted using unit weight and ultrasonic pulse velocity (UPV) tests, while tests for mechanical properties were conducted using compressive strength, flexural strength, and splitting tensile strength tests. Increasing the D_{max} to 25 mm significantly improved the compressive and flexural strength of the mixtures. However, the splitting tensile strength increased up to 19 mm and showed a slight decrease when reaching 25 mm. The increase in cement content consistently improved all mechanical properties. Overall, the use of well-graded coarse aggregates with D_{max} in the range of 19–25 mm was found to improve the mechanical properties and compressibility of roller compacted concrete mixtures.

ARTICLE INFO

Article history:
Received – October 17, 2025
Revision requested – January 5, 2026
Revision received – January 22, 2026
Accepted – February 1, 2026

Keywords:
Roller compacted concrete pavement
Aggregate grain size
Mechanical properties
Ultrasonic pulse velocity

Citation: Keleş ÖF (2026). Effects of maximum aggregate grain size and gradation on roller compacted concrete pavements. *Challenge Journal of Concrete Research Letters*, 17(1), 57–70.

1. Introduction

In recent years, while concrete and asphalt pavement construction has shown significant development, producing durable and longer-lasting pavements has become an important aim (Maafi et al. 2025). Concrete pavements have a higher modulus of elasticity and stiffness than flexible pavements and are more economical in the long term, making them the preferred choice (Baş 2024). With the emergence of new materials and advances in construction technology, various types of pavements have emerged. The most notable of these are RCC pavements and have become a type of pavement which has been increasingly used in most countries in recent times (Ghahari et al. 2017; Tavakoli et al. 2021). RCC pavement is a rigid, zero-slump concrete that is often used in road pavements due to its rapid construction and lower cost effectiveness (ACI 325 2001, Rao et al. 2016a). The materials used in RCC pavement mixtures are similar to those in conventional concrete and contain the same components as traditional concrete (Keleş and Akpinar 2022; Çalış and Yıldızel 2019). RCC pavement construction has become an important alternative to traditional concrete and asphalt pavements due to its advantages of low cement content, rapid constructability, and low maintenance costs (Aghaeipour and

* *Corresponding author*. E-mail address: faruk.keles@erzincan.edu.tr (Ö. F. Keleş)
ISSN: 2548-0928 / DOI: https://doi.org/10.20528/cjcrl.2026.01.005

Madhkhan 2020). The recent preference for RCC pavements over other pavement types has attracted more interest and research from researchers. This situation has caused an increase in studies related to RCC pavements in recent times (Şermet et al. 2024; Armağan; et al. 2019; Sarı et al. 2025; Şengün 2024; Kılıç and Gök 2021).

The physical, mechanical, and durability characteristics of concrete are directly dependent on the design of the mixture and the specifications of the conventional or alternative aggregates used in this design. (Şengül et al. 2013). In this respect, many factors including the ingredients and aggregate characteristics govern concrete performance, and practical constraints such as the availability of local materials can limit the aggregate sources and gradations that can be used (Yıldızel 2023). Aggregates, which have many properties such as shape, roughness, specific gravity, chemical composition, and stability that are related to the characteristics of the parent soil, constitute approximately 75% of concrete and play an important role in its performance (Bulut 2024a). RCC pavements differ from traditional concrete in that they contain more aggregate and less cement (Keleş et al. 2024). This makes aggregate selection even more important for RCC pavements. The particle shape, surface structure, particle size distribution, and especially the Dmax of aggregates have a direct effect on the performance of concrete (Islam et al. 2018; Sağlam and Kılıç 2021). Dmax has a considerable impact on many important properties of both fresh and hardened concrete (Rao et al. 2016b; Meddah et al. 2011).

Studies using recycled, artificial, industrial by-product, and waste-based aggregates of different types and sizes instead of natural traditional aggregates in concrete or asphalt production are available in the literature (Bulut 2024b; Buritatum et al. 2022; Çolak et al. 2025; Bulut and Kandil 2025; Oreto et al. 2024). In many studies in recent years, the effects of maximum aggregate particle size on concrete have been investigated. Gora and Szafraniec (2020) examined the effects of maximum aggregate particle size on the strength properties and elastic modulus of concrete in their study. In this context, concrete specimens with Dmax values of 8, 16, and 31.5 mm were produced, and as Dmax increment, a significant decrease in splitting tensile strength and a slight increase in compressive strength were observed. Śliwiński and Duży (2020) investigated the effect of the ratio of the minimum size of cubic concrete specimens to the Dmax. It was found that the relationship between specimen size and Dmax had a noticeable effect on the representativeness of concrete specimens. Mahmoud et al. (2020) found that increasing the Dmax used in concrete reduces the mass attenuation coefficient. Siregar et al. (2017) investigated the effect of aggregate size distribution on the fracture behavior of concrete with high strength. It was determined that size distribution affects the level of ductility exhibited by concrete with high strength. Çelikten and Canbaz (2020) investigated the effect of aggregate particle size on the permeability properties of concrete. It has been determined that an increment in the aggregate particle size within mixtures causes a decrease in strength. Faramarzi and Rezaee (2018) examined the strength properties of concrete specimens according to changes in particle size. For this objective, concrete blocks with particle sizes of 12, 20, and 25 mm were produced. It was determined that an increase in aggregate size increases compressive strength. Furthermore, the results of the flexural tests showed that fracture toughness increased as the particle size changed from 12 mm to 20 mm, and decreased slightly when the particle size changed from 20 mm to 25 mm. Türkmenoğlu and Atahan (2020) focused on the impact of aggregate grain size distribution and PP fiber usage on plastic shrinkage cracking in concrete. It was determined that coarse aggregate grain size distribution is more effective in preventing cracking. Although many studies have been investigated regarding the impact of maximum aggregate grain size on conventional concrete, its effects on RCC have been studied very limitedly. Furthermore, the effect of Dmax on RCC pavements has almost not been investigated. Sağlam and Kılıç (2021) produced RCC mixtures with dosages of 300 kg and 350 kg, with Dmax of 12.5, 16, and 22.4 mm. In low cement dosage mixtures, the maximum compressive strength is observed using the largest aggregate size, while in high-cement mixtures, it is obtained with the smallest aggregate size. Rao et al. (2016b) investigated the effect of maximum aggregate sizes on RCC performance. It was reported that as aggregate size increased, strength increased but permeability properties deteriorated.

In this study, the effects of different Dmax on the physical and mechanical properties of RCC pavements were experimentally investigated. Unlike previous studies, RCC pavement mixtures with three different Dmax 12.5, 19, and 25 mm were produced according to the mixture design specified in ACPA (2014a). In addition to different aggregate particle sizes, the mixtures had three different cement contents: 300, 350, and 400 kg. Optimum water contents for maximum compactibility were determined for each mixture. The mechanical properties of RCC pavement mixtures with different particle sizes and cement dosages, including compressive, flexural, and splitting tensile strength, as well as their UPV and unit weight values, were measured and the test results have been correlated.

2. Materials and Experimental Program

2.1. Materials

In this study, crushed limestone aggregate has been used in according with ASTM C33 (2016) standard. To produce the mixtures, the maximum aggregate particle sizes specified by the American Concrete Pavement Association (ACPA 2014b) were considered and selected as 12.5 mm, 19 mm, and 25 mm. The aggregate particle size ranges were 0-5 mm, 5-12.5 mm, 12.5-19 mm, and 19-25 mm (Fig. 1). The properties of coarse and fine aggregates used in the study obtained in according with ASTM C127 (2016) and ASTM C128 (2016) standards are given in Table 1.

The sieve size ranges according to D_{max} (12.5, 19, and 25 mm) are given in Table 2. The gradation curves of the mixture aggregates created within the sieve size ranges

specified by the ACPA (2014b) are given in Fig. 2 according to the maximum aggregate particle sizes. Three different aggregate mixtures were prepared to produce RCC pavement mixtures. Mixture 1 had a maximum aggregate particle size of 12.5 mm, with aggregate particle size ranges of 0-5 mm and 5-12.5 mm. Mixture 2 had a maximum aggregate particle size of 19 mm, with aggregate particle size ranges of 0-5 mm, 5-12.5 mm, and 12.5-19 mm. Mixture 3 had a maximum aggregate particle size of 25 mm, with aggregate particle size ranges of 0-5 mm, 5-12.5 mm, 12.5-19 mm, and 19-25 mm.

In the study, CEM II 42.5 Portland cement was used according to the ASTM C150 (2011) standard. The properties of the cement used are given in Table 3. Three different cement dosages, 300 kg, 350 kg, and 400 kg, were used in the RCC mixtures. City supply water according to ASTM C1602 (2012) standard was used in the production of RCC pavement mixtures.

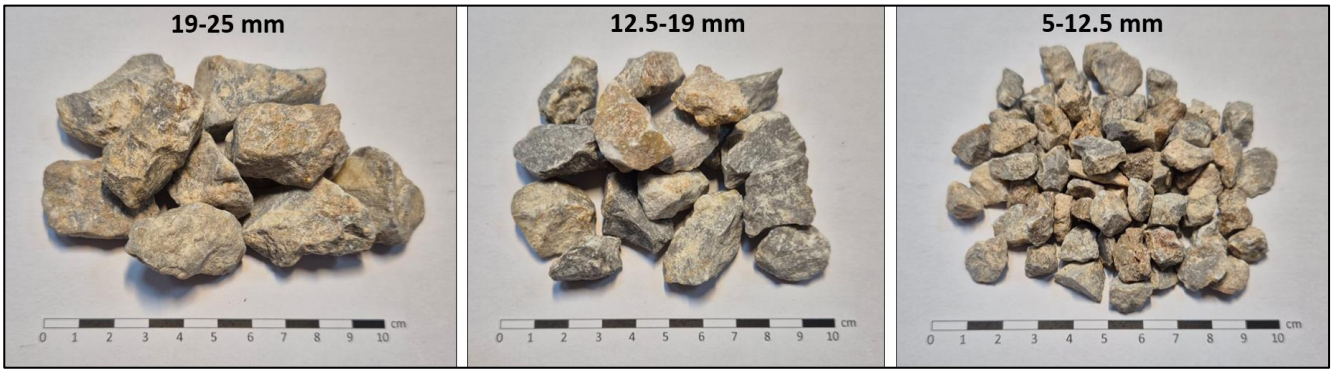

Fig. 1. Coarse aggregates used in RCC mixtures.

Table 1. Properties of coarse and fine aggregates used in RCC mixtures.

Physical properties	Fine aggregate (0–5 mm)	Coarse aggregate (5–12.5 mm)	Coarse aggregate (12.5–19 mm)	Coarse aggregate (19-25 mm)
Specific gravity (OD), gr/cm³	2.48	2.68	2.67	2.67
Specific gravity (SSD), gr/cm³	2.57	2.69	2.68	2.68
Apparent specific gravity, gr/cm³	2.71	2.72	2.69	2.70
Absorption, %	3.51	0.55	0.27	0.38

Table 2. Combined aggregate gradation ranges for RCC (ACPA 2014b).

Sieve size	Lower & Upper specification limits 12.5 mm		Lower & Upper specification limits 19 mm		Lower & Upper specification limits 25 mm	
37.5 mm	–	–	–	–	100	100
25 mm	–	–	100	100	82	100
19 mm	100	100	95	100	72	95
12.5 mm	81	100	70	95	61	81
9.5 mm	71	91	60	85	50	71
4.75 mm	49	70	40	60	36	55
2.36 mm	33	54	30	50	25	43
1.18 mm	24	40	20	40	15	32
600 µm	15	30	15	30	10	26
300µm	10	25	10	25	5	19
150 µm	2	16	2	16	2	16
75 µm	0	8	0	8	0	8

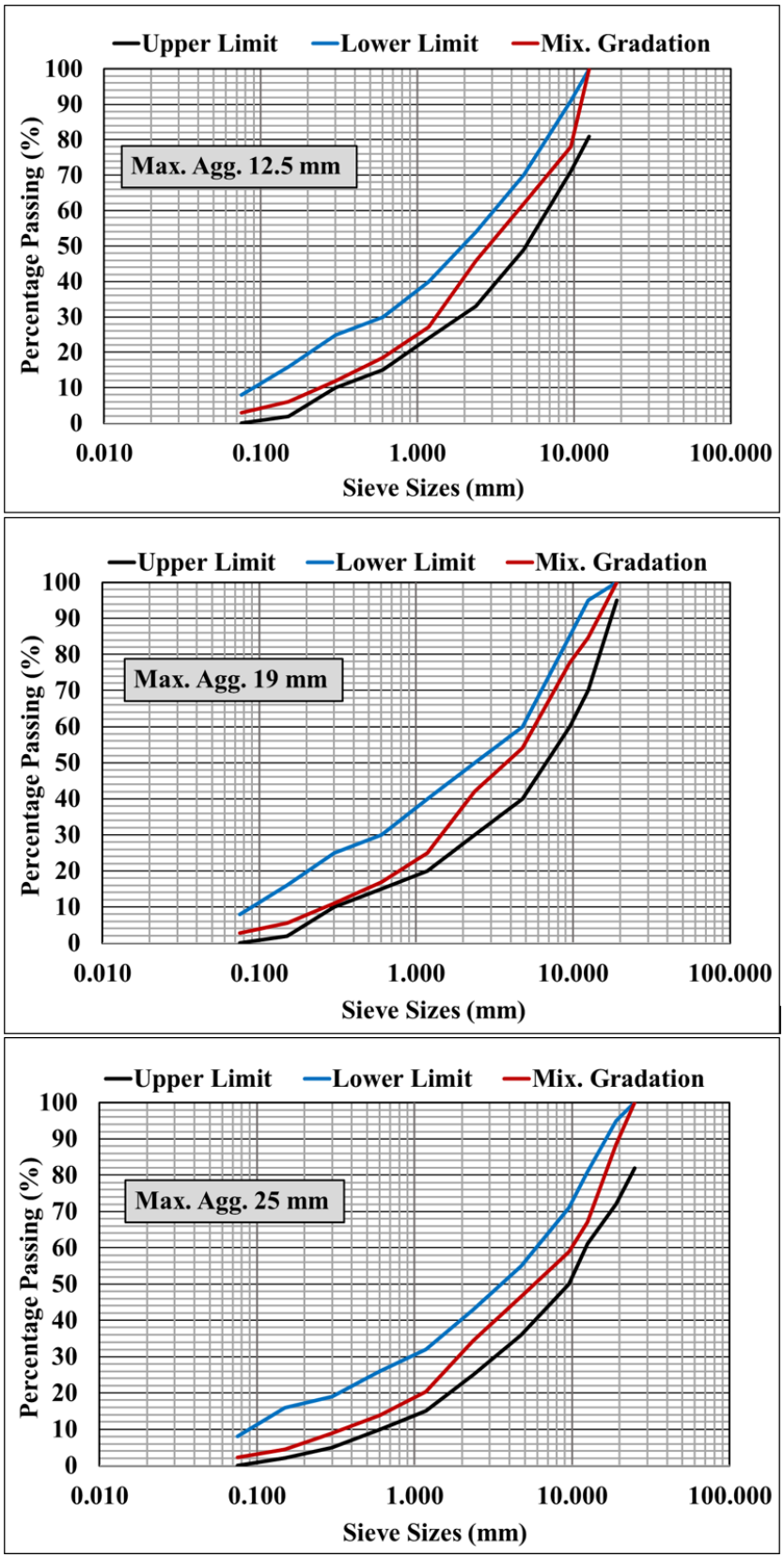

Fig. 2. Gradation curves of combined aggregate and standard limitations.

Table 3. Properties of cement used in RCC mixtures.

Component	SiO_2	Al_2O_3	Fe_2O_3	CaO	MgO	SO_3	Na_2O	K_2O	Cl
Amount (%)	18.5	4.5	3.6	63.3	1.2	2.9	0.3	0.7	0.014
Initial and final setting time (min)			145–215			28-day compressive strength (MPa)			45.82

2.2. Optimum moisture content and mix proportions

The consistency of RCC pavements is more important compared to conventional concrete pavements due to the presence of the compaction operation during production. Compaction is critical in obtaining maximum density in RCC pavements (Keleş et al. 2024). The relationship between moisture content, the parameter that most affects the compactibility of mixtures, and dry unit weight has been found by the Modified Proctor Test (ASTM D1557; 2012). The relationships between optimum moisture content and dry unit weight for mixtures with three different cement dosages are given in Fig. 3.

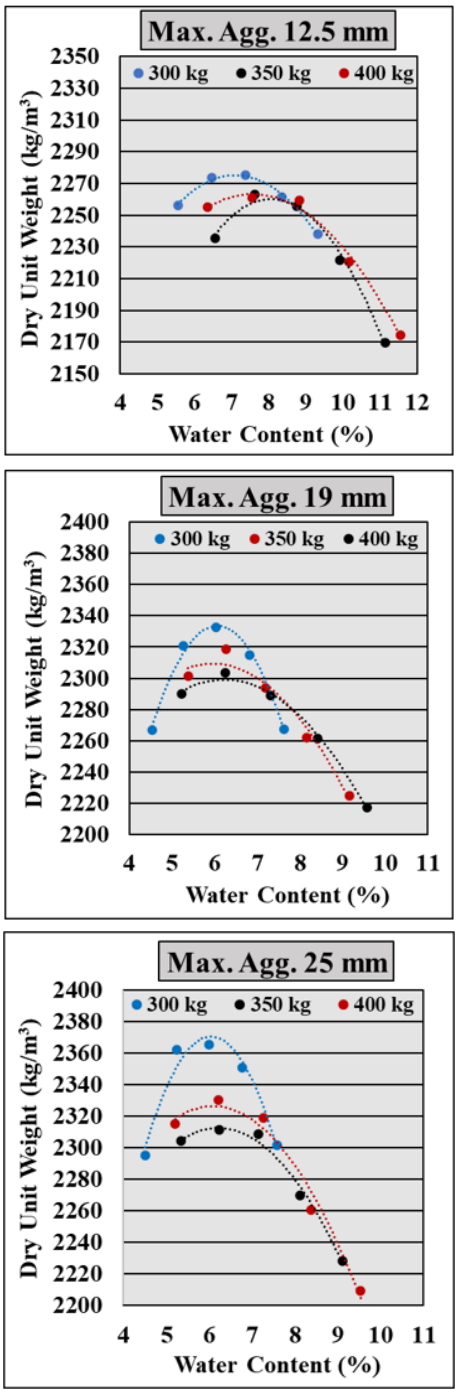

Fig. 3. The relationship between the dry unit weight and water content of RCC mixtures.

The water content and dry unit weight relationships of RCC mixtures were examined, and the water contents of the mixtures were determined by identifying the optimum moisture content corresponding to maximum density. Increasing the maximum aggregate particle size in the mixtures reduced the optimum moisture content corresponding to maximum density. As the particle size increased, the percentage of fine aggregate reduced, and the water absorption ratio of the mixes decreased. This revealed the need for less water for maximum compactibility. The material quantities required for 1 m^3 of RCC mixtures were calculated according to the water contents of the mixtures, and the mixture ratios are given in Table 4. The mixture codes in the table are expressed numerically. The first part of the codes represents the D_{max} (mm), and the second part represents the cement dosage (kg).

2.3. Sample preparation

A pan-type laboratory mixer was used to produce RCC mixtures. For each mixture, the aggregates and cement were first mixed until homogeneous, then mixing water was added and mixing was continued. Unlike conventional concrete, RCC has a very dry consistency, therefore requiring additional compaction during placement. To produce RCC mixtures in a laboratory environment, the compaction procedure specified in ASTM C1435 (2017) is applied. For this purpose, vibrating hammers and compaction plates meeting the specifications outlined in the standard were used. Cylinder specimens were produced for compressive and tensile strength, beam specimens for flexural strength, and cube specimens for unit weight. Circular compaction plates were used for cylinder specimens, rectangular plates for beam specimens, and square plates for cube specimens. The RCC specimens produced using vibrating hammer, compaction plates, and molds used in specimen production are shown in Fig. 4.

According to the standard, the compaction process of the specimens was carried out in three layers, with each layer not exceeding 20 seconds. The RCC samples were demolded 24 hours following casting and kept in a curing tank in according with the ASTM C192 (2015) standard until the test day, which was 28 days later.

Cross-sectional images of the RCC specimens produced in accordance with the standards are presented in Fig. 5 and were obtained by cutting and photographing the beam specimens using a standard scanner. The aggregate and mortar composition in the concrete was created by drawing the edges around each particle and then filling these outlines with white. In the images arranged in this way, the white color represents the aggregate, and the black color represents the mortar surfaces. In all specimens, the aggregate particles were observed to be homogeneously distributed, and no signs of component separation were found.

Table 4. Proportions of materials used in the production of RCC specimens.

Mix. code	Cement (kg)	Aggregate (kg)				W/C
		Fine aggregate (0–5 mm)	Coarse aggregate (5–12.5 mm)	Coarse aggregate (12.5–19 mm)	Coarse aggregate (19-25 mm)	
12.5–300	300	1132	815	–	–	0.43
19–300		1030	506	404	–	0.45
25–300		843	303	303	505	0.45
12.5–350	350	1081	778	–	–	0.42
19–350		1010	496	396	–	0.38
25–350		819	295	294	490	0.40
12.5–400	400	1067	798	–	–	0.35
19–400		978	480	383	–	0.35
25–400		805	290	289	481	0.34

Fig. 4. Vibrating hammer, tamping plates, molds and produced RCC samples.

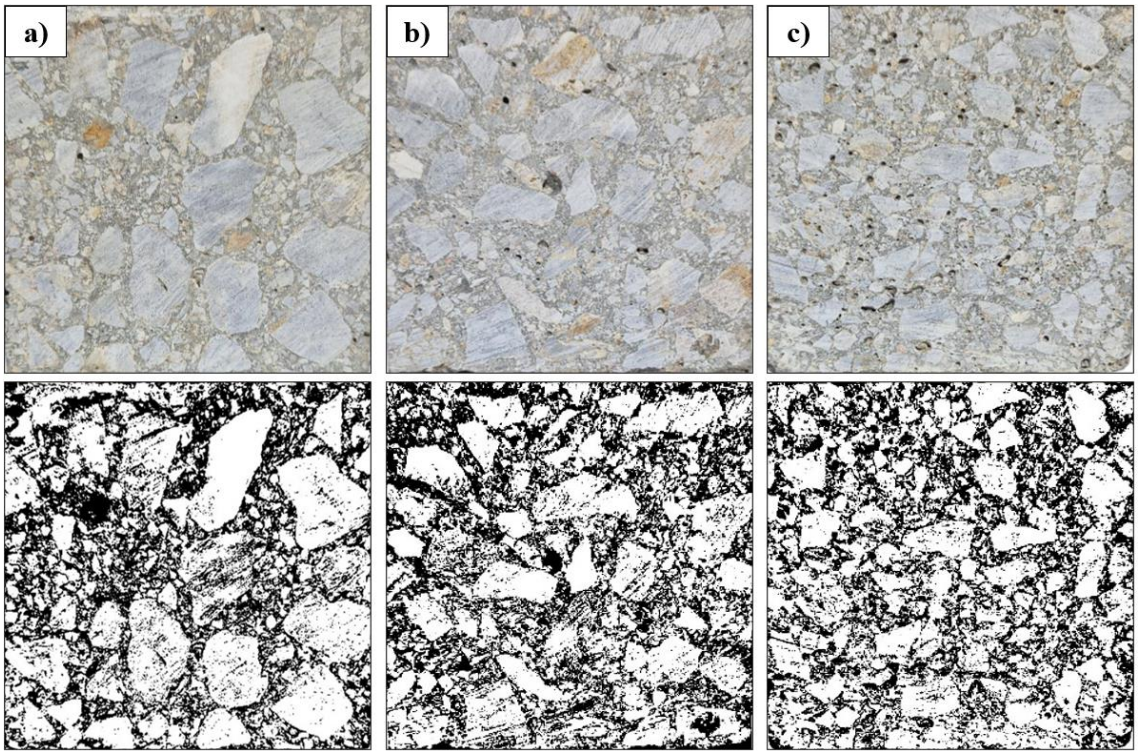

Fig. 5. Cross-sectional images of RCC samples: (a) D_{max}=25 mm; (b) D_{max}=19 mm; (c) D_{max}=12.5 mm.

2.4. Testing methods

This study evaluated the impact of maximum aggregate particle size on the certain physical and mechanical properties of RCC pavement mixtures. Within this scope, the fresh and hardened concrete unit weights, UPV values, and compressive, flexural, and splitting tensile strengths of the RCC samples were measured. The unit weights of RCC mixtures (fresh and hardened) were measured on 150x150x150 mm cube specimens according to ASTM C138 (2013) and ASTM C642 (2013) standards, respectively. The UPV test, one of the non-destructive testing methods, was applied to cylindrical, cube, and beam specimens measuring 150x300 mm, 150x150x150 mm, and 100x100x400 mm, respectively, before the tests, in accordance with the ASTM C597 (2009) standard. Compressive strength and tensile strength in flexure tests were applied to 150x300 mm cylindrical specimens in according with ASTM C39 (2014) and ASTM C496 (2017) standards, respectively, while the flexural strength test was applied to 100x100x400 mm beam specimens in accordance with ASTM C78 (2018) on beam specimens measuring 100x100x400 mm. Images of the tests performed on the RCC specimens are provided in Fig. 6. Three samples were subjected to testing in order to obtain results for each experiment.

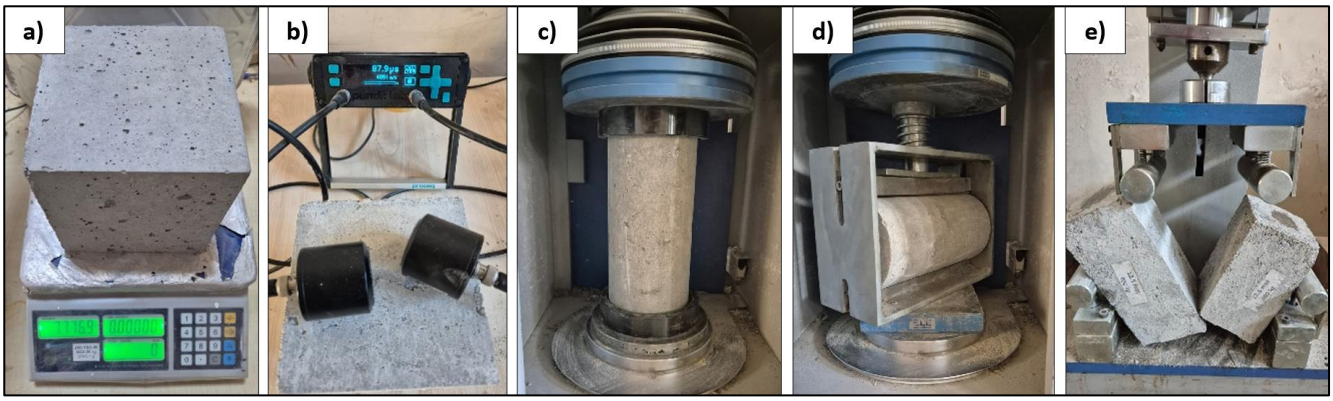

Fig. 6. RCC sample tests: (a) Unit weight; (b) UPV; (c) Compressive strength; (d) Splitting tensile strength; (e) Flexural strength.

3. Results and Discussion

3.1. Unit weight

The fresh and hardened unit weight results for RCC mixtures with different maximum aggregate sizes and gradations are presented in Table 5 and Fig. 7. When examining the unit weight results of the RCC mixtures, it was observed that both the fresh and hardened unit weights had close values. However, with the increment in the D_{max}, slight increases were observed in both unit weights.

Table 5. Unit weights of RCC samples.

Max. aggregate grain size	Cement dosage / Unit weight (kg/m³)					
	300 kg		350 kg		400 kg	
	Hardened	Fresh	Hardened	Fresh	Hardened	Fresh
12.5 mm	2380.19	2475.57	2344.33	2455.85	2344.30	2460.99
19 mm	2387.06	2478.65	2371.13	2479.51	2386.99	2473.24
25 mm	2397.37	2489.42	2395.55	2482.58	2392.80	2482.56

Considering the hardened unit weights, the lowest unit weight value was obtained in mixtures with a D_{max} of 12.5 mm and cement dosages of 350 kg and 400 kg, at approximately 2344 kg/m³. The highest unit weight was observed in mixtures with a maximum particle size of 12.5 mm and a dosage of 300 kg, at 2397 kg/m³. When the D_{max} changed from 12.5 mm to 25 mm at a dosage of 300 kg, the unit weight increased by approximately 1%. This increase was approximately 2% at cement dosages of 350 and 400 kg. Similarly, Çelikten and Canbaz (2020) observed an increase in unit weight with increment aggregate size in their study. Konitufe et al. (2023) used D_{max} of 14, 20, and 25 mm in their study and found the unit weights of the mixtures to be nearly identical.

3.2. Compressive strength

The uniaxial compressive strength test results for RCC mixtures are presented in Table 6 and Fig. 8. The results show that the compressive strength of the mixtures increases steadily with increasing maximum aggregate particle size and cement dosage. Increasing the aggregate particle size from 12.5 mm to 25 mm increased the compressive strength by approximately 23% in mix-

tures with a cement dosage of 300 kg. The increase in compressive strength in RCC mixtures with cement dosages of 350 and 400 kg continued at approximately 31% and 18%, respectively. Compressive strength test results have indicated that the use of aggregates up to 25 mm in size in RCC mixtures has steadily increased the strength of the mixtures, regardless of the cement dosage. In addition, the effect of cement dosage on the compressive strength of the mixtures was similar to the maximum aggregate particle size effect. Increasing the cement dosage in RCC mixtures from 300 kg to 400 kg provided strength increases of approximately 18%, 12%, and 13% for mixtures with maximum aggregate particle sizes of 12.5 mm, 19 mm, and 25 mm, respectively. The increase in cement dosage had a greater impact on the compressive strength test results of RRC mixtures with a 12.5 mm particle size compared to mixtures with 19 mm and 25 mm maximum particle sizes.

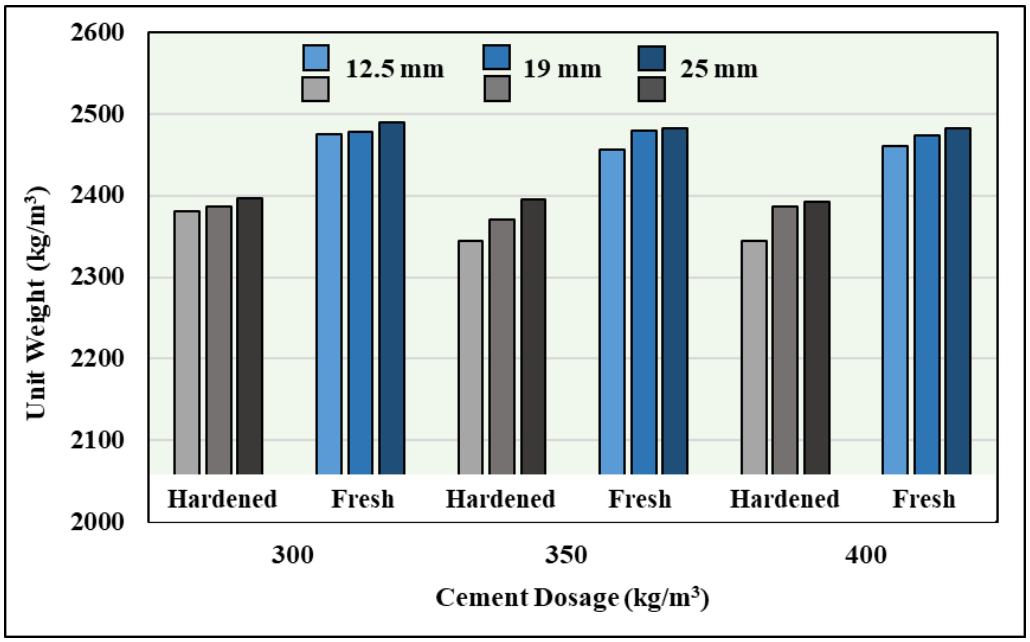

Fig. 7. Unit weights of RCC mixtures.

Table 6. Different strength test results of RCC mixture specimens.

Max. aggregate grain size	Parameter	Cement dosage (kg/m³)		
		300 kg	350 kg	400 kg
12.5 mm	Compressive strength (MPa)	41.57	41.77	48.90
19 mm		46.67	51.30	52.33
25 mm		51.07	56.13	57.65
12.5 mm	Flexural strength (MPa)	6.85	7.02	7.33
19 mm		6.87	7.07	7.62
25 mm		7.19	7.59	8.10
12.5 mm	Splitting tensile strength (MPa)	2.93	3.02	3.58
19 mm		3.43	3.47	3.75
25 mm		3.09	3.14	3.21

The results have indicated that the compressive strength test results of RCC mixtures made from aggregates of uniform size increases with increasing aggregate size. The compressive strength of RCC mixtures is largely dependent on the mechanical interlocking effect between aggregates. Increasing the D_{max} allows the aggregate skeleton to form a stronger and more rigid structure, transferring the load through aggregate-aggregate contacts. This increases the strength, particularly in RCC mixtures with low water/cement ratios, by reducing the stress concentration on the cement paste. Additionally, increasing the maximum aggregate particle size results in a better graded aggregate distribution. This facilitates better compaction of RCC mixtures, thereby reducing the void ratio and producing denser concrete, which further enhances strength. This effect is also supported by the increase in unit weights resulting from the larger particle size.

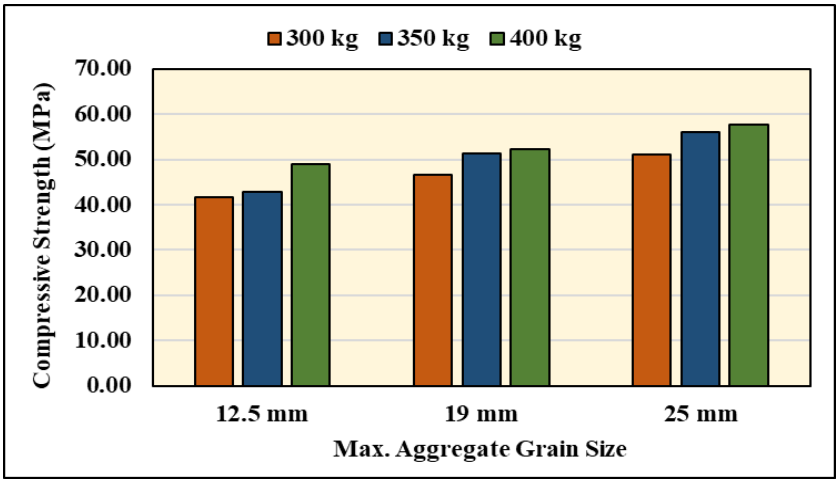

Fig. 8. Variation of compressive strength according to max. aggregate grain size.

Similar to the results of the current study, many studies have recorded increases in compressive strength with an increase in aggregate particle size. Faramarzi and Rezaee (2018), recorded increases in compressive strength with increasing aggregate particle size in their studies. A strength of 44.5 MPa was obtained in concrete mixtures with 12 mm aggregate size, while a compressive strength of 58.45 MPa was obtained in mixtures with 25 mm aggregate size. Góra and Szafraniec (2020), produced concrete mixtures with D_{max} of 8, 16, and 32 mm and obtained compressive strengths of 54.0 MPa, 54.7 MPa, and 56 MPa, respectively. Musa and Saim (2017) used two different aggregate particle sizes, 10 and 20 mm, in their studies. They determined compressive strengths of approximately 17 MPa and 39 MPa, respectively, achieving a significant strength increase of 128% with increasing particle size. In addition, Ajamu and Ige (2015) and Khan et al. (2021) were among other researchers who recorded an increase in compressive strength with an increase in D_{max}. Contrary to these studies, Konitufe et al. (2023) recorded a slight decrease in compressive strength, achieving approximately 28 MPa, 27 MPa, and 26 MPa in concrete mixtures with aggregate sizes of 14, 20, and 25 mm, respectively. Similarly, Woode et al. (2015) observed a decrease in strength with increasing maximum aggregate particle size in their studies. Together with other studies in the literature, the results showing the effect of D_{max} on compressive strength are summarized in Fig. 9.

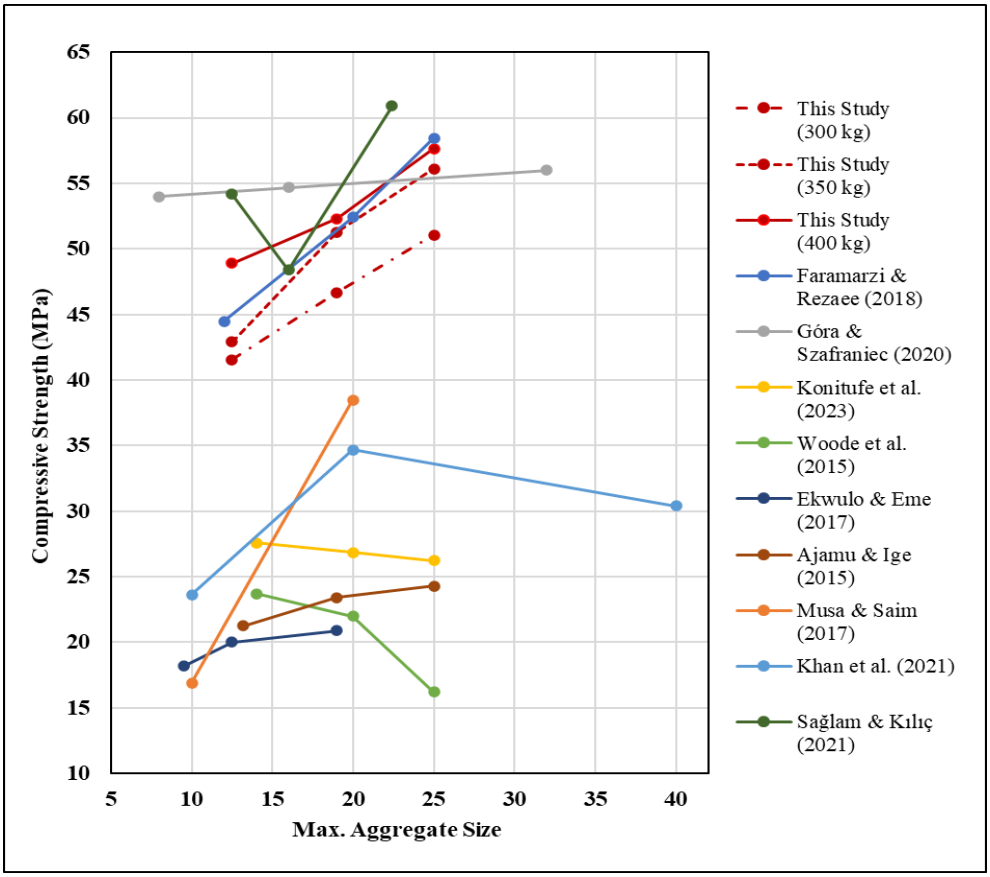

Fig. 9. The effect of D_{max} on compressive strength in different studies.

3.3. Flexural strength

The results of the four-point flexural strength test for RCC mixtures are presented in Table 4 and Fig. 10. The results have indicated that the flexural strength of the mixtures increased steadily with increasing cement dosage. The highest flexural strength was measured at 8.1 MPa in mixtures with a cement dosage of 400 kg and a maximum aggregate particle size of 25 mm. The lowest strength was measured at 6.85 MPa in specimens with a cement dosage of 300 kg and a particle size of 12.5 mm. Increment of the cement dosage in the mixtures from 300 kg to 400 kg increased the flexural strength of the samples with aggregate particle sizes of 12.5 mm, 19 mm, and 25 mm by approximately 7%, 13%, and 13%, respectively. The change in maximum aggregate particle size produced different results in flexural strength. The increase in maximum aggregate size from 12.5 mm to 19 mm produced an insignificant variation in flexural strength for the mixtures with 300 and 350 kg/m^3 cement dosage. Increasing the particle size from 19 mm to 25 mm in mixtures with the same dosages resulted in approximately 6% and 7% increases in flexural strength, respectively. In mixtures with a dosage of 400 kg, changing the particle size from 12.5 mm to 19 mm and then from 19 mm to 25 mm increased the flexural strength by 4% and 6%, respectively. The American Concrete Pavement Association (ACPA 2014a) has stated that the flexural strength of RCC pavements ranges between 3.5 and 7 MPa. The Technical Specifications for Concrete Pavements published by the General Directorate of Highways of Türkiye (KGM 2016) specifies a minimum flexural strength of 4.5 MPa for concrete pavements. The flexural strength results obtained show that all mixtures meet the minimum flexural strength requirements specified in the standards.

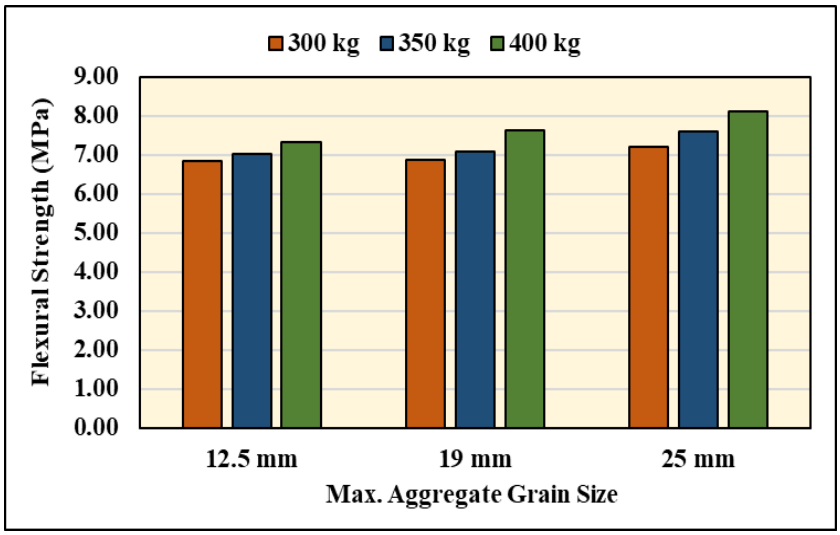

Fig. 10. Variation of flexural strength according to max. aggregate grain size.

The results showed that, similar to the compressive strength results, the flexural strength increased with the increment of the D_{max}. The increase in flexural strength can be described by the rigid structure formed by coarse aggregates limiting crack propagation and extending the crack path, thereby providing higher energy absorption under flexural loading. Furthermore, coarse aggregates reduced the mortar volume, decreasing the proportion of weak tensile zones and contributing to increased flexural strength. Furthermore, as the aggregate particle size increased, the load-bearing skeleton structure of the concrete became more rigid. Under bending, this rigid skeleton contributed to the homogeneous distribution of the load and the spreading of the bending moment over a wider area, thereby contributing to the increase in flexural strength.

Similarly, Sağlam and Kılıç (2021) reported an increase in flexural strength with an increment in maximum aggregate particle size. Flexural strength results of 7.6 MPa, 7.7 MPa, and 7.9 MPa were obtained for mixtures with maximum aggregate particle sizes of 12.5 mm, 16 mm, and 22.4 mm, respectively. The flexural strength of the samples supported the conclusion that bigger aggregate size resulted in better performance, which in turn resulting in higher flexural strength (Wei et al. 2020). On the contrary, there are also studies showing that flexural strength decreases as aggregate particle size increases. Ajamu and Ige (2015), and Ozioko (2015) used different maximum aggregate particle diameters in their studies and observed decreases in flexural strength with increasing particle size.

3.4. Splitting tensile strength

The splitting tensile strength test results for RCC mixtures are presented in Table 4 and Fig. 11. The results showed that the splitting tensile strength of the mixtures increased steadily with higher cement dosages. The highest splitting tensile strength was measured at 3.75 MPa in mixtures with a cement dosage of 400 kg and D_{max} of 19 mm. The lowest strength was measured at 2.93 MPa in samples with a cement dosage of 300 kg and a particle size of 12.5 mm. Increment the cement dosage in the mixtures from 300 kg to 400 kg increased

the splitting tensile strength of the specimens with aggregate particle sizes of 12.5 mm, 19 mm, and 25 mm by approximately 22%, 9%, and 4%, respectively. Cement dosage had shown the minimum effect in mixtures with D_{max} of 25 mm when compared to other aggregate sizes. Increment the D_{max} did not cause a continuous increase in splitting tensile strength, unlike in compressive and flexural strengths. The splitting tensile strengths of the mixtures increased when the particle size reached 19 mm and began to decrease when it reached 25 mm. This was observed in all cement-dosed mixtures. The splitting tensile strengths of mixtures with cement dosages of 300 kg, 350 kg, and 400 kg increased by 17%, 15%, and 5%, respectively, as the particle size changed from 12.5 mm to 19 mm. Conversely, as the particle size increased from 19 mm to 25 mm, the splitting tensile strength in the split test decreased by 10%, 9%, and 14%, respectively.

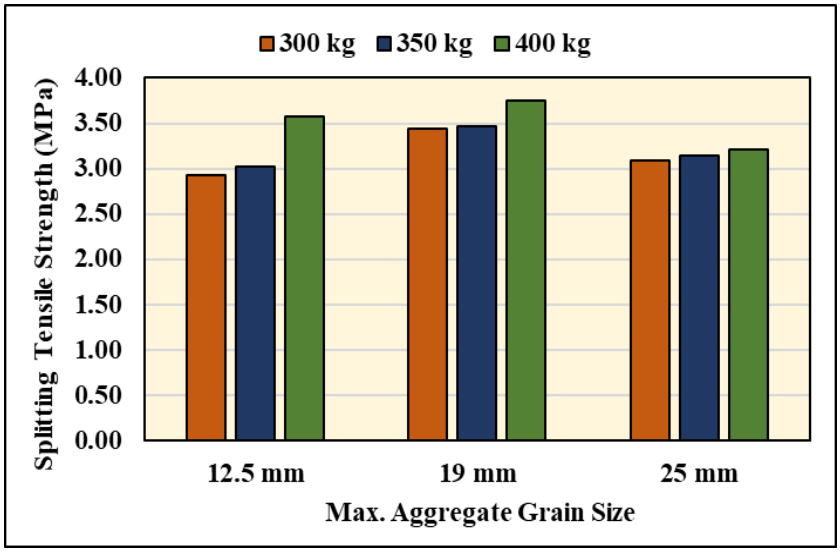

Fig. 11. Variation of splitting tensile strength according to max. aggregate grain size.

Similar to the results of this study, Wei et al. (2020) used aggregate particle sizes of 9.5 mm and 16 mm in concrete mixtures and obtained splitting tensile strengths of 2.18 MPa and 2.97 MPa, respectively. They determined that increasing the particle size resulted in an approximate 36% increase in strength. Góra and Szafraniec (2020), on the other hand, recorded a decrease in splitting tensile strength in the split test with an increase in D_{max}. They produced concrete mixtures with D_{max} of 8, 16, and 32 mm and obtained splitting tensile strengths in the split test of 5.0 MPa, 3.7 MPa, and 3.3 MPa, respectively.

3.5. Ultrasonic pulse velocity (UPV)

The UPV values of each mixture measured prior to strength tests on cylinder, cube, and beam specimens. The UPV test results for RCC specimens produced in different sizes and shapes are given in Fig. 12. UPV values increased as the D_{max} of the mixtures became larger, while these values decreased as the cement dosage amount also became higher. The best UPV values were measured at 4971 m/s, which were obtained from beam specimens with D_{max} of 25 mm and a cement dosage of 300 kg. The lowest UPV values were measured at 4451 m/s, obtained from cylinder specimens with D_{max} of 12.5 mm and a cement dosage of 400 kg. Considering cube specimens, the UPV values in RCC mixtures with cement dosages of 300 kg, 350 kg, and 400 kg increased by 4%, 3%, and 7%, respectively, as D_{max} increased from 12.5 mm to 25 mm. Considering all sample results, increasing the dosage from 300 kg to 350 kg and 400 kg caused a decrease in UPV values of approximately 1% and 2%, respectively. When evaluated in terms of sample sizes, differences in UPV values were observed despite having the same mixture. When cube, beam, and cylinder samples were compared, UPV values showed an average difference of 4%, with the highest UPV values obtained from beam samples. The UPV values of the beam specimens are followed by the cube and cylinder specimens, respectively. The UPV variability in samples of different sizes with the same mixture may be due to differences in the compaction method (Keleş and Akpinar 2022). Samples with smaller cross-sections were subjected to greater compression energy, resulting in a more void-free and dense mixture, leading to higher UPV values.

The results revealed that 85% of the RCC mixtures had UPV values exceeding 4500 m/s. The UPV values of the remaining 15% also stayed above 4000 m/s. Whitehurst (1951) evaluated the results as excellent, good, questionable, poor, and very poor in his UPV-based quality assessment method. In this method, UPV values indicate that the quality of concrete mixtures below 2000 m/s is very poor, those between 2000-3000 m/s are poor, those between 3000-3500 m/s are questionable, those between 3500-4500 m/s are good, and those above 4500 m/s are very good. According to this method, it is understood that all RCC mixtures produced were of at minimum good quality. Similar to the results in this study, Sağlam and Kılıç (2021) found that in their 300 kg and 350 kg dosage samples, the void ratio decreased and UPV values increased as D_{max} increased.

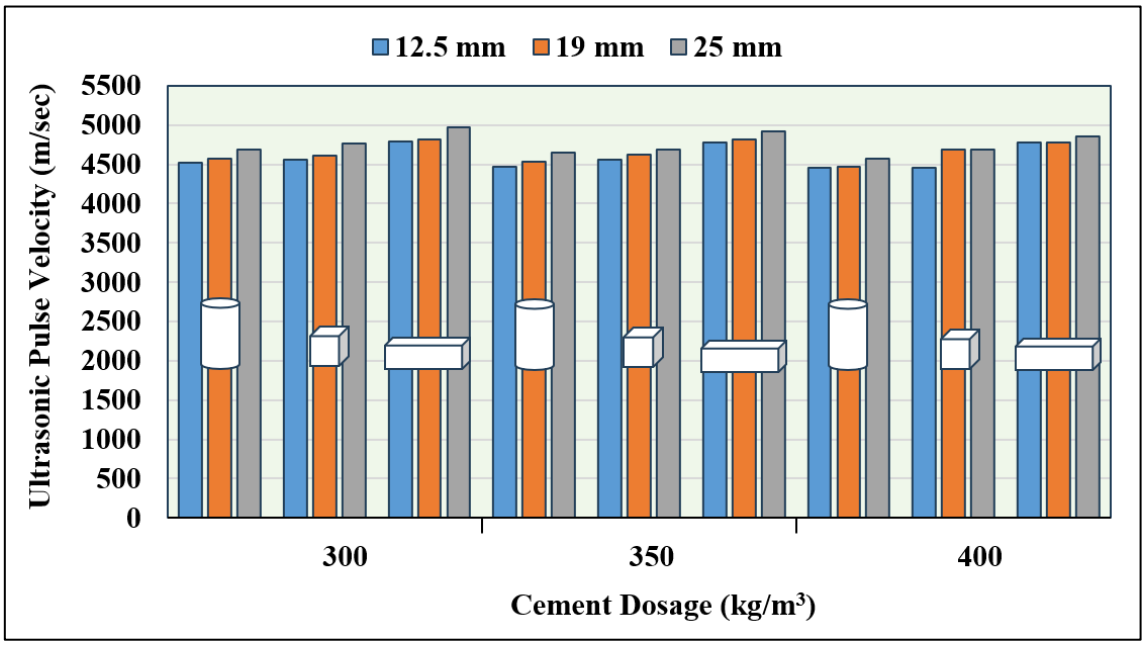

Fig. 12. UPV values of RCC cylinder, cube, and beam specimens.

4. Conclusions

This study investigated the effects of maximum aggregate particle size and gradation on the mechanical and physical properties of RCC pavement mixtures. In this regard, the findings obtained offer significant advantages in the design of RCC pavements in terms of both structural and construction aspects. Higher compressive and flexural strengths can be achieved with the suitable maximum aggregate particle size and gradation selection, while crack formation can be controlled by maintaining tensile strength through the optimum particle size. The high-density microstructure with a low void ratio enhances the durability and long-term performance of the pavement, while the limited variations in unit weight provide additional ease in placement and compaction during field applications. In these respects, the study demonstrates concrete engineering advantages for designing more reliable, durable, and predictable-performance mixtures in RCC pavements. The main findings obtained within the scope of the research are listed below.

- Maximum aggregate particle size and gradation had significant effects on the mechanical properties of RCC pavement mixtures. Increment the aggregate particle size from 12.5 mm to 25 mm resulted in significant increases in compressive and flexural strength. Up to 31% increase in compressive strength and up to 7% increase in flexural strength have been observed.
- Splitting tensile strength increased up to a maximum aggregate particle size of 19 mm, but decreased when reaching 25 mm. While the increase in strength reached up to 17%, decreases of up to 14% were observed with increasing particle size.
- An increment in cement dosage at all levels within the mixtures resulted in a consistent increase in all strength types. Increment of the cement dosage to 350 kg/m^3 resulted in average increases of approximately 8%, 4%, and 2% in compressive, flexural, and splitting tensile strength, respectively. Increment to 350 kg/m^3 resulted in increases of 14%, 11%, and 12%, respectively.
- UPV tests revealed that 85% of the mixtures had values above 4500 m/s and showed that the microstructure of the mixtures was dense and the void ratio was low. It has been determined that UPV values increase with an increment in the D_{max}, while they decrease with an increment in cement dosage.
- While both fresh and hardened unit weights of RCC mixtures have similar values, increment in maximum aggregate size has caused a slight increase in unit weights.

Acknowledgements
None declared.

Funding
The author received no financial support for the research, authorship, and/or publication of this manuscript.

Conflict of Interest
The author declares no potential conflicts of interest with respect to the research, authorship, and/or publication of this manuscript.

Data Availability
The datasets generated and/or analyzed during the current study are not publicly available but are available from the corresponding author upon reasonable request.

AI Assistance
No AI-based tools were used in the preparation of this manuscript.

Author Contributions
The author declares sole responsibility for all aspects of the study, including conceptualization, methodology, formal analysis, investigation, data curation, visualization, writing of the original draft, and writing, review, and editing of the manuscript.

REFERENCES

ACI 325.10R-95 (2001). Report on Roller-Compacted Concrete Pavements. American Concrete Institute, Farmington Hills, MI, USA.

ACPA (2014a). Guide Specification, Roller-Compacted Concrete Pavements, American Concrete Pavement Association, Skokie, IL, USA.

ACPA (2014b). Roller-Compacted Concrete Guide Specification. American Concrete Pavement Association, Skokie, IL, USA.

Aghaeipour A, Madhkhan M (2020). Mechanical properties and durability of roller compacted concrete pavement (RCCP). *Road Materials and Pavement Design*, 21(7), 1775-1798.

Ajamu SO, Ige JA (2015). Effect of coarse aggregate size on the compressive strength and the flexural strength of concrete beam. *International Journal of Engineering Research and Applications,* 5(1), 67-75.

Armağan K, Yıldızel SA, Arslan Y (2019). Steel scrap added roller compacted concrete. *Challenge Journal of Concrete Research Letters*, 10(1), 7-12.

ASTM C33 (2016). Standard Specification for Concrete Aggregates. American Society for Testing and Material, West Conshohocken, PA, USA.

ASTM C39 (2014). Standard Test Method for Compressive Strength of Cylindrical Concrete Specimens, American Society for Testing and Materials, West Conshohocken, PA, USA.

ASTM C78 (2018). Standard test method for flexural strength of concrete (using simple beam with third-point loading), American Society for Testing and Materials, West Conshohocken, PA, USA.

ASTM C127 (2016). Standard Test Method for Relative Density (Specific Gravity) and Absorption of Coarse Aggregate, American Society for Testing and Material, West Conshohocken, PA, USA.

ASTM C128 (2016). Standard Test Method for Relative Density (Specific Gravity) and Absorption of Fine Aggregate, American Society for Testing and Material, West Conshohocken, PA, USA.

ASTM C138 (2013). Standard Test Method for Density (Unit Weight), Yield, and Air Content (Gravimetric) of Concrete, American Society for Testing and Materials, West Conshohocken, PA, USA.

ASTM C150/C150M (2011). Standard Specification for Portland Cement, American Society for Testing and Material, West Conshohocken, PA, USA.

ASTM C192 (2015). Standard Practice for Making and Curing Concrete Test Specimens in the Laboratory, American Society for Testing and Materials, West Conshohocken, PA, USA.

ASTM C496 (2017). Standard Test Method for Splitting Tensile Strength of Cylindrical Concrete Specimens, American Society for Testing and Materials, West Conshohocken, PA, USA.

ASTM C597 (2009). Standard Test Method for Pulse Velocity through Concrete, American Society for Testing and Materials, West Conshohocken, PA, USA.

ASTM C642 (2013). Standard Test Method for Density, Absorption, and Voids in Hardened Concrete, American Society for Testing and Materials, West Conshohocken, PA, USA.

ASTM C1435 (2017). Standard Practice for Molding Roller-Compacted Concrete in Cylinder Molds Using a Vibrating Hammer, American Society for Testing and Materials, West Conshohocken, PA, USA.

ASTM C1602 (2012). Standard Specification for Mixing Water Used in the Production of Hydraulic Cement Concrete, American Society for Testing and Material, PA, USA.

ASTM D1557 (2012). Standard Test Methods for Laboratory Compaction Characteristics of Soil Using Modified Effort, American Society for Testing and Materials, West Conshohocken, PA, USA.

Baş Fİ (2025). Investigating the effects of glass fiber in enhancing concrete pavement performance. *Challenge Journal of Structural Mechanics*, 11(1), 42-54.

Buritatum A, Suddeepong A, Horpibulsuk S, Akkharawongwhatthana K, Yaowarat T, Hoy M, Bunsong C, Arulrajah A (2022). Improved performance of asphalt concretes using bottom ash as an alternative aggregate. *Sustainability*, 14(12), 7033.

Bulut HA (2024a). Examination of mechanical, permeability, and durability properties of sustainable lightweight concrete composites with natural perlite aggregate. *Iranian Journal of Science and Technology, Transactions of Civil Engineering*, 48, 1329–1352.

Bulut HA (2024b). A different approach for green concrete production: Determination of the effect of e-waste and waste rubber powder on durability properties of concrete. *Challenge Journal of Concrete Research Letters*, 15(3), 69-81.

Bulut HA, Kandil U (2025). Investigation of freeze-thaw performance for sustainable rubberized concrete composites with different water to cement ratios. *Materiales De Construcción,* 75(357), e364.

Çalış G, Yıldızel SA (2019). Investigation of roller compacted concrete: Literature review. *Challenge Journal of Concrete Research Letters*, 10(3), 63-74.

Çelikten S, Canbaz M (2020). Agrega tane boyutunun ve bağlayıcı türünün geçirimli beton özeliklerine etkisi. *Eskişehir Teknik Üniversitesi Bilim ve Teknoloji Dergisi B-Teorik Bilimler,* 8(2), 171-181. (in Turkish)

Çolak MA, Keleş ÖF, Baş Fİ, Demiriz AO (2025). Fracture behavior of warm mix asphalt mixtures incorporating Cecabase and recycled concrete aggregate: An experimental and numerical assessment. *Construction and Building Materials,* 492, 142939.

Faramarzi L, Rezaee H (2018). Testing the effects of sample and grain sizes on mechanical properties of concrete. *Journal of Materials in Civil Engineering,* 30(5), 04018065.

Ghahari SA, Mohammadi A, Ramezanianpour AA (2017). Performance assessment of natural pozzolan roller compacted concrete pavements. *Case Studies in Construction Materials*, 7, 82–90.

Góra J, Szafraniec M (2020). Influence of maximum aggregate grain size on the strength properties and modulus of elasticity of concrete. *Applied Sciences*, 10(11), 3918.

Islam MS, Azad MAK, Sarker AR (2018). Standardization the effect of shape of aggregates with respect to compressive strength of concrete. *Concrete Research Letters*, 9(1), 1-9.

Keleş ÖF, Akpinar, MV (2022). Strength properties of roller compacted concrete pavement (RCCP) under different curing methods. *Construction and Building Materials*, *324*, 126530.

Keleş ÖF, Bayrak OÜ, Bayata HF (2024). Experimental investigation on mechanical properties of sustainable roller compacted concrete pavement (RCCP) containing waste rubbers as alternative aggregates. *Construction and Building Materials*, 424, 135930.

KGM (2016). KGM-ARGE-17-02, Beton Yol Kaplamaları Teknik Şartnamesi (Technical Specification for Concrete Pavement), Research and Development Department, General Directorate of Highways, Ankara, Türkiye. (in Turkish)

Khan TF, Bashir K, Dar MS, Rather HA, Shahzad EI, Bhat ES, Tahir ES, Masoodi ES (2021). Effects of aggregate size on the concrete strength. *International Journal for Research in Applied Science & Engineering Technology,* 9(10), 695-700.

Kılıç İ, Gök SG (2021). Silindirle sıkıştırılmış atık beton agregasının silindirle sıkıştırılmış beton üretiminde yeniden değerlendirilmesi. *Bitlis Eren Üniversitesi Fen Bilimleri Dergisi*, 10(3), 999-1008. (in Turkish)

Konitufe C, Abubakar A, Baba AS (2023). Influence of aggregate size and shape on the compressive strength of concrete. *Construction*, 3(1), 15-22.

Maafi N, Benouadah A, Benammar A, Kessal O, Belkadi AA, Beddar M (2025). The effects of polypropylene fibers on the mechanical and durability performance of a roller compacted concrete for pavement. *International Journal of Pavement Research and Technology*, 18(1), 67-77.

Mahmoud KA, Tashlykov O, El Wakil AF, El Aassy IE (2020). Aggregates grain size and press rate dependence of the shielding parameters for some concretes. *Progress in Nuclear Energy,* 118, 103092.

Meddah MS, Suzuki M, Sato R (2011). Influence of a combination of expansive and shrinkage-reducing admixture on autogenous deformation and self-stress of silica fume high-performance concrete. *Construction and Building Materials*, 25(1), 239-250.

Musa MF, Bin Saim AA (2017). The effect of aggregate size on the strength of concrete. *The Colloquium,* 10, 9-11.

Oreto C, Russo F, Dell'Acqua G, Veropalumbo R (2024). A comparative environmental life cycle assessment of road asphalt pavement solutions made up of artificial aggregates. *Science of the Total Environment*, *927*, 171716.

Ozioko HO (2015). Effects of coarse aggregate sizes on the flexural strength of concrete. *Umudike Journal of Engineering and Technology*, 1(2), 1-6.

Rao SK, Sravana P, Rao TC (2016a). Experimental studies in Ultrasonic Pulse Velocity of roller compacted concrete pavement containing fly ash and M-sand. *International Journal of Pavement Research and Technology*, 9(4), 289-301.

Rao M, Yang H, Lin Y, Li J, Shi Y (2016b). Influence of maximum aggregate sizes on the performance of RCC. *Construction and Building Materials*, 115, 42-47.

Sağlam B, Kılıç İ (2021). Silindirle sıkıştırılmış betonlarda maksimum agrega tane çapının dayanım özelliklerine etkisi. *Kirklareli University Journal of Engineering and Science*, 7(2), 257-271. (in Turkish)

Sarı FA, Öztürk İŞ, Gönen T, Emiroğlu M (2025). Evaluation of waste metallic powder as fine aggregate replacement in Roller compacted concrete: Impact on physical and mechanical properties. *Construction and Building Materials,* 468, 140386.

Sengul O, Sengul C, Keskin G, Akkaya Y, Tasdemir C, Tasdemir MA (2013). Fracture and microstructural studies on normal and high strength concretes with different types of aggregates. *Proceedings of the 8th International Conference on Fracture Mechanics of Concrete and Concrete Structures*, Toledo, Spain, 714–725.

Siregar APN, Rafiq MI, Mulheron M (2017). Experimental investigation of the effects of aggregate size distribution on the fracture behaviour of high strength concrete. *Construction and Building Materials,* 150, 252-259.

Śliwiński J, Duży P (2020). Impact of sample size and maximum aggregate grain on the representativeness of concrete samples. *Energies*, 13(13), 3358.

Şengün E (2024). Mekanistik-ampirik tasarım yaklaşımıyla silindirle sıkıştırılmış beton yol performans değerlendirmesi: Ankara Temelli yolu örneği. *Black Sea Journal of Engineering and Science*, 7(6), 1155-1162. (in Turkish)

Şermet F, Kartal ME, Yiğit ME, Hökelekli E (2024). The effect of the gravity on the earthquake performance of roller compacted concrete dams. *Challenge Journal of Concrete Research Letters*, 15(1), 20-29.

Tavakoli D, Fakharian P, De Brito J (2021). Mechanical properties of roller-compacted concrete pavement containing recycled brick aggregates and silica fume. *Road Materials and Pavement Design*, 23(8), 1793–1814.

Türkmenoğlu HN, Atahan HN (2022). Agrega Tane boyut dağılımı ve PP lif kullanımının betonda plastik rötre çatlağı oluşumu üzerine etkileri. *Dicle University Journal of Engineering*, 13(3), 611-618. (in Turkish)

Wei H, Liu Y, Wu T, Liu X (2020). Effect of aggregate size on strength characteristics of high strength lightweight concrete. *Materials,* 13(6), 1314.

Whitehurst EA (1951). Soniscope tests concrete structures. *Journal Proceedings*, 47(2), 433-444.

Woode A, Amoah DK, Aguba IA, Ballow P (2015). The effect of maximum coarse aggregate size on the compressive strength of concrete produced in Ghana. *Civil and Environmental Research*, 7(5), 7-12.

Yıldızel S (2023). Mechanical, durability and solar reflectance properties of colored self–compacting concrete. *Challenge Journal of Concrete Research Letters*, 14(3), 89-95.

Challenge Journal of CONCRETE RESEARCH LETTERS

Research Article

Utilization of fly dust generated during fired shale production for the preparation of aggregates and geopolymers

Jan Urbánek [a,*], Petr Antoš [b]

[a] *Technopark Kralupy, University of Chemistry and Technology Prague, 27801 Kralupy nad Vltavou, Czechia*

ABSTRACT

Fly shale dust (FSD) is a fine secondary powder that is produced during the firing of shales in a rotary kiln. Its use is relatively limited, and therefore it is usually landfilled, despite its chemical composition being similar to chamotte. The main challenge is the wide firing temperature range. As a result, the material partially retains plastic properties and at the same time contains high-temperature phases. The second challenge is the significant fineness of the material, which makes it impossible to burn it in a rotary kiln. To evaluate its suitability, FSD powder was granulated with water and subsequently fired at temperatures ranging from 800 °C to 1650 °C to produce a refractory aggregate. Analysis of the high-temperature product confirmed a high mullite content and low porosity, as well as high refractoriness, which was further improved by the addition of alumina. The next part of the work was focused on the use of FSD for metakaolin production, where granulated material was calcined at 600-850 °C. The sample with the highest pozzolanic activity was selected for geopolymer preparation. Potassium or sodium water glass was used as the activator, blast furnace slag or cement as the hardener, and chamotte aggregate as the filler. The obtained material reached the compressive strength of concrete class C60/75. The results provided important information about the key steps of FSD processing and confirmed its potential for practical application.

ARTICLE INFO

Article history:
Received – November 7, 2025
Revision requested – December 24, 2025
Revision received – January 26, 2026
Accepted – February 1, 2026

Keywords:
Fly dust
Shale
Clay
Aggregate
Geopolymer

Citation: Urbánek J, Antoš P (2026). Utilization of fly dust generated during fired shale production for the preparation of aggregates and geopolymers. *Challenge Journal of Concrete Research Letters*, 17(1), 71–81.

1. Introduction

Formerly, chamber furnaces and charcoal piles were used for fireclay production. These technologies are now considered inadequate and have been displaced by the rotary kiln (Boateng 2008). Among the main advantages of rotary kilns are the possibility of automation, uniform continuous firing, and material processing in a wide range of fractions, high feed capacity and high operational temperatures (Bojanovský et al. 2022). During firing, flue gases are produced, which are blown out of the furnace by a connected fan. Blowing out also provides a slight underpressure in the furnace, which is critical for its safe and stable conditions (Zheng et al. 2022). Along with the flue gases, fine fly clay dust is carried away from the furnace and subsequently captured on collectors (Abdelgader et al. 2022). Due to the extremely high temperatures in the rotary kiln and the low temperature resistance of the filter material (up to 250 °C), the output mixture must be quickly cooled, for example, by using an auxiliary fan or a heat exchanger. At the same time, a multi-stage thermal filter protection system is used. The last protection is a short-term bypass switch directly to the fan. The obtained fly clay dust is characterized by high fineness and non-uniform properties. Its utilization is typically very limited. Therefore, it is usually landfilled. The production of aggregates, fillers and binders represents one of the potential methods for its effective reuse (Özkılıç et al. 2023; Lam et al. 2021; Jala and Sharma 2019; Riaz et al. 2022;

* *Corresponding author*. E-mail address: urbanekj@vscht.cz (J. Urbánek)
ISSN: 2548-0928 / DOI: https://doi.org/10.20528/cjcrl.2026.01.006

Padmalosan et al. 2023; Kaminskas and Savickaite 2023; Saleh et al. 2021).

Shale is a laminated or fissile claystone (Sheng 2020). It is a sedimentary rock formed by the settling of clay particles with a moderately consolidated layered structure with a particle size below 63 μm (Rimstidt et al. 2017; Muhammed et al. 2021). Shales consist mainly of clay minerals, predominantly kaolinite and also contain quartz, feldspar, iron oxides, carbonates, coal etc. (Aird 2019). They are processed by firing at temperatures of approximately 1350 °C to form refractory fireclay (Djangang et al. 2008). Fired shales are characterized by volume stability and good resistance to thermal shock. They are used in power generation blast furnaces, chimney linings, boilers, glass tank furnaces and pottery kilns (Debnath et al. 2022). The quality of fireclay is evaluated based on the amount of mullite and its degree of densification (Malaiškiene et al. 2022).

Due to its high kaolinite content, shale can also be used for the production of metakaolin. Metakaolin is an amorphous aluminosilicate that is a highly reactive natural pozzolan produced by the calcination and dehydroxylation of kaolinitic clay at temperatures between 500 °C and 900 °C (Panesar 2019; Provis and Bernal 2014). Depending on the origin of the raw materials, the chemical composition might vary (Bucher et al. 2021). Metakaolin is used as a cement replacement in concrete, leading to improved durability and a reduced environmental impact associated with the cement industry (Rasekh et al. 2020; Pillay et al. 2021). Metakaolin is rather expensive (Lopes et al. 2023) and therefore its production remains limited. Another application of metakaolin is as a precursor for geopolymer production (Aziz et al. 2015). The process involves the dissolution of the aluminosilicate source material in an alkaline solution (alkaline activator) to form aluminate-silicate hydrates, followed by a condensation reaction and subsequent hardening. Geopolymers exhibit excellent mechanical properties, durability, acid resistance and high temperature stability (Cong and Cheng 2021).

The aim of this study is to evaluate the reuse potential and application possibilities of fine fly shale dust (FSD) in construction materials. The work investigates the large-scale thermal treatment of powdered FSD, including firing to produce refractory aggregate and calcination to obtain reactive metakaolin. Key properties affecting applicability, such as refractoriness and pozzolanic activity, are evaluated. In the case of metakaolin, geopolymer binders are prepared and their mechanical properties are compared with literature data. In contrast to most previous studies, which focus on a single utilisation route, this work demonstrates a dual, construction-oriented valorisation of FSD using industrially applicable processes, including granulation, drying, firing, and grinding, which are commonly available in facilities engaged in clay processing and firing.

2. Materials and Methods

The fine fly shale dust (FSD) was obtained from České lupkové závody, a company specializing in the mining, firing and granulometric processing of refractory clays. The powder contained particles in the size range of 0-500 μm, with d_{60} being 31 μm and d_{90} being 123 μm. It contained a large amount of Al_2O_3 and a relatively low proportion of melting oxides (Table 1). The chemical composition may vary depending on the deposit location; for example, the Fe2O3 content ranges from 1.25% to 3.8%. A similar situation is observed for the mineralogical composition, which is additionally influenced by the firing temperature. Of the crystalline phases, it contained kaolinite, mica in the form of muscovite, quartz, anatase and high-temperature phases mullite and cristobalite (Table 2). Considering the relatively high proportion of mullite, it is clear that part of the material was exposed to high temperatures above 1050 °C. Furthermore, spherical ash particles were registered. They originate from powdered coal, which is used to heat the rotary kiln. SEM/EDS analysis showed that the chemical composition of individual particles varies in the content of minor fluxing oxides (K_2O, CaO, Fe_2O_3), particularly among spherical ash particles. In order to understand the processes during the firing, a thermal analysis of the FSD was carried out.

Table 1. Chemical composition of raw materials. (The contents are given in weight percent, normalized to 100%.)

Title	Al_2O_3	SiO_2	Fe_2O_3	TiO_2	Na_2O	K_2O	CaO	MgO
FSD	44.15	48.26	2.11	2.29	0.21	0.88	0.83	0.33
Kaolin	43.31	53.18	0.64	1.00	0.07	1.32	0.07	0.15
Alumina	99.35	0.18	0.05	–	0.15	0.05	0.02	0.13

Table 2. Mineralogical composition of FSD. (The contents are semiquantitative and expressed in weight percent, normalized to 100%. The sample contains a significant amount of amorphous phase.)

Title	Kaolinite	Mullite	Muscovite	Quartz	Anatase	Cristobalite
FSD	41	30	17	8	2	2

In the experimental work, the possibilities of using a commercial sample of FSD for the production of refractory aggregates were tested. The FSD was first mixed and homogenized with water in a ratio of 4:1 and granulated using an extruder equipped with a mesh adapter with an outlet mesh diameter of 9 mm (Fig. 1). The granules were dried at 110 °C to a constant weight and after cooling, were sieved manually using sieves 1.25, 2.5, 5.0, 7.1 and 10 mm. The 7.1-10 mm fraction was used for further analyses.

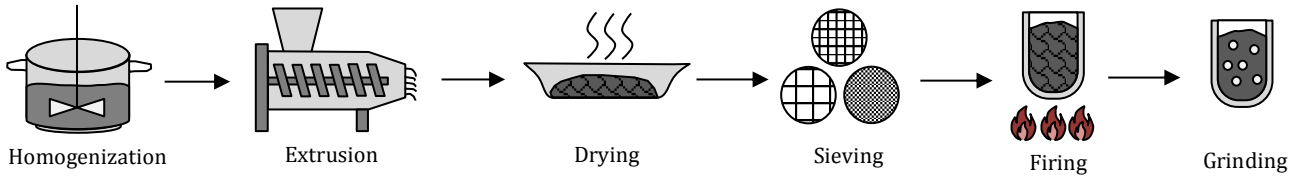

Fig. 1. Process scheme.

80-100 g of granulate was placed into a corundum crucible, which was fired in an electric furnace at temperatures of 800, 1150, 1250, 1350, 1450, 1550 and 1650 °C. Heating was performed at 5 °C/min, with a 3 h dwell time, followed by free cooling. Based on the weight loss, the loss on ignition was determined. The density criteria (bulk density, apparent porosity, absorbency) were determined by soaking the granules under vacuum in water. The soaking procedure was based on the EN 993-1 (2018) standard, while the granules were weighed on a steel sieve under water. Part of the fired granules was ground in a planetary mill. The resulting powder was used for analysis of phase composition using X-ray diffraction and particle morphology using electron microscopy. To increase the strength of the granules after drying, the effect of the addition of kaolin was tested. Furthermore, to increase the refractory properties, the influence of the addition of alumina (FEPA size: F-1200) was tested. The composition of the mixtures is shown in Table 3. With regard to the different absorbency of the individual components, the amount of added water was adjusted so that the mixtures exhibited similar plasticity after mixing.

Table 3. Composition of mixtures for granulate production.

Title	Content (%)			
	FSD	Kaolin	Alumina	Water
R	100	-	-	25
RK	80	20	-	28
RA	67	-	33	23

The chemical composition of the raw materials is given in Table 1. Rods from all three mixtures were prepared by manual tamping into molds with a size of 40×40×160 mm. After 24 hours, the samples were unmolded and dried in an oven at a gradually increasing temperature up to 110 °C. After cooling, the samples were cut into 4 cm cubes and their compressive strength was determined. Cylindrical samples were prepared from the mixtures in a similar way for analysis of refractoriness under load according to the EN ISO 1893 standard. The samples were then pre-fired at a temperature of 1350 °C.

The second research direction involved testing the potential use of FSD for the production of metakaolin. Dried granules from mixture R, prepared according to the above procedure, were fired at a rate of 5 °C/min at temperatures of 600-850 °C with a duration of 3 hours. After cooling, the granulate was ground in a planetary mill at 400 rpm for 30 min. The resulting powder was used to determine the pozzolanic activity using the Chapelle test. The principle of the method is heating and homogenizing a mixture consisting of 0.33-0.34 g of the sample, 0.43-0.44 g of CaO and 80 ml of distilled water at 93 °C for 17 hours. After cooling and filtering, the content of dissolved calcium in the filtrate is determined by titration with 0.1M HCl. The result of the measurement is a number indicating the amount of $Ca(OH)_2$ bound by one gram of pozzolan, i.e. the analyzed sample. The sample fired at 650 °C with the highest pozzolanic activity ($FSD_{650°C}$) was further used to verify the possibility of its application for the production of geopolymers. They consisted of the following components. Potassium water glass (PWG) with a modulus of 1.7 and sodium water glass (SWG) with a modulus of 2.0 were used as activators, slag and alumina cement Górkal 40 as a hardener, a commercial silicone-based sample as a plasticizer and chamotte aggregate A111 with a grain size of 0-1 mm as a filler. A complete overview of the composition of the tested geopolymer mixtures is given in Table 4. The formulations of the mixtures were based on patents US20160152521 and US2010010139A, which relate to the use of the pozzolanic activity of fly ash. The water content of the MPSl and MefPSl samples was adjusted to achieve a vibroplastic consistency.

The mixtures were homogenized using a planetary mixer and then manually or vibro-tamped into molds with dimensions of 40×40×160 mm. The setting was carried out according to the following procedure. The samples were covered with plastic wrap to prevent significant drying and left for 24 hours in the molds at room temperature. Subsequently, they were unmolded and placed on wire racks for another 24 hours and finally hardened in an oven at 60 °C. The resulting rods were used to determine the flexural strength, compressive strength and density criteria. For the selected mixtures, the refractoriness under load was also determined. To compare the quality of metakaolin prepared from FSD, a geopolymer sample was also prepared from commercial metakaolin Mefisto L05, and its properties were subsequently analyzed.

Table 4. Composition of geopolymer samples. (FSD650°C – fly shale dust fired at 650 °C, PWG – potassium water glass, SWS – sodium water glass, cement. The water content is expressed relative to 100% of the remaining mixture.)

Sample	Metakaolin (%)		Activator (%)		Hardener (%)		Water (%)	Filler (%)	
MPSl	$FSD_{650°C}$	64.9	PWG 1.7	18.9	Slag	16,2	14,0	-	-
MefPSl	$Mefisto_{L05}$	64.9	PWG 1.7	18.9	Slag	16,2	20,3	-	-
MPSlCh	$FSD_{650°C}$	16.9	PWG 1.7	13.5	Slag	3.0	-	Chamotte	66.7
MSSlCh	$FSD_{650°C}$	16.9	SWG 2.0	13.5	Slag	3.0	-	Chamotte	66.7
MSCCh	$FSD_{650°C}$	16.9	SWG 2.0	13.5	Cement	3.0	-	Chamotte	66.7

3. Results and Discussion

3.1. Aggregates

In order to granulate the mixture of FSD with water or with other raw materials, a relatively narrow range of water content had to be used. If the water content was too low, the mixture was insufficiently plastic and it was not possible to push it through the output adapter of the extruder (Salehi and Salem 2008). With an excess of water, long fibers were formed, which stuck together to form a compact mass. Under optimal conditions, elongated cylindrical granules were formed, which contained numerous cracks due to the excess solid phase and relatively high output pressure. During handling of dried granules (for example, during manual sieving) they broke at the place of cracks into smaller cylindrical and spherical particles (Fig. 2). The content of fine particles below 1.25 mm was 22%.

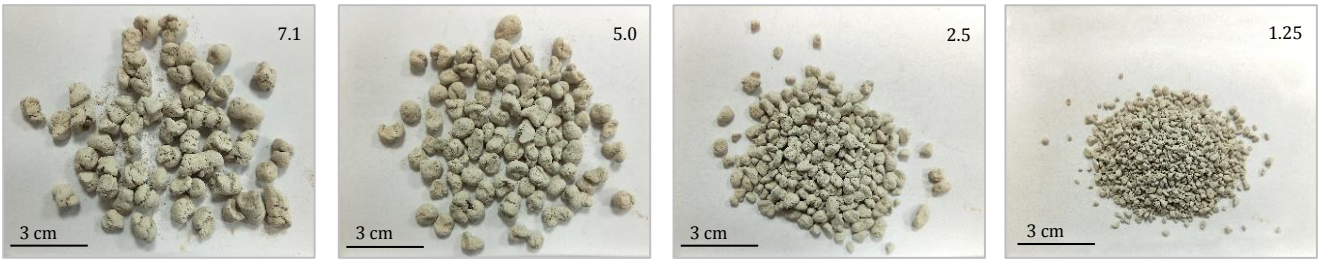

Fig. 2. Granulate fraction on sieve 7.1, 5.0, 2.5, and 1.25 mm.

The granules were relatively strong. It was difficult to squeeze them between the fingers. They exhibited low abrasion resistance, as also evidenced by the relatively high proportion of fine particles. The compressive strength after drying of the manually tamped samples was around 1 MPa for all three tested mixtures R, RK and RA. Their bulk density reached 1550-1600 kg/m^3, in the case of the mixture with alumina almost 1800 kg/m^3. Loss on ignition of granules after firing at a temperature of 1150 °C reached 6.2% (R), 7.0% (RK) and 3.9% (RA). The mixture with alumina showed a lower loss due to its lower clay content, and consequently a lower proportion of chemically bound water. The progression of granule sintering is shown in the graphs in Fig. 3. Samples R and RK exhibited a relatively similar behavior. Their more pronounced sintering occurred in the temperature range of approximately 1150-1450 °C. After firing at 1450 °C, they showed a bulk density of approximately 2180 kg/m^3, an absorbency of 4.1% and an apparent porosity of 9.0%. In the case of the mixture RA, more pronounced sintering occurred at 200-250 °C higher compared to the other two samples. After firing at 1650 °C, it had a bulk density of 2290 kg/m^3, an absorbency of 6.8% and an apparent porosity of 15.6%.

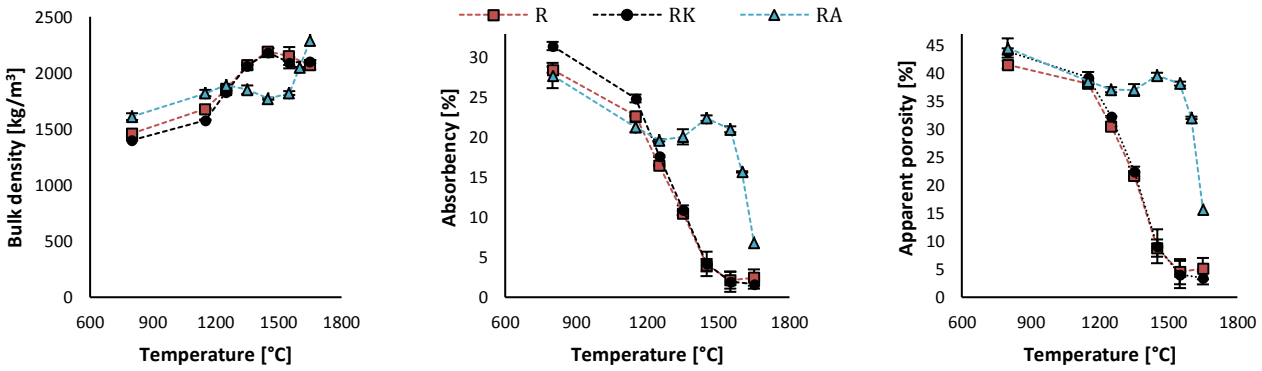

Fig. 3. Dependence of bulk density, absorbency and apparent porosity of granulate on firing temperature. (number of measurements: n = 3)

The results of the thermal and mineralogical analysis of the FSD and the granules R and RA made from it are shown in the graphs in Figs. 4 and 5. In the temperature range up to approximately 200 °C, free water was removed corresponding to a 0.58% weight loss. The majority weight loss of 5.4% was registered in the temperature interval of about 450-650 °C, with a maximum at 540 °C associated with the dehydroxylation of kaolinite. Dehydroxylation of muscovite occurred in the temperature range of approximately 700-900 °C, with a maximum at about 850 °C (Jia, et al. 2015). The interpretation of the exothermic band at a temperature of 978 °C is not unequivocal. It included theories such as the formation of γ-Al_2O_3, Al-Si spinel, mullite or SiO_2. In more detail, the whole subject is discussed in the book Phase Transformation of Kaolinite Clay (Chakraborty 2014). At temperatures above 1050 °C, the formation of high-temperature phases mainly mullite and cristobalite occurred, while the quartz content decreased. Above 1350 °C, the cristobalite content decreased, while the mullite fraction further increased. The total loss of ignition after firing at 1400 °C was 6.70%. The addition of alumina led to a higher mullitization of the aggregates after firing above 1350 °C. A side effect of the reaction was a reduction, to nearly zero, of the cristobalite fraction compared to FSD alone. Mullite, formed by needle-shaped crystals, is characterized by high refractoriness above 1700 °C and a low coefficient of thermal expansion 4.5–5.6 × 10^{-6} K^{-1} (Samadi et al. 2022), thereby contributing to enhanced mechanical strength, refractoriness – as confirmed by the graph in Fig. 7, and resistance to sudden temperature changes. Given its relatively low content, cristobalite is not expected to significantly affect the properties of fired FSD. At higher contents, however, microcracks and a reduction in strength may occur due to the α ↔ β phase transformation at approximately 220 °C, which is accompanied by a ~5% volume change (Stokes 2024).

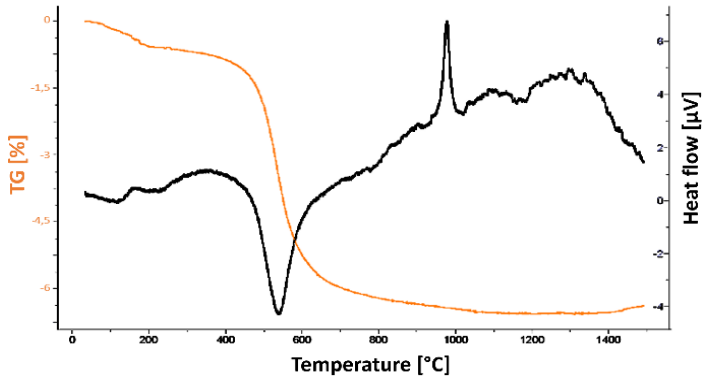

Fig. 4. TG-DTA analysis of the FSD. (weight 65.11 mg, rate 5 °C/min, atmosphere air)

Electron microscope photographs of the FSD and ground granules R fired at temperatures of 650, 1350 and 1650 °C are shown in Fig. 6. Spherical ash particles were visible in the FSD. Partial sintering was observed on the surfaces of granules fired at 1350 °C. After firing at 1650 °C, complete sintering occurred. In the corresponding photo, larger sharp-edged particles of the aggregates were visible, accompanied by finer particles formed during the grinding of the granulate.

The results of the refractoriness under load analysis of the samples R, RK and RA are shown in the graphs in Fig. 7 (graphs a and b). In the case of the unfired sample R, deflection occurred at a significantly lower temperature compared to the sample fired at 1350 °C. The deflection was not caused by lower refractory properties, but by shrinkage resulting from sintering and phase transformations. The refractory properties of samples R and RK were partly similar. Their more significant deformation during the heat resistance test occurred at temperatures above 1350 °C, likely due to shrinkage, among other factors. The addition of alumina increased the deformation temperature (Andrews et al. 2013), in the case of the RA sample by about 100 °C.

3.2. Metakaolin

A commercial sample of metakaolin, designated Mefisto L05, had a pozzolanic activity of 932 mg/g. The FSD exhibited a low pozzolanic activity of 172 mg/g. Firing in the temperature range of 600-850 °C increased its pozzolanic activity (Fig. 8) with a maximum value of 476 mg/g observed after firing at 650 °C. This was in accordance with the results of the thermal analysis, which indicated that the dehydroxylation of kaolinite occurs in the temperature range of 500–650 °C. Commercial metakaolin contained very fine particles with d_{50} = 3 µm and d_{90} = 10 µm, while metakaolin prepared from FSD contained coarser particles. This was attributed to the lower efficiency of the planetary mill used to grind the fired granulate. No significant increase in pozzolanic activity was observed when the grinding time was extended beyond 30 minutes. The same trend was observed for the fraction below 32 µm. By grinding metakaolin to a finer particle size, or to a size comparable to the commercial sample, an increase in its pozzolanic activity could be expected. However, FSD cannot achieve the pozzolanic activity of the commercial sample because it has already been partially exposed to high temperatures during industrial processing, resulting in the conversion of part of the original kaolin into high-temperature phases, primarily mullite, as evidenced by the diffractogram in Fig. 5.

The fired sample of metakaolin, like the original FSD, partially contained high-temperature phases. As a result, it showed a lower absorbency compared to the commercial sample. Its oil number was 36 g/100 g, while the Mefisto L05 exhibited 51 g/100 g. The difference in absorbency had to be considered when preparing geopolymer samples with regard to the desired consistency of the mixture.

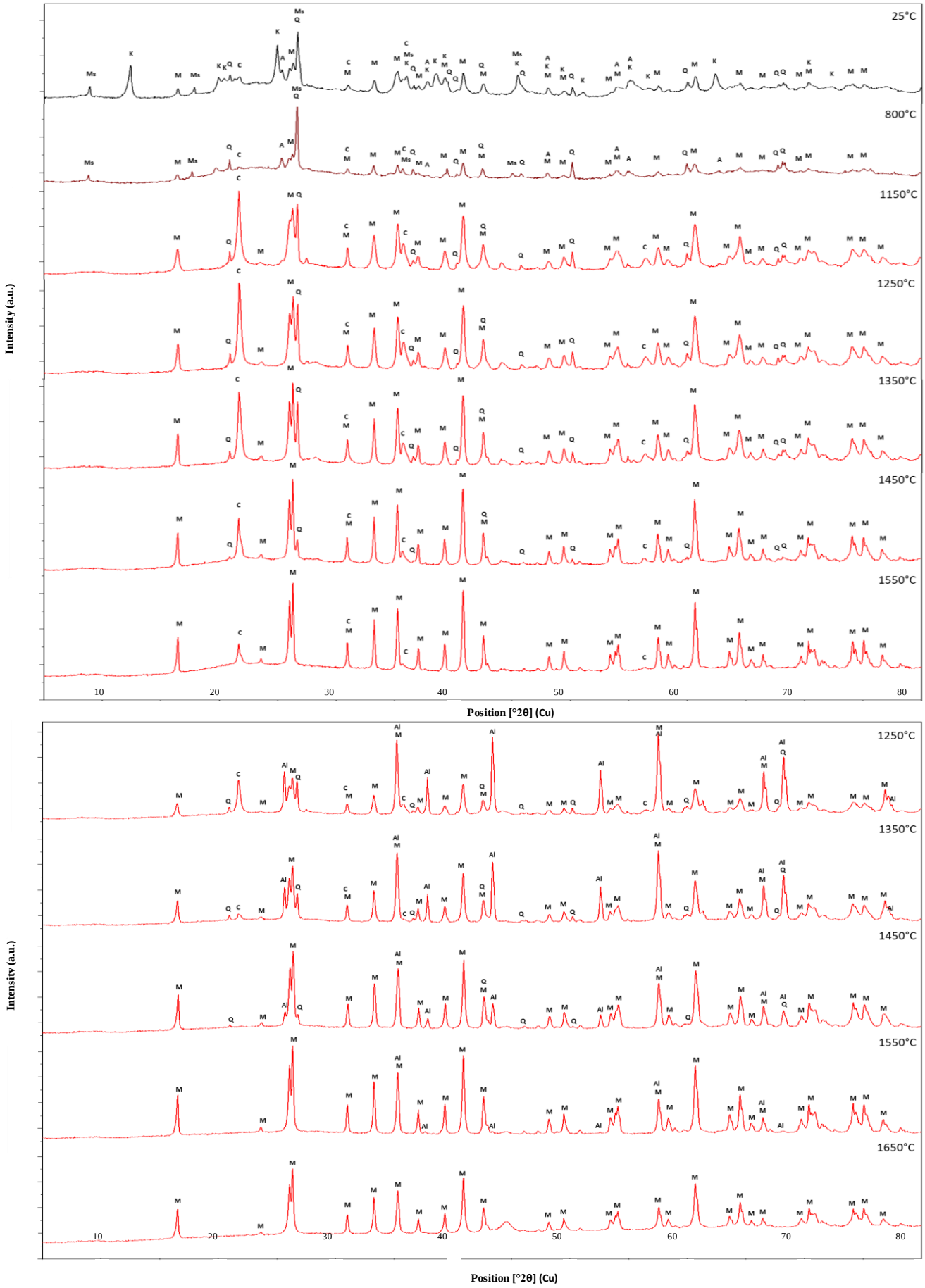

Fig. 5. Diffractogram of granulate R (top) and RA (bottom) depending on firing temperature. (M – mullite, Q – quartz, C – cristobalite, K – kaolinite, Ms – muscovite, A – anatase, Al – corundum)

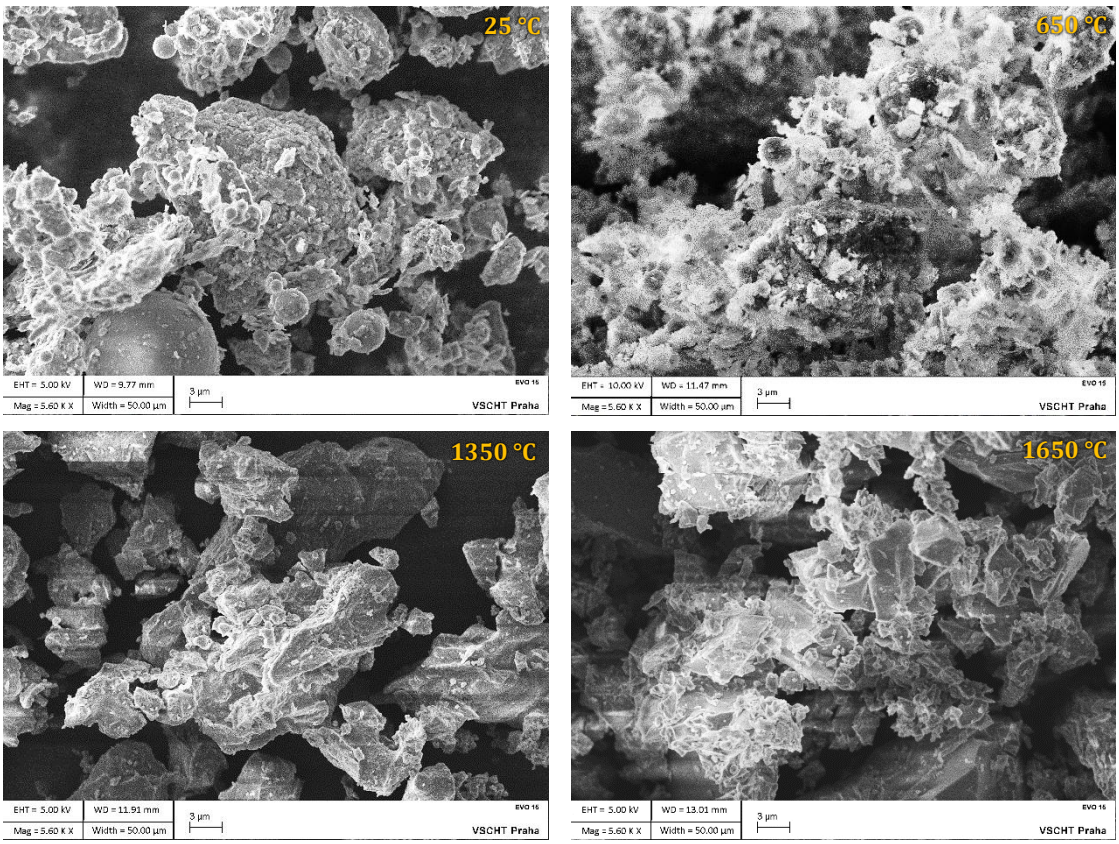

Fig. 6. Photos of original FSD and fired at temperatures of 650, 1350 and 1650 °C.

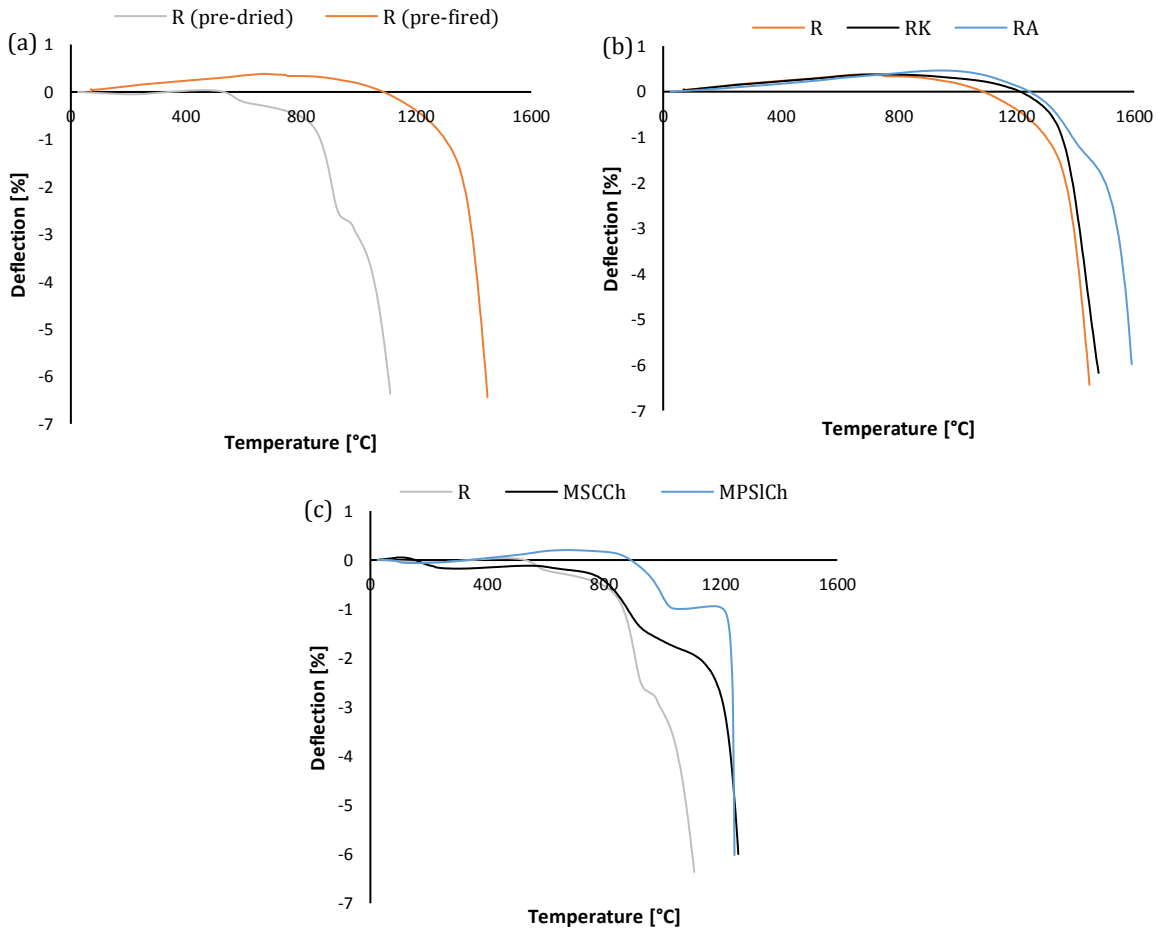

Fig. 7. Refractoriness under load: (a) Sample R pre-dried at 110 °C and the pre-fired at 1350 °C; (b) Samples R, RK and RA pre-fired at 1350 °C; (c) MSCCh and MPSlCh geopolymer samples R pre-dried at 60 °C and for comparison sample R pre-dried at 110 °C.

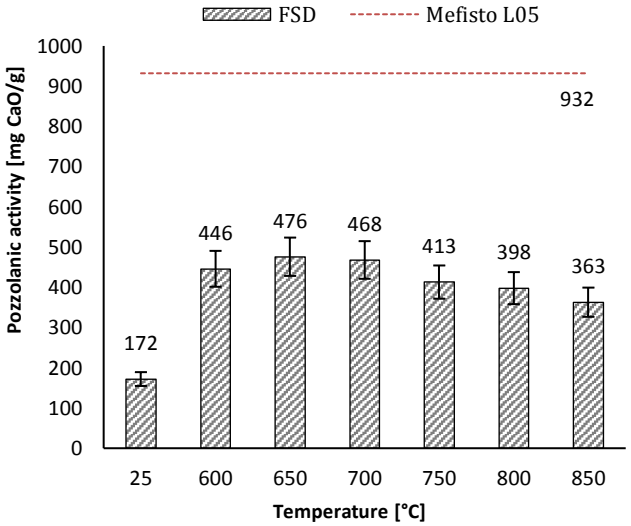

Fig. 8. Dependence of pozzolanic activity of FSD on firing temperature. (According to AFNOR (2012), the results are expected to fall within a ±10% variation.)

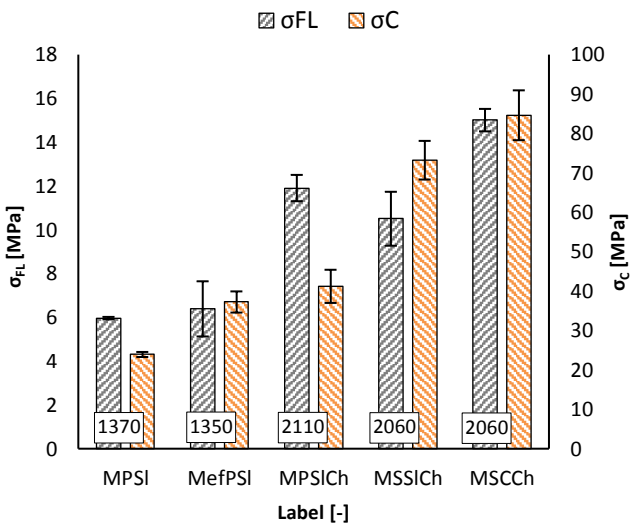

Fig. 9. Flexural and compressive strength and bulk density (at the base) of geopolymer samples (n = 3; 4).

Test samples of geopolymers MPSl and MefPSl exhibited vibroplastic consistency. Samples with the addition of chamotte aggregate MPSlCh, MSSlCh and MSCCh showed a ramming consistency. Geopolymers were prone to cracking due to shrinkage during setting and hardening (Khan et al. 2019). Cracks usually did not occur in samples containing filler due to an excess of aggregates. The mechanical properties of the samples are shown in Fig. 9. Geopolymers from prepared and commercial metakaolin MPSl and MefPSl showed similar flexural strength of approx. 6-6.5 MPa, but a different compressive strength of 24 MPa compared to 37 MPa. The difference can be attributed to the higher content of the binding phase in the commercial metakaolin sample, whereas the MPSl sample contains partly high-temperature phases such as mullite. The higher pozzolanic activity of the commercial metakaolin resulted in increased reactivity, as reflected by the shorter setting time of 195 minutes compared to 255 minutes for the second sample. The addition of chamotte aggregate improved the mechanical properties by reducing shrinkage and cracking. Sodium water glass activated geopolymers exhibited higher strength than potassium activator, in accordance with the literature. The reasons for this are as follows: NaOH has a greater ability to liberate silicate and aluminate monomers during the initial stage of the geopolymerization process, when the aluminosilicate (metakaolin) particles are dissolved (Duxson et al. 2007, Li et al. 2025; Provis and Deventer 2009). The second reason is the smaller ionic radius of Na^+, which promotes the formation of a denser and more highly cross-linked aluminosilicate gel (Hounsi, et al. 2019). The best mechanical properties were achieved when sodium glass was used as an activator and alumina cement as a hardener, when the flexural strength was 15 MPa and the compressive strength was 85 MPa.

The results of refractoriness under load of selected geopolymer samples are shown in Fig. 7 (graph c). For comparison, the progression of the sample R was also included. The samples were not pre-fired. In the temperature range of approximately 100-200 °C, minor deformation occurred, probably caused by drying and hardening. As the temperature increased, a slight expansion of the samples was observed due to thermal expansion. In the temperature range of 850-1000 °C and 1150-1250 °C, more significant deformations of the samples occurred due to the effect of melting oxides CaO, K_2O and Na_2O and due to phase transformations. The sample with sodium-based activator was deformed at lower temperatures, in accordance with the literature (Zarębska et al. 2022). In contrast, the original MSCCh sample contained only 1.9 wt.% Na_2O, whereas the MPSlCh sample contained 3.8 wt.% K_2O, due to the differences in silicate modulus and solids content of the sodium and potassium water glasses (SWG and PWG). This highlights the strong fluxing effect of Na_2O. The CaO content in the MSCCh and MPSlCh samples is relatively low, at approximately 1 wt.%, and is therefore not expected to significantly reduce the refractory properties. Its primary source is the cement hardeners or slag, which are incorporated in a very small proportion of around 3 wt.%.

The main product of the geopolymer reaction is an alkaline aluminosilicate gel with a low degree of structural order, whose development is influenced, among other factors, by the K/Si, Na/Si, and Al/Si ratios. Short setting times and higher K/Si (or Na/Si) ratios lead to a less crystalline product (Shi et al. 2025). This effect is also attributed to the addition of slag or cement hardeners, which supply calcium that reacts with the dissolved silicate precipitates in the activator and accelerates the formation of the C-A-S-H gel and thus the geopolymerization (Kabirova et al. 2022). As a result of the relatively short setting times, the prepared geopolymers remain predominantly amorphous except for the high-temperature mullite and cristobalite phases present in the original FSD. The geopolymer structure, including

porosity, is influenced by the amount of mixing water, which was adjusted to achieve a similar consistency across geopolymer binders and mixtures, a key factor for material processing. In the case of metakaolin, water absorption is indirectly related to its reactivity, which supports the observation that a higher oil absorption value of the commercial metakaolin corresponds to higher strength of the geopolymer binder MefPSl compared to MPSl. The mixing water content also depends on the type of alkaline activator used. Potassium water glass exhibits higher stability in aqueous solutions due to the lower hydration energy of K+ compared to Na+, which allows for a higher solids concentration. Consequently, the potassium water glass used contained 54 wt.% dry matter, whereas the sodium water glass contained only 42 wt.% dry matter. The formation of N–A–S–H gel results in a greater proportion of bound water relative to P–A–S–H gel. The higher water-binding capacity may accelerate the transformation of free water into gel-bound water, leading to a reduction in the fluidity of fresh geopolymer pastes (Zhang et al. 2020).

The following table presents a comparison of the mechanical properties of the prepared geopolymer samples with examples reported in the literature. The obtained strengths are relatively high, particularly for the sample activated with sodium water glass. Aggregate, as well as other potential additives, appears to have a significant influence. For instance, several studies report that the addition of fibers leads to a significant increase in flexural strength.

Table 5. Comparison of results with literature data (Bezerra and Luz 2024; Albidah, et al. 2021; Mohmmad et al. 2023; Skyrianou et al. 2025; Kuenzel et al. 2014; Xu et al. 2025; Borçato et al. 2023; Latella et al. 2008; Li et al. 2022; Chairunnisa et al. 2024; Tippayasam et al. 2014; Zhang et al. 2023; Yang et al. 2022).

Title	Activator	σ_C (MPa)	σ_{FL} (MPa)
MSCCh	Na-based	84.6	15.0
Literature	Na-based	35.3–100.0	5.2–30.0
MPSlCh	K-based	41.2	11.9
Literature	K-based	30.3–80.0	6.7–13.1

4. Conclusions

Fly shale dust FSD mixed with water could be pelletized by extrusion through an adapter with circular meshes with a diameter of 9 mm. The key to creating cylindrical granules was to maintain a relatively narrow water content, when the mixture had the consistency of a ductile mass with lower plasticity. If the water content was low, the extruder could not push the mixture through the output adapter. Otherwise, the extruded mixture stuck together. The dried granulate contained particles in the range of approximately 0-10 mm, while the proportion of fine particles below 1.25 mm was 22%. Industrial-scale extrusion or pellet pressing could likely produce denser granules with lower porosity. The compressive strength of the dried mixture reached around 1 MPa. By firing granulate, it was possible to produce a refractory aggregate with a bulk density of 2180 kg/m^3, an absorbency of 4.1% and an apparent porosity of 9.0%. With the addition of alumina (RA sample), sintering occurred at a temperature 200-250 °C higher. At the same time, it exhibited a higher degree of mullitization during firing. This confirmed that the refractory properties of aggregates corresponded to their sintering activity (Liu et al. 2022). The material prepared in this study was comparable to lower quality commercial chamotte, but it still exhibits very good properties. Although it contained a slightly higher proportion of TiO_2, the material maintained a high refractoriness above 1670 °C, due to its high Al_2O_3 content and low alkali oxide content.

By firing the FSD granulate at a temperature of 650 °C, it was possible to increase the pozzolanic activity of the powder from the original 172 mg/g to 476 mg/g. For comparison, the commercial sample of metakaolin had a higher pozzolanic activity of 932 mg/g. The prepared pozzolanic material has been successfully tested for the production of geopolymers, achieving a flexural strength of 15 MPa and a compressive strength of 85 MPa. Therefore, it can be considered suitable as an active additive in construction materials. The addition of metakaolin to cement typically ranges between 5 and 15%, while in special applications it may reach up to 25%. Fillers are commonly added at levels of up to 5%. The metakaolin prepared in this study contains a partial filler component, primarily the high-temperature phase mullite. Therefore, its addition into concrete mixtures is optimum, as both its pozzolanic activity and filler effect can be utilized. In the case of cement itself, a lower addition should be considered, with expected levels of approximately 5–8%, which also contributes to a reduction in CO_2 emissions associated with cement production.

Although the products from both studied processes exhibit lower quality than commercially available variants, they still represent materials with high potential applications. Refractory aggregate could be used for the production of fireclay bricks or castables. Metakaolin could be added to concrete mixtures, serving both as a reactive component with cement and as a filler. Their technological production process involves standard operations such as granulation, drying, firing, and grinding. However, the critical factor in industrial scale will be the techno-economic analysis, which should consider reduced energy costs for input processing (crushing and grinding), increased costs for treatment (granulation), lower revenues due to slightly inferior product quality, and simultaneously lower landfill costs.

Acknowledgements

This research has previously been presented at SUROVINY 2023 held in Prague, Czechia, on May 17-18, 2023. Extended version of the research has been submitted to Challenge Journal of Concrete Research Letters and has been peer-reviewed prior to the publication.

Funding

The authors received no financial support for the research, authorship, and/or publication of this manuscript.

Conflict of Interest

The authors declare(s) no potential conflicts of interest with respect to the research, authorship, and/or publication of this manuscript.

Data Availability

The datasets generated and/or analyzed during the current study are not publicly available but are available from the corresponding author upon reasonable request.

AI Assistance

No AI-based tools were used in the preparation of this manuscript.

Author Contributions

All authors made substantial contributions to the conception and design of the study, acquisition of data, analysis and interpretation of data; drafted or critically revised the manuscript for important intellectual content; and approved the final version to be published.

REFERENCES

Abdelgader H, Amran M, Kurpińska M, Mosaberpanah M, Murali G, Fediuk R (2022). 10 - Cement kiln dust. *In*: *Ramezanianpour AA. Sustainable Concrete Made with Ashes and Dust from Different Sources.* Woodhead Publishing, Cambridge, United Kingdom, 451-479.

Aird P (2019). Deepwater Drilling. Gulf Professional Publishing, Oxford, United Kingdom.

Albidah A, Alghannam M, Abbas H (2021). Characteristics of metakaolin-based geopolymer concrete for different mix design parameters. *Journal of Material Research and Technology,* 10, 84-98.

Andrews A., Adam J, Gawu SK (2013). Development of fireclay aluminosilicate refractory from lithomargic clay deposits. *Ceramics International,* 39(1), 779-783.

Aziz I, Abdullah M, Yong H, Ming L, Hussin K, Azimi E (2015). A review on mechanical properties of geopolymer composites for high temperature application. *Key Engineering Materials,* 660, 34-38.

Bezerra B, Luz A (2024). High-alumina refractory castables bonded with metakaolin-based geopolymers prepared with different alkaline liquid reagents. *Ceramics International,* 50(11), 18628–18637.

Boateng A (2008). Rotary Kilns. Butterworth-Heinemann, Oxford, United Kingdom.

Bojanovský J, Máša V, Hudák I, Skryja P, Hopjan J (2022). Rotary kiln, a unit on the border of the process and energy industry—Current state and perspectives. *Sustainability,* 14(21), 13903.

Borçato AG, Thiesen M, Medeiros RA (2023). Mechanical properties of metakaolin-based geopolymers modified with different contents of quarry dust waste. *Construction and Building Materials,* 400, 132854.

Bucher R, Cyr M, Escadeillas G (2021). Performance-based evaluation of flash-metakaolin as cement replacement in marine structures – Case of chloride migration and corrosion. *Construction and Building Materials,* 267, 120926.

Chairunnisa N, Haryanti N, Nurwidayati R, Pratiwi A, Arnandha Y, Manik T, Suryajaya, Saputra Y, Hazizah N (2024). Characteristics of metakaolin-based geopolymers using bemban fiber additives. *Materials Science,* 11(4), 815-832.

Chakraborty A (2014). Phase Transformation of Kaolinite Clay. Springer India, New Delhi, India.

Cong P, Cheng Y (2021). Advances in geopolymer materials: A comprehensive review. *Journal of Traffic and Transportation Engineering,* 8(3), 283-314.

Debnath N, Boga S, Singh A, Majhi M, Singh V (2022). Fabrication of low to high duty fireclay refractory bricks from lignite fly ash. *Ceramics International,* 48(9), 12152-12160.

Djangang C, Elimbi A, Melo UC, Lecomte GL, Nkoumbou C, Soro J, Bonnet JP, Blanchart P, Njopwouoy D (2008). Sintering of clay-chamotte ceramic composites for refractory bricks. *Ceramics International,* 34(5), 1207-1213.

Duxson P, Fernández-Jiménez A, Provis JL, Lukey GC, Palomo A, Deventer JS (2007). Geopolymer technology: the current state of the art. *Journal of Materials Science,* 42, 2917–2933.

EN 993-1 (2018). Methods of test for dense shaped refractory products – Part 1: Determination of bulk density, apparent porosity and true porosity. European Committee for Standardization, Brussels, Belgium.

Hounsi AD, Lecomte-Nana G, Djétéli G, Blanchart P, Alowanou D, Kpelou P, Napo K, Tchangbédji G, Praisler M (2019). How does Na, K alkali metal concentration change the early age structural characteristic of kaolin-based geopolymers. *Ceramics International,* 40(7), 8953-8962.

Jala S, Sharma P (2019). Effect of cement kiln dust and RBI grade 81 on engineering properties of plastic clay. *Proceedings of the International Conference on Environmental Geotechnology, Recycled Waste Materials and Sustainable Engineering.* Singapore, 37-49.

Jia F, Su J, Song S (2015). Can natural muscovite be expanded? *Colloids and Surfaces A: Physicochemical and Engineering Aspects,* 471, 19-25.

Kabirova A, Uysal M, Hüsem M, Aygörmez Y, Dehghanpour H, Pul S, Canpolat O (2022). Physical and mechanical properties of metakaolin-based geopolymer mortars containing various waste powders. *European Journal of Environmental and Civil Engineering,* 27(2), 437-456.

Kaminskas R, Savickaite B (2023). Expanded clay production waste as supplementary cementitious material. *Sustainability,* 15(15), 11850.

Khan I, Xu T, Castel A, Gilbert RI, Babaee M (2019). Risk of early age cracking in geopolymer concrete due to restrained shrinkage. *Construction and Building Materials,* 229, 116840.

Kuenzel C, Li L, Vandeperre L, Boccaccini AR, Cheeseman CR (2014). Influence of sand on the mechanical properties of metakaolin geopolymers. *Construction and Building Materials,* 66, 442-446.

Lam M, Nguyen D, Nguyen D (2021). Potential use of clay brick waste powder and ceramic waste aggregate. *Construction and Building Materials,* 313, 125516.

Latella BA, Perera D, Durce D, Mehrtens EG, Davis J (2008). Mechanical Properties of Metakaolin-Based Geopolymers with Molar Ratios of Si/Al≈2 and Na/Al≈1. *Journal of Materials Science,* 43, 2693-2699.

Li L, Boumediene N, Follet C, Yang B, Promis G (2025). A review study: The effect of activator type on the compressive basic creep of alkali-activated materials under autogenous condition. *Results in Engineering,* 29, 108831.

Li Q, Chen S, Zhang Y, Hu Y, Wang Q, Zhou Q, Yan Y, Liu Y, Yan D (2022). Effect of curing temperature on high-strength metakaolin-based geopolymer composite (HMGC) with quartz powder and steel fibers. *Materials,* 15(11), 3958.

Liu Y, Xu L, Chen M, Zhang D (2022). Effects of andalusite and kyanite addition on the microstructure, thermo-mechanical properties and corrosion resistance of ultralow-cement bauxite-corundum castables. *Ceramics International,* 48(10), 14141-14150.

Lopes A, Lopes S, Pinto M (2023). Flexural stiffness and structural behavior of alkali-activated metakaolin faced with cement-based beams. *Journal of Building Engineering,* 76, 18.

Malaiškiene J, Antonovič V, Boris R, Stonys R (2022). Improving the physical and mechanical properties and alkali resistance of fireclay-based castables by modifying their structure with SiO2 sol. *Ceramics International,* 48(15), 22534-22544.

Mohmmad S, Shakor P, Muhammad J, Hasan M, Karakouzian M (2023). Sustainable alternatives to cement: Synthesizing metakaolin-based geopolymer concrete using nano-silica. *Construction materials,* 3(3), 276-286.

Muhammed N, Olayiwola T, Elkatatny S (2021). A review on clay chemistry, characterization and shale inhibitors for water-based drilling fluids. *Journal of Petroleum Science and Engineering,* 206, 109043.

NF P18-513 (2012). Addition for concrete - Metakaolin - Specifications and conformity criteria. AFNOR, Paris, France.

Özkılıç YO, Başaran B, Aksoylu C, Karalar M, Martins HM (2023). Mechanical behavior in terms of shear and bending performance of reinforced concrete beam using waste fire clay as replacement of aggregate. *Case Studies in Construction Materials,* 18, e02104.

Padmalosan P, Vanitha S, Kumar VS, Anish M, Tiwari R, Dhapekar NK, Yadav AS (2023). An investigation on the use of waste materials from industrial processes in clay brick production. *Materials Today: Proceedings,* 67, 1-4.

Panesar D (2019). Supplementary cementing materials. *In: Mindess S. Developments in the Formulation and Reinforcement of Concrete (Second Edition).* Woodhead Publishing, Cambridge, United Kingdom, 55-85.

Pillay D, Olalusi O, Kiliswa M, Awoyera P, Kolawole J, Babafemi A (2021). Engineering performance of metakaolin based concrete. *Cleaner Engineering and Technology,* 6, 100383.

Provis JL, Bernal S (2014). Geopolymers and related alkali-activated materials. *Annual Review of Materials Research,* 44, 299-327.

Provis JL, Deventer JS (2009). Geopolymers, Structures, Processing, Properties and Industrial Applications. Woodhead Publishing, Cambridge, United Kingdom.

Rasekh, H., Joshaghani, A., Jahandari, S., Aslani, F., & Ghodrat, M. (2020). Rheology and workability of SCC. *In: Siddique R. Self-Compacting Concrete: Materials, Properties and Applications.* Woodhead Publishing, Cambridge, United Kingdom, 31-63.

Riaz M, Khitab A, Ahmed S (2022). Evaluation of sustainable clay bricks incorporating Brick Kiln Dust. *Journal of Building Engineering,* 24,100725.

Rimstidt JD, Chermak JA, Schreiber ME (2017). Processes that control mineral and element abundances in shales. *Earth-Science Reviews,* 171, 383-399.

Saleh A, Abdel-Gawwad HA, EL-Moghny, MGA, El-Deab MS (2021). The sustainable utilization of weathered cement kiln dust in the cleaner production of alkali activated binder incorporating glass sludge. *Construction and Building Materials,* 300, 124308.

Salehi M, Salem A (2008). Effect of moisture content on extrusion process of kaolinitic–illitic clay in manufacturing of ceramic Raschig ring. *Journal of Materials Processing Technology,* 200(1-3), 232-237.

Samadi A, Gao L, Kong L, Orooji Y, Zhao S (2022). Waste-derived low-cost ceramic membranes for water treatment: Opportunities, challenges and future directions. *Resources, Conservation and Recycling,* 185, 106497.

Sheng JJ (2020). Chapter One - Introduction to shale and tight reservoirs. *In: Alfarge D, Wei M, Bai B, Chen Z. Enhanced Oil Recovery in Shale and Tight Reservoirs.* Gulf Professional Publishing, Cambridge, United Kingdom, 1-6.

Shi C, Liu Y, Qin L, Ghafoor MT, Zhang Z (2025). Time-dependent evolution of the microstructural characteristics of C-A-S-H and N-A-S-H gels with various Ca/Si and Al/Si ratios. *Construction and Building Materials,* 502, 144408.

Skyrianou I, Koutas LN, Papakonstantinou CG (2025). Metakaolin-based geopolymer mortars: Influence of mix design on mechanical properties and durability. *Construction and Building Materials,* 490, 142526.

Stokes JL (2024). β-Cristobalite thermal expansion and stability in environmental barrier coating systems. *Journal of the American Ceramic Society,* 108(2), e20214.

Tippayasam C, Balyore P, Thavorniti P, Kamseu E, Leonelli C, Chindaprasirt P, Chaysuwan D (2014). Potassium alkali concentration and heat treatment affected metakaolin-based geopolymer. *Construction and Building Materials,* 104, 293-297.

Xu W, Briffaut M, Gay N, Shao J (2025). Experimental investigation on the physical and mechanical properties of metakaolin-based geopolymers: Effects of aging and confining pressure. *Applied Clay Science,* 276, 107910.

Yang J, Xu L, Wu H, Jin J, Liu L (2022). Microstructure and mechanical properties of metakaolin-based geopolymer composites containing high volume of spodumene tailings. *Applied Clay Science,* 218, 106412.

Zarębska K, Zabierowski P, Grzywacz MG, Czuma N, Baran P (2022). Fly ash-based geopolymers with refractoriness properties. *Clean Technologies and Environmental Policy,* 24, 2161-2175.

Zhang DW, Zhao KF, Xie F, Li H, Wang D (2020). Effect of water-binding ability of amorphous gel on the rheology of geopolymer fresh pastes with the different NaOH content at the early age. *Construction and Building Materials,* 261, 120529.

Zhang Y, Chen J, Xia J (2023). Compressive strength and chloride resistance of slag/metakaolin-based ultra-high-performance geopolymer concrete. *Materials,* 16(1), 181.

Zheng J, Zhao L, Du W (2022). Hybrid model of a cement rotary kiln using an improved attention-based recurrent neural network. *ISA Transactions,* 129, 631-643.